UNIVERSITY OF COPENHAGEN
FACULTY OF SCIENCE

PhD thesis

Star formation in galaxies across cosmic time

Stellar Populations in Multiwavelength Photometric Observations

Vadim Rusakov

Advisor: Charles L Steinhardt

Submitted: February 14, 2024

This thesis has been submitted to the PhD School of The Faculty of Science, University of Copenhagen

Acknowledgements

I would like to express my deepest gratitude to the individuals who have greatly helped me in my recent pursuits and made the journey a joyful experience. Thank you to my parents Nadia and Vadim and grandparents Eugene and Galina for your unconditional support and love – a lot of this is thanks to you and for you. Thank you to you, Jane, for being my partner in crime, my voice of sanity and for painting every step of the way with colours. To my friends – you are never forgiven and are always warmly welcomed.

To my supervisor, Charles, I am grateful for the many discussions we have had and for keeping my brain in places of productive discomfort. Thank you, Darach, for all vivacious discussions. Johan, tak for din ærlighed og menneskelighed. Thank you to Sune, Thomas and Georgios for your advice and wisdom. I am very grateful to Charlotte for the work done to help younger researchers at the Institute. There are countless times for which I have to thank you for help, Guarn and Helena. To my PhD fellows – Albert, Clara, Irene, Kate, Meghana, David, Iris, Diego, Malte, Natalie and everyone, thank you for being around and helping each other. To Vasily, John, Francesco, Francesca, Peter, Bo, Seiji, Conor, Anne, Marko, Koki and everyone who has joined, thank you for prodding me occasionally in the right directions. Thank you, people at Dawn for your help and for making me feel at home.

I am deeply grateful to Troels for the opportunity to teach alongside him, and for being not just a mentor but also an incredible inspiration. Thank you to Roberto, Sandro, Will, Giovanni and everyone at Cambridge who made my stay memorable and very educational.

It is also worth stating that, just as any other effort, this work is based on a large body of literature and the work of other people in the astrophysics community and beyond. Unfortunately, it is almost impossible to credit all studies and in some places only the most relevant or recent ones are referred to. However, all existing work is respected and appreciated.

Abstract

Until recently, galaxies have been studied back to when the universe was only 5-7% of its current age, yet little is known about the processes that shape their early evolution and reionize most of the neutral gas in the universe by that time. New observations of the James Webb Space Telescope (JWST) and Atacama Large Millimetre Array move this timeline to only 2% and reveal that galaxies appear to be more evolved in the early universe than previously thought. The most distant galaxies appear to produce more light or form sooner than expected from the physics of star formation in local galaxies or than predicted by the cosmological model. By extension, models tuned in the later universe suggest that the early galaxies are also more massive than expected. In addition to that, the nature of the strong ionising radiation in some early galaxies is still unknown and can be tied to distinct types of massive stars or active galactic nuclei. The wealth of new information challenges our understanding of galaxies as complex systems and suggests new alleys for modern research.

This work addresses the problems of excessive stellar light and mass by investigating possible differences in the physics of star formation. The so-called mass-to-light ratio is one of the fundamental properties of galaxies that connects star formation and the total amount of galaxy light. Various case studies of old and young stellar systems in the Milky Way and elliptical galaxies in the late universe, pointed to possible over or under-production of certain types of stars compared to the standard models. The study here implements some of these changes in the galaxy models and tests them using a large sample of images of distant galaxies in multiple wavelengths. The findings show that active galaxies tend to form more massive stars in the past and extrapolating this effect can explain most of the unusual luminous objects observed with the JWST. Therefore, modifications to the fundamental assumptions about star formation may be required. In the future, the new galaxy models need to be tested on the observations of chemical abundances in the earliest galaxies that can be sensitive to distinct types of stars. Finally, this work also presents possible evidence of star formation in one of the most extreme environments in the universe – active galactic nuclei, which, if confirmed, can become one of the testing grounds for extreme star formation conditions in the future.

Resumé

Indtil for nylig er galakser blevet studeret tilbage til, da universet kun var 5-7% af sin nuværende alder, men der er stadig lidt kendt om de processer, der former deres tidlige udvikling og reioniserer det meste af den neutrale gas i universet på det tidspunkt. Nye observationer fra James Webb Space Telescope (JWST) og Atacama Large Millimeter Array flytter denne tidsplan til kun 2% og afslører, at galakser synes at være mere udviklede i det tidlige univers end tidligere antaget. De fjerneste galakser synes at producere mere lys og dannes tidligere end forventet ud fra fysikken af stjernedannelse i lokale galakser og forudsagt af den kosmologiske model. Derudover antyder modeller justeret for det senere univers, at de tidlige galakser også er mere massive end forventet. Derudover er naturen af den stærke ioniserende stråling i nogle tidlige galakser stadig ukendt og kan være knyttet til bestemte typer af massive stjerner eller aktive galaktiske kerner. Mængden af ny information udfordrer vores forståelse af galakser som komplekse systemer og indikerer nye retninger for moderne forskning.

Dette arbejde adresserer problemerne med overdreven stjernelys og masse ved at undersøge mulige forskelle i fysikken af stjernedannelse. Det såkaldte masse-til-lys-forhold er en af de fundamentale egenskaber ved galakser, der forbinder stjernedannelse og den samlede mængde af galakselys. Forskellige casestudier af gamle og unge stjernesystemer i Mælkevejen og elliptiske galakser i det sene univers har peget på mulig over- eller underproduktion af visse typer stjerner sammenlignet med standardmodellerne. Studiet her implementerer nogle af disse ændringer i galaksemodellerne og tester dem ved hjælp af et stort udvalg af billeder af fjerne galakser over flere bølgelængder. Fundene viser, at aktive galakser har tendens til at danne mere massive stjerner i fortiden, og ekstrapolering af denne effekt kan forklare de fleste af de usædvanlige lysstærke objekter observeret med JWST. Derfor kan der være behov for ændringer i de fundamentale antagelser om stjernedannelse. I fremtiden skal de nye galaksemodeller testes på observationer af kemiske rigdomme i de tidligste galakser, som kan være følsomme over for bestemte typer stjerner. Endelig præsenterer dette arbejde også mulige beviser for stjernedannelse i et af de mest ekstreme miljøer i universet – aktive galaktiske kerner, hvilket, hvis bekræftet, kan blive en af prøvegrund for stjernedannelse under ekstreme forhold i fremtiden.

Contents

Chapter 1

Introduction

1.1 History of Galactic Evolution

The current frontier of galaxy studies has reached a new challenge — the earliest galaxies in the universe exhibit features that cannot be fully explained in the current extragalactic framework. In the past, inconsistencies and puzzling findings led to theoretical and observational advancements in extragalactic astrophysics. For example, in 1920, the "great debate" on the extragalactic origin of galaxy-like nebulae (Shapley & Curtis, 1921) eventually led to discovering the expansion of the universe by Edwin Hubble (Hubble, 1926, 1929). Discrepancies in the amount of mass required to reproduce velocity dispersion of galaxies in clusters (Zwicky, 1933; de Swart et al., 2017), their mass ratio to stellar luminosity (Smith, 1936; Holmberg, 1937) or observed rotation curves (Faber & Gallagher, 1979) led to the concept of the missing "dark matter" and inspired alternative gravitational theories (Milgrom, 1983). Observations of an extraordinary variable point source 3C 273 in radio waves that exceeded the luminosity of hundreds of galaxies (Schmidt, 1963) led to the discovery of the first supermassive black hole (SMBH). Finally, recent deepest infrared observations reveal that galaxies are too bright or too numerous at the cosmological epoch associated with their early evolution (Boylan-Kolchin, 2023), which either prompts adjustments to the current galaxy models or challenges the preferred cosmological theory.

One of the ultimate goals of extragalactic astrophysics is to construct a model of galaxy evolution that is capable of predicting reliably a variety of system types and observational signatures across multiple orders of magnitude on the spatial and temporal scales. The previous multi-decade effort uncovered a diversity of galaxy environments, morphological structures, properties of active nuclei, stellar populations and the interstellar medium and dust. Enabled by existing distance rulers and detailed studies of individual galaxies and their populations, it has been possible to make largely successful phenomenological and numerical models of the growth of galaxies to the first billion years. However, recent observations provided rich data of galaxies well into the earliest epoch, which indicate that otherwise minor inconsistencies in the models of galaxies tuned in the local universe may magnify and become significant during the epoch of possibly rapid early growth.

This section provides a brief overview of the studies in the past 30 years that have detailed the various statistical, physical and chemical properties of galaxies at different cosmological epochs and provided interpretations of the time evolution of these properties. First, it presents "Timeline" of galaxy evolution as seen prior to the latest infrared observations of faint galaxies in the context of different timescales. Then, it concentrates on how this timeline has been reconstructed from the measurements of luminosity and model-dependent stellar mass. The section "Key Galaxy Relations" discusses the processes driving galaxy evolution and physical constraints from various observed galaxy relations. Finally, the latest findings made with the James Webb Space Telescope and other observatories and related problems are placed in the context in "Galaxies in the First Billion Years". This chapter closes with an overview of how some of the properties are modelled using the integrated stellar light of galaxies and discusses some of the associated assumptions that are tested in this work.

Timeline

Multiple processes determined galaxy evolution on different timescales and took place during 13.8 Gyr of the universe's lifetime (Planck Collaboration et al., 2020). After the epoch of recombination at $z \approx 1100$ (at ~ 0.4 Myr), the baryons cooled inside overdense regions determined by the primordial plasma fluctuations and dark matter halos that decoupled from the cosmic expansion. On the timescale of $\sim$ 100 Myr the baryon clouds cool and start to fuse in the first stars. The subsequent stellar growth of galaxies proceeds until today through regulation by radiative and hydrodynamic processes at star formation (driven by the feedback of youngest stars on the timescales of $\sim 1 - 100$ Myr), feedback from supermassive black holes (thought to occur on the similar timescale of ~ 100 Myr) and collisions with other galaxies (occur on a ~ 1 Gyr timescale). During this time, galaxies grow into a diverse population, with a variety of morphological structures,

Table 1.1: Timescales of galaxy evolution.

Timescale	Description
~10-100 Myr	Lifetime of massive stars
~10-100 Myr	Lifetime of a super-Eddington (most active) phase of an AGN
~100 Myr	Gas free-fall or cooling timescale
~100 Myr	Crossing time of a Milky Way-like spiral galaxy
~1 Gyr	Time required for merging of two galaxies
~10 Gyr	Age of the universe (i.e., Hubble time)

physical and chemical properties inside the large-scale cosmic environment. Various timescales are shown in Table 1.1 to aid understanding the role of different mechanisms in shaping history of galaxies throughout the rest of this work.

This evolutionary timeline is marked with several notable periods, from dark ages after recombination through the present day. The dark ages ended with the cosmic dawn, when the UV emission of the first stars started to spread and reionize the neutral interstellar and intergalactic medium (ISM, IGM). According to the standard cosmological model (Peebles, 1993; Bullock & Boylan-Kolchin, 2017), the collapse of the first baryon clouds happens from $z = 30$ (Klessen & Glover, 2023). After that, the rate of star formation steadily increased until peaking at the cosmic noon epoch at $z \approx 2$ (Madau & Dickinson, 2014; Behroozi et al., 2013a), by which point galaxies grew most of their stellar mass and enriched the interstellar medium with metals. The rest of the evolution until the current epoch was responsible for developing a morphological Hubble sequence (Hubble, 1926; de Vaucouleurs, 1959; Conselice, 2014) disc-like structure around the central stellar bulges and producing spiral Milky Way-type galaxies with highly-ordered multi-scale stellar and ISM structure, and elliptical galaxies with passive star formation (Faber et al., 2007).

The key to understanding the evolutionary sequence of galaxies is tracking changes in their properties over time. As it is practically impossible to do so for individual galaxies on any relevant timescale, the approach is to take snapshots of galaxies at different epochs and complete the picture by cross-matching their population-level properties. This task would be straightforward if galaxies formed different unique populations that would be tractable over different epochs. However, in reality galaxies represent unimodal or non-linearly separable distributions when viewed in terms of most simple properties. Therefore, it is important to establish the most important galaxy properties to form basic relations in the order of increasing complexity.

Finally, time-stamp studies of the universe rely on determining distances to galaxies which primarily come from estimation of cosmological redshift[1]. This became possible with the help of the multi-wavelength imaging campaigns that can be used to constrain SED models of galaxies. Alternatively, the images can be used to estimate redshift of the Lyman-break galaxies by constraining the position of the Lyman series limit at 912 Å between two adjacent wavelength channels. The redshift of older galaxies can also be estimated using the positions of the Balmer break at 3645 Å. Finally, narrow photometric bands or spectroscopic observations can be used to constrain positions of emission lines to determine redshift with higher precision.

Assembly of Stellar Light

Before it is possible to invoke complicated models of galaxy evolution, it is important to study basic observable properties of galaxies and their population statistics, such as stellar luminosity and its relative distribution referred to as the luminosity function (LF). The characteristic shape of the LF is surprisingly similar at most times: up to the normalisation constant $\phi^\star$, it is best described as a power law at the faint end with the exponent α, and after some characteristic luminosity $L^\star$ the bright end drops off exponentially – the traditional parametrisation of the Schechter function (Schechter, 1976):

$$dn/dL = \phi(L) = \left(\tfrac{\phi^\star}{L^\star}\right)\left(\tfrac{L}{L^\star}\right)^{\alpha} e^{-L/L^\star}. \tag{1.1}$$

Over the past 30 years luminosity function has been studied in multiple deep imaging surveys made from the ground and space. These studies benefited greatly from observing in blank fields with little foreground contamination: Hubble Ultra-Deep Field (HUDF, Beckwith et al., 2006), The Great Observatories Origins Deep Survey (GOODS, Grogin et al., 2011; Koekemoer et al., 2011), the Cosmological Evolution Survey (COSMOS,

---

[1] Other methods exist to measure distances to the most distant galaxies, such as the cosmic gravitational wave sirens (Abbott et al., 2017) or light travel delays due to gravitational lensing (Treu et al., 2022). However, their applicability is limited by the statistical rates of the associated phenomena and therefore are not as widely available as cosmological redshift measurements, which often require constraining at least one or two well-defined spectroscopic features using spectra or images.

Capak et al., 2007; Scoville et al., 2007; Ilbert et al., 2009, 2013; Laigle et al., 2016), Hubble Frontier Fields (HFF, Lotz et al., 2017). Ground-based observations have been fitted into the transmission windows in the optical, radio and a few infrared wavelength ranges, outside of the atmospheric absorption bands.

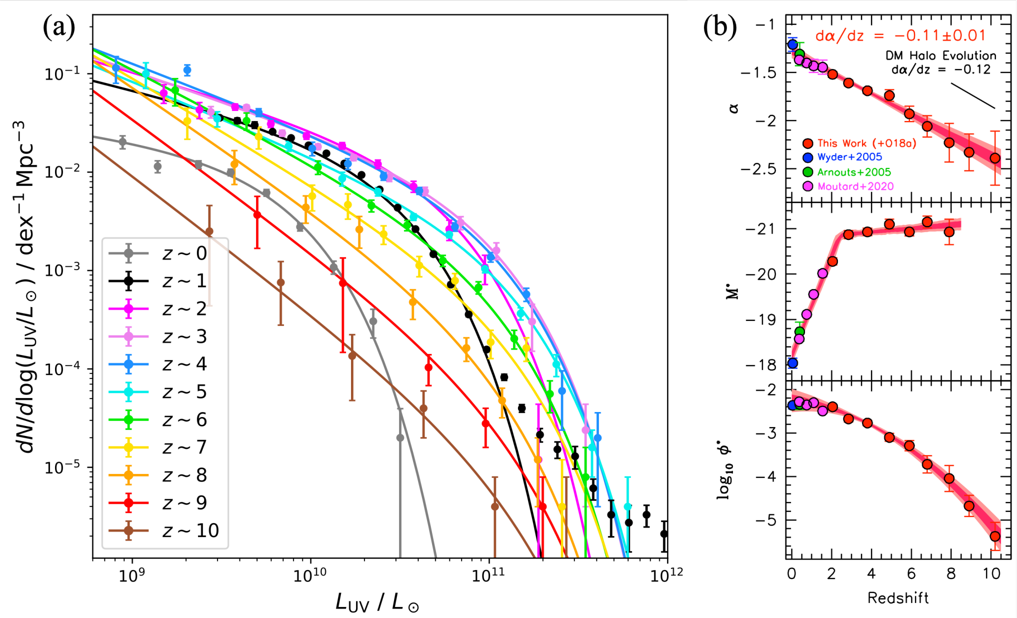

Figure 1.1: Panel (a): UV LF from multiple surveys ($z \sim 0$ from Wyder et al., 2005; $z \sim 1$ from Moutard et al., 2020; $z \sim 2-9$ from Bouwens et al., 2021; $z \sim 10$ from Oesch et al., 2018). These distribution functions trace the evolution in recent star formation, as well as amount of UV dust attenuation. Panel (b): the evolution of the UV LF Schechter function parameters: faint-end slope α, characteristic absolute magnitude $M^\star$ and the normalisation factor $\phi^\star$, for a sample at $2 < z < 9$ (red dots; Bouwens et al., 2021), at $0.3 < z < 1.8$ (magenta dots; Moutard et al., 2020), at $z \sim 0.3$ (green dots; Arnouts et al., 2005) and at $z = 0.055$ (blue dots; Wyder et al., 2005). Figures (a) and (b) and data compilation have been produced in Laursen (2023) and Bouwens et al. (2021), respectively.

Panchromatic observations allowed to study the evolution of LF with redshift. Optical campaigns probed luminosity functions in the UV at redshift $z \sim 1$. Lower-redshift galaxies were observed in wide-field sky campaigns that sampled sufficiently large cosmic volume. On the other end, the observational range expanded to near UV wavelengths (NUV) at $2 < z < 10$ and IR at lower redshifts with the help of the airborne telescopes (Treyer et al., 1998; Sullivan et al., 2000) and space-based Infrared Space Observatory (ISO), Galaxy Evolution Explorer (GALEX) and the Hubble Space Telescope (HST). Finally, the combination of HST and ground-based optical and IR efforts allowed to fill the gaps and photometrically sample most the timeline up to the first billion years (Steidel et al., 1996; Connolly et al., 1997; Giavalisco et al., 2004; Castellano et al., 2010a,b; Hathi et al., 2010; Oesch et al., 2010; Bowler et al., 2012; Tilvi et al., 2013; Oesch et al., 2018; Bouwens et al., 2021).

Luminosity in a given rest-frame waveband is one of the most well-studied and powerful properties. In the rest-frame UV (1300 – 3000 Å) it traces continuum emission of massive (> 10 $M_\odot$) O and B-type stars with the main-sequence timescales of ~ 10 and ~ 100 Myr, and extinction by dust in the star-forming regions. The MIR and FIR luminosity traces the emission of dust in the star-forming regions and cold ISM and has been used to estimate the star formation rate (SFR) in galaxies where dust is heated up by the most recent stellar populations (e.g., Sodroski et al., 1997; da Cunha et al., 2008). Multiple early studies targeted these spectral regions to study recent star formation at $0 \lesssim z \lesssim 10$ (Chary & Elbaz, 2001; Chapman et al., 2005; Elbaz et al., 2007; Pérez-González et al., 2008; Elbaz et al., 2011; Oesch et al., 2018; Bouwens et al., 2021). A compilation of some of these functions in Figure 1.1a shows the evolution of both recent star formation and changes in dust obscuration of galaxies. Their behaviour is consistent with the gradual build-up in typical star formation towards $z \sim 2-3$, as the LF normalisation $\phi^\star$ and logarithmically increases and the faint-end slope α becomes flatter (Figure 1.1b). After $z < 3$, the UV LF turns over and the knee $M^\star$ decreases exponentially towards $z \sim 0$, when the epoch of the formation of massive stars is predominantly completed.

More detail has been added to the global picture of star formation from IR and sub-millimetre observations about stellar mass-dominated star-formation and dust obscuration. It is shown that most of the $z \sim 0-4$ UV observations are attenuated by dust to some extent. ALMA constraints on this contribution from star-formation-heated or ambient dust help to reconstruct the total star formation history (SFH) of the universe, as shown in Figure 1.2. The SFH, traced by the star formation rate density (SFRD), is estimated by integrating the luminosity functions (and converting the luminosity to the SFR, Kennicutt, 1998):

$$\rho_{\mathrm{UV}} = \textstyle\int_0^\infty \phi(L) L dL. \tag{1.2}$$

Most recent results show characteristic agreement between the cosmic SFH (e.g., Madau & Dickinson, 2014; Casey et al., 2018; Zavala et al., 2021).

The LF measurements tell the history of star formation that builds-up

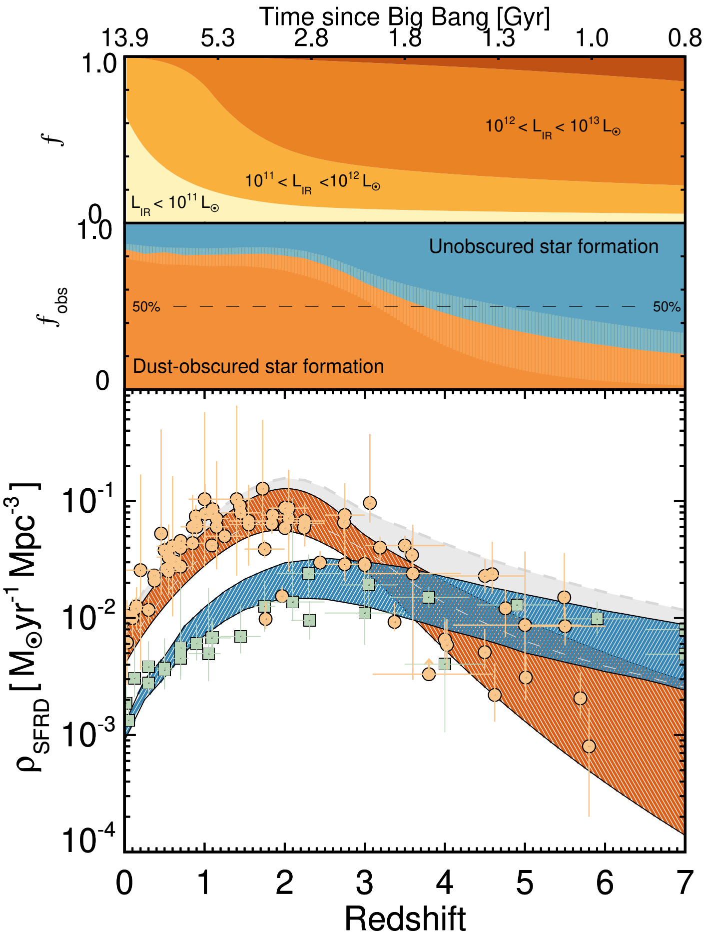

Figure 1.2: Bottom: dust obscured star formation rate density (orange shaded area) computed from double power-law LF based on Mapping Obscuration to Reionization with ALMA (MORA) in Zavala et al. (2021). Unobscured (blue shaded area; from Finkelstein et al., 2015a) and total (grey shaded area) SFRD are also shown. The overplotted data points are from UV surveys, IR or sub-mm surveys (orange circles; see references in Zavala et al., 2021). Middle: fraction of dust-obscured star formation. Top: breakdown of the fraction of galaxies by their infrared luminosity L_{IR} as a function of redshift. Figure is taken from in Zavala et al. (2021).

to and drops exponentially from around the epoch of the cosmic noon at $z \sim 2$, as shown in Figure 1.2. In this context, the UV LF indicate that while the number of blue galaxies actively forming stars does not evolve strongly from the cosmic noon, the red population grows and exhibits elliptical morphology more frequently towards the present day (Faber et al., 2007). Such changes suggest evolutionary connections between the two types, where the end of star formation is associated with ageing stellar populations and where possible mergers drive the morphological changes.

The story holds consistently between the measurements made from young stellar emission in the UV and dust heated by massive stars in the mid-IR to sub-millimetre wavelengths. From IR observations, it is also found that dust obscuration of the star-forming sites in galaxies becomes becomes typical than unobscured after the first 1-2 Gyr.

Assembly of Stellar Mass

To study the physics that governs galaxy growth, it is useful to compare galaxy stellar mass functions (SMF) to their underlying dark matter halos. The SMF, $\phi(M)$, represents the number of galaxies per unit mass and cosmic volume at a given redshift and, like the luminosity function, is best represented by the Schechter function at most times. In the context of the halo mass function (HMF), the SMF is a powerful tool that traces gas and physical processes responsible for galaxy formation, growth and suppression of star formation in galaxy populations and can be used as a cosmological observable (Davidzon et al., 2017; Weaver et al., 2023). Therefore, the SMF can be used to constrain models of the more detailed physical processes on scales varying from individual stars to whole galaxies in semi-analytical (Kauffmann et al., 1994; Hopkins et al., 2008; Peng et al., 2010; Kelson, 2014; Somerville & Davé, 2015; Lagos et al., 2018) models and numerical simulations (Furlong et al., 2015; Pillepich et al., 2018; Davé et al., 2019; Lovell et al., 2021).

The SMF approach has progressed significantly since the first studies started to use near-infrared observations in the local universe (e.g., Cole et al., 2001; Bell et al., 2003; Baldry et al., 2008). The first SMF studies have become possible by using the light of evolved stellar populations in the near-infrared which constitute the bulk of the stellar mass budget of galaxies. First such observations came from the wide-field catalogs of J, H, K_S band fluxes in the surveys 2dF-GRS (Colless et al., 2001), SDSS (York et al., 2000) and GAMA (Driver et al., 2011). Later studies improved the accuracy of measurements by probing wider SEDs in COSMOS (Scoville et al., 2007) surveys, which had large enough sky coverage for dealing with the cosmic variance (Moster et al., 2011; Steinhardt et al., 2021), and included galaxies at redshifts up to $z = 7.5$ in the HST and Spitzer images (Fontana et al., 2006; Ilbert et al., 2010; Pozzetti et al., 2010; Ilbert et al., 2013; Muzzin et al., 2013; Grazian et al., 2015; Song et al., 2016; Davidzon et al., 2017; Stefanon et al., 2021; Adams et al., 2021; McLeod et al., 2021; Weaver et al., 2023). In addition, robust statistical approaches were developed over time (Pozzetti et al., 2010; Davidzon et al., 2017; Leja et al., 2019; Adams

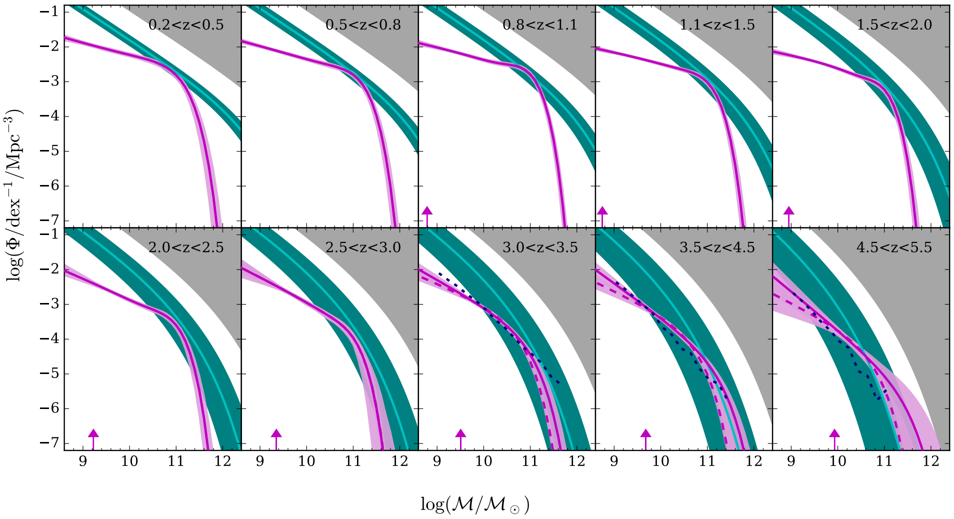

Figure 1.3: Stellar mass functions (magenta lines) overplotted on top of the SMF predicted from halo mass functions (cyan lines) using the stellar-to-halo mass conversion and assuming a typical efficiency of star formation. The gray shaded area denotes the region with excessive baryon fraction density than assumed in the cosmological model. The magenta arrows indicate mass completeness levels. Figure is taken from in Davidzon et al. (2017).

et al., 2021) for dealing with the observational biases including Malmquist (Malmquist, 1922) and Eddington bias (Eddington, 1913) and general mass completeness of a survey, as well as SED fitting.

The result of the extensive previous work has led to a coherent picture of ordered stellar mass assembly. Most notably, the stellar mass growth of galaxies proceeds according to mass downsizing (Cowie et al., 1996; Fontanot et al., 2009) which indicates that the massive end of the SMF forms earlier than the rest. However, more specifically, the studies found that the fastest growth happens for galaxies with the mass close to the SMF Schechter knee $M^\star$ from $z < 3$ (Moster et al., 2013; Behroozi et al., 2013b; Ilbert et al., 2013; Davidzon et al., 2017; Wechsler & Tinker, 2018)[2]. However, the most recent formulations of the SMF appear to be rid of this characteristic mass scale (Weaver et al., 2023) suggesting that it may be an artefact of comparing high-mass ends of active and passive population Schechter functions based on low-number statistics (Steinhardt et al.,

---

[2] Any scale-dependence is counter-intuitive in galaxy growth which is fundamentally driven by the scale-independent gravitational force and therefore points to physical effects responsible for the characteristic mass of quenching galaxies.

2022a). Finally, most of massive galaxies quench by $z = 1$. The small quiescent galaxies grow in numbers rapidly from $z \sim 2$, becoming progressively less massive towards $z = 0$. As it appears, there are multiple pathways to galaxy formation and this may be indicative of the importance of various internal and external processes in producing such ordering.

More insight comes from studying galaxy growth in their respective DM halos (Wechsler & Tinker, 2018), especially where the low and high-mass ends of the SMF diverge from the halo mass function (HMF). Traditionally, these deviations are interpreted as the signature of stellar and AGN feedback, respectively. Figure 1.3 clearly demonstrates these two effects in galaxies observed at $z < 3$. Interestingly, that higher-redshift SMF takes the shape of the smoother power law in this figure and in more recent studies (Stefanon et al., 2021; McLeod et al., 2021; Weaver et al., 2023) and some simulations (Long et al., 2023) at $z > 5-6$, which may indicate diminishing efficiency of AGN feedback for quenching the most massive galaxies in the first ~ 1 Gyr (as found in simulations in Kaviraj et al., 2017; Laigle et al., 2019). Besides, it is also useful to compare SMF with the theoretical SMF predicted by assuming a halo-to-stellar mass conversion. This may point to differences in the physics of star formation, such as efficiency, if more stellar mass is found to form per halo (the last panel of Figure 1.3 has indications of that). Finally, hydordynamical and semianalytical simulations (e.g., Furlong et al., 2015; Pillepich et al., 2018; Davé et al., 2019; Lovell et al., 2021) are tuned to reproduce the local SMF provide overall good agreement with the observed SMF, albeit with some difficulties in predicting the merger rates (Conselice et al., 2022), and significantly miss the low and high-mass ends at the higher redshift (Weaver et al., 2023).

As the estimates of stellar masses of galaxies and their redshift are typically obtained from SED fitting (e.g., Conroy, 2013a), the SMF is prone to the biases in the SED models, such as the IMF, SFH, dust extinction curves and the history of metallicity evolution. It is the goal of the study in Chapter 2 to quantify the bias related to the IMF. In fact, this work shows that if star-forming conditions favour a top-heavy IMF at high redshift, this may provide another explanation of the excessively massive high-end of the SMF at $z > 5$ in Figure 1.3 (Davidzon et al., 2017; Weaver et al., 2023).

Key Galaxy Relations

Until this point in the review, the evidence suggests that galaxies appear to follow evolutionary paths determined broadly by their stellar mass and the DM halos they inhabit and therefore their environment and gas availability.

Once the main episode of star formation takes place in a galaxy of a given stellar mass and redshift, the growth is likely set by the stellar and AGN feedback in most cases.

To study the exact mechanisms driving star formation and its cessation, as well as providing the star-forming gas, it is necessary to make further cross-sections between the most important properties to determine possible relations and their physical or statistical nature. Below is a description of some of the key relations that are relevant for the studies presented afterwards – namely, the star-forming main sequence and some of the fundamental metallicity relations. The first may relation may help to constrain the diversity of mechanisms or conditions driving star formation, while the latter can help to link this to the balance between supplied and removed gas.

Star-forming main sequence

A meaningful picture of galaxy growth emerges from the combined information about star formation from luminosity density and mass growth from stellar mass functions. The star formation rate (SFR) is intuitively correlated with the total stellar mass of galaxies at a given redshift forming a main sequence of star formation (SFMS), where the scatter in this correlation reflects the diversity of underlying processes such as galaxy mergers, stellar and AGN feedback and the availability of gas (Brinchmann et al., 2004; Noeske et al., 2007a; Elbaz et al., 2007; Daddi et al., 2007; Salim et al., 2007; Whitaker et al., 2012, 2014). Various studies probing redshift $0.2 < z < 7.0$ concluded that the SFMS is tightly correlated ($\sim 0.2 - 0.4$ dex one-sigma scatter) and thus most galaxies tend to be in a stable state, except starbursts (above the MS) or low to intermediate-mass quiescent galaxies (below the MS) (Noeske et al., 2007a). Figure 1.4 shows an example of the "concensus" SFMS which different studies are found to reproduce when placed on the common assumption basis (Speagle et al., 2014). The slope of the total SFMS is shallower than 1 in many studies, but is shown to be unity at low redshift when separating the contribution from active and passive regions to the total flux of galaxies (Abramson et al., 2014). In this scenario, the fact that the slope of the main sequence is found to decrease with the age of the universe possibly points to a progressively larger fraction of older stellar populations in the integrated fluxes. These indicators show that star formation is regulated by the same physics in all galaxies and deviations from the sequence suggest changes in gas supply or total efficiency of star formation.

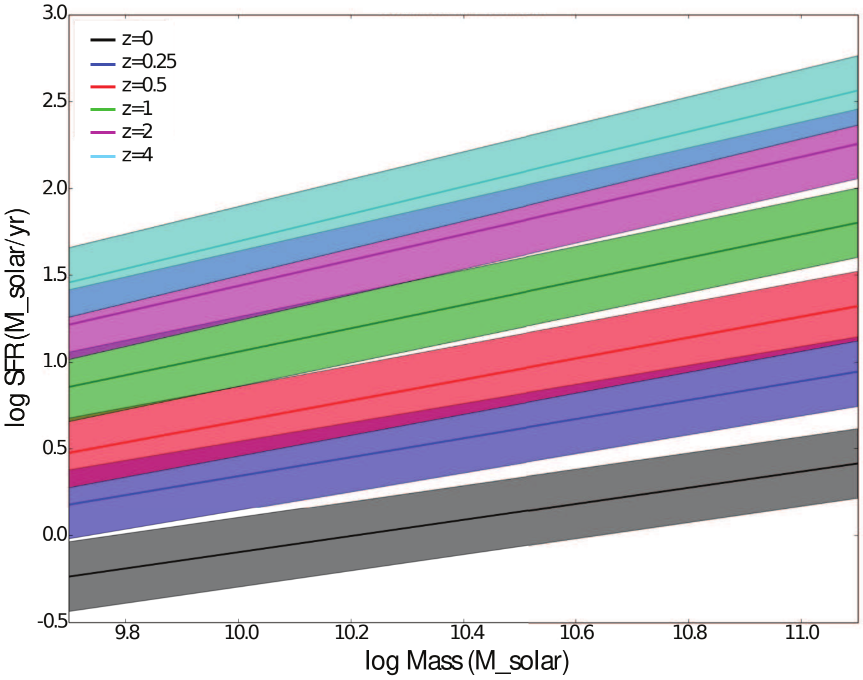

Figure 1.4: Star-forming main sequence from the best-fit models of multiple observational sets at different redshifts considered at the time in Speagle et al. (2014). Figure is taken from in Speagle et al. (2014).

The uniformity of star formation across the main sequence in terms of its dispersion and slope indicates that despite all apparent complexity of stellar and gas-phase properties, morphological structures and sizes, star formation is a unifying process across most of the active population. The deterministic nature of SFMS has been expressed using various models with regulated star formation, where the evolving SFMS is used to infer stellar mass assembly and its cessation (Noeske et al., 2007b; Peng et al., 2010). For example, Noeske et al. (2007b) proposed a "staged" model where the mass of the galaxies entering the main sequence decreases with time for an increasing fraction of a galaxy population (consistent with mass downsizing). The shape of the stellar mass functions motivated the model of Peng et al. (2010) in which star formation quenching is associated with the environmental or mass effects, depending on the mass and redshift of a galaxy. Other, probably less popular approaches showed that the SFMS and its scatter can be described by a diverse set of initial conditions followed by stochastic events in the SFHs of galaxies, instead of a regulated growth (Kelson, 2014;

Abramson et al., 2016). In the end, these relations form a phenomenological basis for tuning models of galaxy evolution using more detailed numerical approaches that may help to further pin point the exact mechanisms of galaxy growth.

Some of the work presented in this thesis attempts to further dissect the SFMS relation in search for more fundamental properties and clues about the star-formation mechanisms – in particular, the IMF is used as the key property that may indicate different modes of growth on the same star-forming main sequence at a given epoch and point to differences in the overall efficiency of star formation in galaxies of different stellar masses.

Mass-metallicity Relation

At a given epoch, the mass-metallicity relation (MZR) traces the history of star formation and gas mixing of galaxies with different stellar mass through the mass and luminosity distribution functions. Overall, the long-term enrichment appears to be gradual and monotonic, although likely sensitive to short-term effects of galaxy mergers, gas inflows in large galaxies or outflows in the smaller ones, as for example typically inferred from the analyses of resolved stellar populations in small galaxies of the local universe (Gallart et al., 1996a, 2019). For galaxy populations in large cosmic volumes, the stellar mass and metallicity exhibit clear correlation, with the less massive galaxies being more pristine. This picture is consistent with the mass downsizing seen from the mass and light distribution functions (Sections 1.1,2.4). It is also clear that passive galaxies of all masses are more enriched than the active (Mannucci et al., 2010) (as seen in Figure 1.5a), which can be explained by "gas starvation" of the passive population and the lack of gas inflows that can dilute metal-rich star-forming galaxies from phenomenological (Peng et al., 2015; Spitoni et al., 2017) or hydrodynamical modelling (De Rossi et al., 2018). Fundamentally, the effect of inflows may be determined by the environment of galaxies (Peng et al., 2015; Trussler et al., 2021): cluster galaxies show little difference in their MZR, while field galaxies have "exclusive" access to the intergalactic gas reservoir and become diluted over time. Similar conclusions were reached in simulations (Engler et al., 2018). Finally, MZR also shows a steady decline from $z = 0$ to $z = 3.5$, as traced the by the gas-phase metallicity (Faisst et al., 2016), and is expected to decline further until the Population II and III stars started the process of chemical enrichment.

Later, it was found that the MZR is a projection of the more fundamental metallicity relation (FMR) that includes the SFR and has the

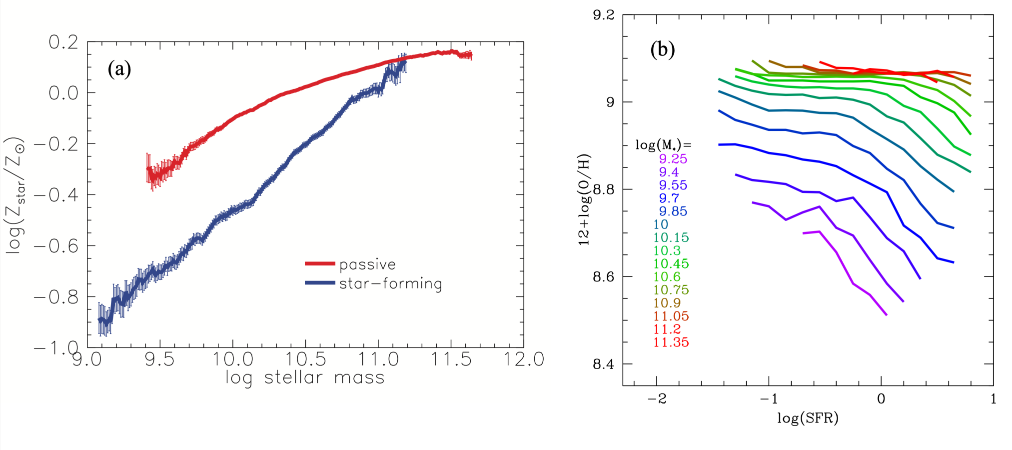

Figure 1.5: Panel (a): mass-metallicity relation. Panel (b): fundamental metallicity relation. Figures (a) and (b) are taken from Peng et al. (2015) and Mannucci et al. (2010), respectively.

relation scatter reduced to the level of measurement errors ($\sim 0.1 - 0.2$ dex) (Mannucci et al., 2010; Andrews & Martini, 2013; Curti et al., 2020). The fundamental nature of the dependence of metallicity on the other two parameters is found using the principal component analysis (Hunt et al., 2012, 2016a). The key result shows that the metallicity decreases with SFR and increases with stellar mass. In this context, it was argued that the downturn of the MZR at high stellar mass is reflected through the similar downturn in the SFMS (Hunt et al., 2016a). Physically, a model by Lilly et al. (2013) parametrised FMR as a function of specific SFR, gas consumption and the balance between outflows and SFR (i.e. mass loading factor). Numerical approach in Hunt et al. (2016b) reproduces the FMR from Hunt et al. (2016a) with the following conclusions: accretion rates and total gas amount in galaxies increases at high redshift, while the gas regulation via star formation and outflows is approximately the same in proportion; star formation is the driver of galaxy mass growth with only minor contribution from galaxy mergers. There has been inconclusive evidence on whether the FMR changes with redshift from stellar and gas-phase metallicities, various samples and methods for deriving the relation (e.g., Salim et al., 2015; Hunt et al., 2016a; Cresci & Maiolino, 2018; and a more detailed review in Maiolino & Mannucci, 2019).

As it turns out, the FMR brings the modelling efforts a step closer to fixing the exact system of physical processes responsible for star formation and galaxy growth. Therefore, it is important to that this relationship holds regardless of possible biases introduced in deriving the relevant physical properties, such as stellar mass and star formation rate. The next chapter investigates the effect of the IMF on these physical properties.

Galaxies in the First Billion Years

Prior to the JWST, considerable effort led to reconstructing the history of star formation across 13 billion years (Madau & Dickinson, 2014; Scoville et al., 2017; Casey et al., 2018; Zavala et al., 2021), producing physical and statistical models of the luminosity functions and stellar mass functions, semi-analytical and numerical simulations of galaxies as complex systems. However, the projections to the earliest stage of galaxy evolution often have been contradictory. It is now possible to test various predictions and investigate the early growth of the first galaxies.

Since the launch of the JWST it has become possible to fill at least some of the remaining observational gaps in the first billion years of galaxy evolution and test the existing models based on studies at lower redshift. Previous sections provided a brief review of how the work done with the HST, Spitzer and other optical and IR facilities pushed the cosmological frontier to $z < 7$ where galaxies would start to drop out in most photometric bands or where the flux sensitivity would limit further probes. The next chapter of extragalactic astronomy is driven by the JWST observations in the $0.6 - 5$ μm range with high sensitivity and spatial resolution which allow studying rest-frame optical continuum and spectroscopic lines at $z \lesssim 15 - 20$. These characteristics can be utilised efficiently with the multi-object observational modes of the camera (NIRCam; Rieke et al., 2023) and spectrograph (NIRSpec; Jakobsen et al., 2022) and a relatively large field of view to observe multiple galaxies in NIR down to 30 AB magnitudes in deep fields, which can be complemented by valuable data from its mid-infrared instrument (MIRI) and by the sub-mm coverage of the Atacama Large Millimetre Array (ALMA).

Soon after the first observations in July 2022, multiple studies have reported finding bright galaxies well into the first few hundred Myr, which outnumber expectations of how rapidly they can grow in the early universe. In particular, the number of bright objects is consistent with little evolution of the bright end of the UV LF (Castellano et al., 2022; Naidu et al., 2022). Based on more sizeable samples at $z > 9$ with $M_V < -20$ galaxies appear to be $\sim 2 - 10$ times more frequent than expected from simulations (Adams et al., 2023a; Atek et al., 2023a; Donnan et al., 2023; Yan et al., 2023; Finkelstein et al., 2023; Whitler et al., 2023a; Harikane et al., 2023) and from extrapolations of some lower redshift models (Mason et al., 2015; Bouwens et al., 2021). Contrary to predictions of Oesch et al. (2018), the bright end of the UV LF at $z > 9$ does not drop off rapidly, but continues to decline exponentially and is best described as a double power law rather than the Schechter function (e.g., as discussed in Bowler et al., 2020. Interestingly, the bright end of the UV LF and high end of the SFRD may become shallower above $z \sim 11 - 12$ as found by Harikane et al. (2023); Finkelstein et al. (2023). Although lacking high statistical significance, these findings can suggest extremely blue UV slopes of these galaxies and therefore possibly lack of dust and distinct stellar populations at $z > 10$.

Later work showed that the large UV luminosities during the cosmic dawn are likely not caused by extremely blue UV continuum slopes β which leaves uncertainty about the types of stars ionizing the H II regions and the ISM. According to photometric SED models, the typical slopes of galaxies at $z \gtrsim 9$ vary in the range $-1.6 \lesssim \beta \lesssim -2.5$ and are on average slightly bluer than their $z > 5$ descendants (e.g. in Finkelstein et al., 2012) by $\Delta\beta = -0.38 \pm 0.09$ (Dunlop et al., 2013; Bhatawdekar & Conselice, 2021; Tacchella et al., 2022; Cullen et al., 2023; Whitler et al., 2023b). Only a small number of very blue slopes have been identified recently ($\beta \approx -3$ in Topping et al., 2022), with most other cases (e.g., in Bouwens et al., 2010) being uncertain (e.g., Dunlop et al., 2012; Bouwens et al., 2012). On one hand, this may suggest that a typical bright galaxy shows recent star formation with little dust extinction and likely a low stellar metallicity. On the contrary, if some of these galaxies have unusually strong nebular emission, the same intermediate β may be consistent with rare massive stars forming from a low-metallicity gas (Nussbaumer & Schmutz, 1984; Bottorff et al., 2006). In this option, the continuum can redden due to the two-photon excitation in H II regions, which likely results in small escape fractions of ionising radiation. Although the escape fraction of galaxies during reionisation has been hard to constrain (Robertson, 2022), a recent study argues that some galaxies can be uniquely modelled with such nebular continuum model (Cameron et al., 2023b).

Following the initial census of the numbers and luminosities of the early galaxies, there has been extensive evidence that many SED models "calibrated" for galaxies at $z \lesssim 6$ do not accurately explain the observed SEDs towards the cosmic dawn. Stellar masses inferred from the SED models of some candidates reported by Harikane et al. (2023); Labbé et al. (2023) appear to grow above the local ratio $M_{BH}/M_\star \sim 0.01$ (Häring & Rix, 2004) and sometimes exceed it (Boylan-Kolchin, 2023). The "impossibly-massive" candidates are now ruled out with the updated photometric calibrations

(Boyer et al., 2022), accurate spectroscopic redshift estimates (Arrabal Haro et al., 2023; Harikane et al., 2024), and improved constraints of the rest-frame optical continuum and nebular emission lines. As shown in the early science release spectra in Curtis-Lake et al. (2023); Carnall et al. (2023a); Atek et al. (2023b), early galaxies are much more likely to have strong nebular emission than a Balmer break, which can be indiscernible in photometric bands (Adams et al., 2023b; Steinhardt et al., 2023a). [3]

Any remaining tension between the inferred stellar mass and the masses of dark matter halos likely points to either an elevated star formation efficiency (SFE) or a top-heavy IMF. Initially motivated by large UV luminosities, the model of feedback-free starbursts by Dekel et al. (2023) can also explain how star formation proceeds in the early galactic stage. Possible indications of increased SFE come from abundance matching (e.g., Finkelstein et al., 2015b) or from the possibly "overpopulated" high-end of the stellar mass functions (Davidzon et al., 2017; Weaver et al., 2023), however it remains to be tested. An orthogonal hypothesis is that the IMF is distinct at high redshift and produces more intermediate mass or massive stars that can solve the problem of luminosities and masses by decreasing the mass-to-light ratio of galaxies. This assumption produces a better match to the bright end of the luminosity functions in numerical simulations (Yung et al., 2023) and in theory can fully explain the excessive stellar mass (Harikane et al., 2023) if the IMF is driven by, for example the cosmic microwave background (Steinhardt et al., 2023a). At this time neither solution is ruled out and some combination of two processes is possible.

However, by this time, several other pieces of evidence have been published that can point in the direction of the top-heavy IMF idea. As described in more detail in Section 2.3, several observational results suggest that the distribution of stellar masses varies with redshift: In the present epoch, kinematics and metallicities of stars in the early-type galaxies, which are believed to be the latest stage of galaxy evolution, suggest a bottom-heavy IMF in their most recent stage of star formation (Conroy & van Dokkum, 2012); at the cosmic noon, delay-time distributions of Type Ia

---

[3] In fact, the Balmer break, which is indicative of late B and AF-type stars, has been suggested as an observable to test predictions of the ΛCDM: assuming that galaxies in the first billion years do not stop forming stars for as long as 100 Myr, Steinhardt et al. (2023c) predicted that the earliest breaks can be expected at $z < 7$. So far, quiescent candidates have been discovered only as early as $z = 4.68$ (Carnall et al., 2023b) and $z = 5.2$ (Strait et al., 2023). This both supports the cosmological predictions, as well as shows that even if star formation is regulated by feedback processes in the galaxies detected at higher redshift, it is resilient on sufficiently long timescales, in agreement with simulations (McCaffrey et al., 2023).

supernovae in early-types galaxies highlight an excess of white dwarfs that is consistent with an intermediate-heavy IMF at $z > 3$ (Freundlich & Maoz, 2021); during the cosmic dawn, [N/O] and [C/O] exceed solar abundances by ~ 10 times in a galaxy at $z = 10.6$ (Bunker et al., 2023; Cameron et al., 2023a) which among several existing hypotheses could be caused an intermediate or a top-heavy IMF (Bekki & Tsujimoto, 2023); finally, sub-mm observations with ALMA reveal extremely high-ionization sources at $z > 6$ which appear to be common (Harikane et al., 2020) and their origin may be linked either to the properties of massive stellar populations or active galactic nuclei. Different ideas exist how to explain the IMF with physical conditions of the star-forming gas and some form of variation of the stellar mass distribution is likely due to some combination of changes in metallicity, temperature and density of the gas (Bromm & Larson, 2004; Jermyn et al., 2018).

Chapter 2 sets the goal to investigate potential variations in the assumption of the stellar IMF by using population-level properties of galaxies across the previous 10 billion years of evolution. After there has been substantive evidence of IMF-driven variations in mass-to-light from case studies (more examples are discussed in Section 2.3), this work takes a statistical approach to constraining IMF in a large photometric sample of galaxies. As it is shown later, there is a possibility that the IMF varies systematically with redshift by becoming increasingly top-heavy with lookback time in star-forming galaxies, with starburst galaxies exhibiting the most similar properties to the galaxies at high redshift. This work also demonstrates that the mass-to-light changes play an important role in reevaluating the physical properties of galaxies and making sharper the interpretation of the stellar mass assembly in terms of mass downsizing. Future work that follows-up on the spectroscopic properties of the photometrically-constrained stellar populations can test these results and help to understand more accurately the physical connections between the gas-phase and stellar populations.

1.2 Modelling Stellar Light of Galaxies

Models of spectral energy distributions of galaxies are extremely valuable for estimating cosmological redshift from photometry and reconstructing physical properties of a galaxy, but they are complicated and include a wide range of assumptions about the typical stellar populations in the galaxy, the interstellar and intergalactic medium, presence of an AGN and dust and the cosmic history of star formation. As most of these assumptions are not directly testable and the available data often allows just a few statistical degrees of freedom, it is important to carefully select the models. Generally, the simplest models can be constructed by using templates of pre-selected well-measured galaxies that can be representative of a larger population. A more detailed and common approach involves modelling an SED from the first principles, which involves assuming an initial mass function, modelling a simple stellar population using stellar spectra and isochrones (through stellar population synthesis, SPS, models Bruzual A. & Charlot, 1993; Leitherer et al., 1999; Anders & Fritze-v. Alvensleben, 2003; Bruzual & Charlot, 2003; Maraston, 2005), evolving the system over a star formation and chemical evolution history and applying the remaining dust and AGN components. These steps will be reviewed briefly in the sections below (a detailed review of various ingredients and their limitations is given in Conroy, 2013a).

Galaxy-wide Stellar Population

One of the key processes determining to the shape of an SED continuum and various emission and absorption features is star formation. On the scale of giant molecular clouds ($\sim 10-100$ pc) star formation starts from the collapse of dynamically cool gas on a free-fall timescale (~ 30 Myr in the Milky Way in Murray, 2011). During this process, gas fragments and subsequently collapses into multiple stellar cores which form a stellar population. As the efficiency of converting gas into stars ranges between $0.2-20$ % in the Milky Way (Murray, 2011) and $\sim 5-15\%$, as estimated in extragalactic studies of the ISM or from abundance matching (Stefanon et al., 2017; Finkelstein et al., 2015b), most of the gas remains unused and some returns to the ISM after most massive stars explode. Therefore, this process can last until most of the gas is depleted or until interrupted by various feedback processes, including active galactic nuclei or star formation itself.

Star formation can be quantified by starting with a simple stellar population (SSP) which is a coeval group of stars with the same metallicity that acts as a unit stellar population. Every star is described by an effective surface temperature, surface gravity and stellar mass that result in a unique stellar spectrum that can be either produced from observations of stars in the Milky Way or using models with atomic and molecular line tables scaled by chemical abundances. An SED of the whole population can be produced by integrating over the distribution of stellar masses assumed at birth, called the stellar initial mass function (IMF). It is commonly assumed that the IMF is universal and usually one of its common empirical forms is used in local or extragalactic studies.

The exact SED of every galaxy is a composite of the SEDs of individual star-forming clouds that can form in multiple locations at different times in a galaxy. As it is impossible to resolve individual stellar groups in most extragalactic studies, it is necessary to assume that stars forming in a range of gas-phase conditions across an individual galaxy can be represented by an average stellar population with one age, metallicity and IMF (Weidner & Kroupa, 2005). The total stellar emission in the UV and optical is usually attenuated by dust grains (an example is shown in Figure 1.6). After being heated by the young stars, dust in the stellar birth clouds produces hot emission in the NIR, while dust component in the ISM being heated by the ambient radiation field produces a cooler component.

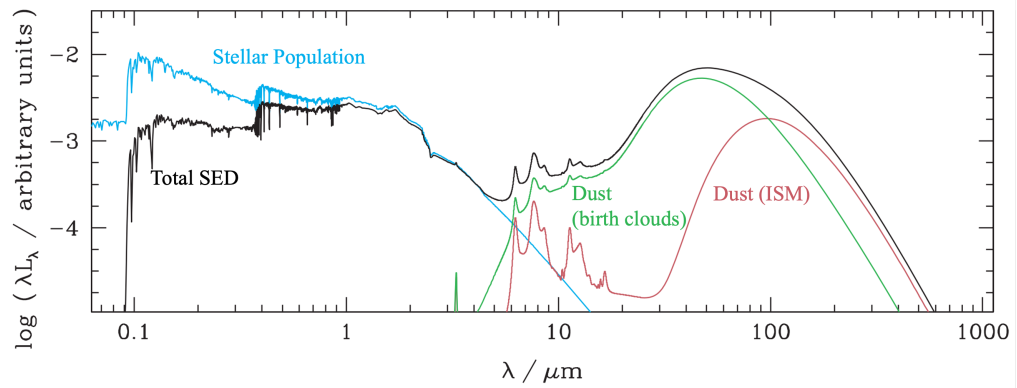

Figure 1.6: An example model of a starburst galaxy with a dust component. The figure shows: stellar population component (blue), dust emission from stellar birth clouds (green), dust emission from the ambient ISM (red), total SED model which includes the attenuated stellar population (black). Adapted from da Cunha et al. (2008).

Accurately inferring physical properties from total galaxy SED depends on the ability to constrain the SFH and the IMF of a galaxy, as they detemine colour and brightness of galaxies (Conroy, 2013b). For example, a decreasing SFR can be misinterpreted as an IMF with a steeper (i.e. top-lighter) high-mass slope. Even with a fixed IMF, studies of resolved observations (Sorba & Sawicki, 2015, 2018; Giménez-Arteaga et al., 2023) and numerical simulations (Narayanan et al., 2024) of galaxies find that the model constraints based on the integrated photometry are dominated by the stellar light of the most recent star formation event. To a large extent this effect can be mitigated by sampling NIR tail of the old and intermediate-age stellar populations (Song et al., 2023). Furthermore, recent work by Sneppen et al. (2022) argues that in addition to the NIR and overall dense wavelength coverage, deepest observations (signal-to-noise $S/N > 10 - 100$

per integrated flux of a galaxy) allow to alleviate the degeneracy between the SFH and IMF.

Stellar Initial Mass Function

Extragalactic studies make a common assumption about the integrated stellar light of distant galaxies: stars are born with the same distribution of mass in all galaxies as in the Milky Way (MW). It is postulated as the universal stellar initial mass function (IMF; e.g., Kroupa, 2001). The low-mass end of the IMF determines most of the stellar mass in a galaxy, the intermediate-mass stars strongly contribute to the metallicity of the interstellar medium, while the massive end dominates the stellar energy output. Therefore, the relative abundance of stars of different types in the spectrum of stellar mass is a fundamental property that connects stellar populations to galaxy evolution. It underlies the properties inferred from stellar light: stellar mass, star formation rate, stellar metallicity and the amount and strength of the ionizing radiation.

Is the IMF indeed universal given possible differences in the environments of star formation across gas clouds, galaxy populations and cosmic times? Theoretical considerations show that the IMF may be set by a range of physical conditions: the Jeans mass (Larson, 1998); stochastic processes (Elmegreen, 2006); feedback of the first most massive stars (Silk, 1995); or physics of turbulent interstellar medium (Hopkins, 2012). Whether the IMF is determined by any or all of the processes, strong differences in molecular gas conditions likely may affect affect the final distribution function. The MW IMF is canonically represented as a single (Salpeter, 1955) or multi-component power law (Kroupa, 2001) with the mass m segment of the linear form with the exponent α:

$$\phi(m) = dN/dm \propto m^{-\alpha}. \tag{1.3}$$

Alternatively, it has been approximated as a log-normal distribution function by the central limit theorem assuming that star formation results from a combination of many independently distributed variables (Miller & Scalo, 1979; Adams & Fatuzzo, 1996; Chabrier, 2003), as demonstrated in Figure 1.7.

Various studies find evidence pointing to IMF-driven variations in the mass-to-light ratio increasing towards high redshift. Chemical abundances of stars in the early-type galaxies suggest a bottom-heavy IMF in their

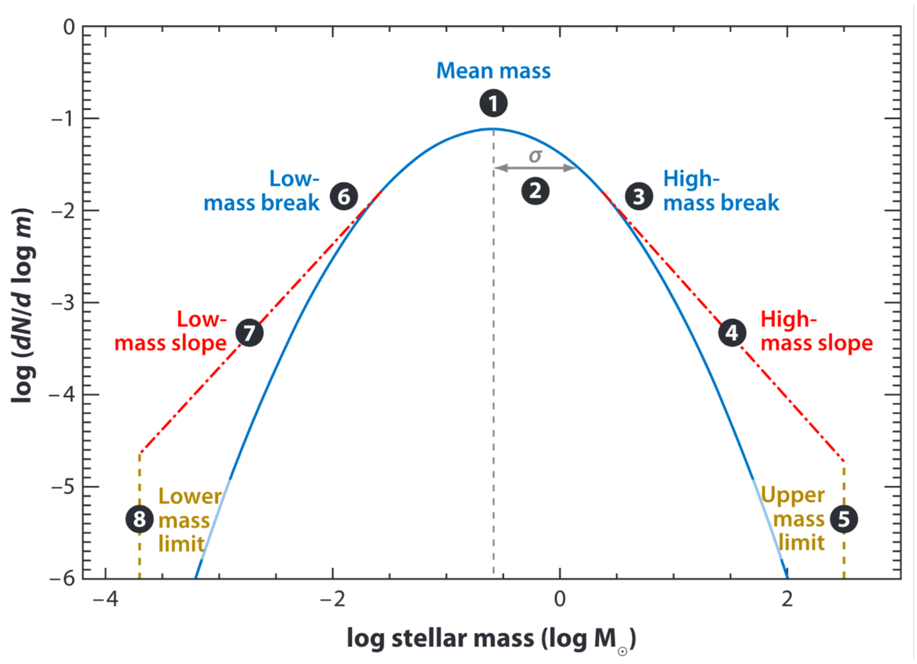

Figure 1.7: The log-normal shape of the IMF assuming it results from many independent physical and statistical processes by the central limit theorem. This shape is used in several formulations, such as in Miller & Scalo (1979); Adams & Fatuzzo (1996); Chabrier (2003). Figure is taken from Bastian et al. (2010).

most recent stage of star formation (Conroy & van Dokkum, 2012). On the other hand, based on delay-time distributions of Type Ia supernovae, the early-type galaxies are found to have an excess of white dwarfs indicative of an intermediate-heavy IMF at $z > 3$ (Freundlich & Maoz, 2021). Finally, super-solar abundance $[N/O]$ in a galaxy at $z = 10.6$ points to possible excess in the number of intermediate-mass (Pettini et al., 2008) or massive stars (Bekki & Tsujimoto, 2023; Nandal et al., 2024), which may soon motivate searches of similar traces in other galaxies at high redshift. These hints from case studies of galaxies at different times in the universe may provide a pivoted framework for systematic changes in the process of star formation.

In addition to the possible evolution with redshift, hints of IMF variations come from different evolutionary types of galaxies. Studies of old regions in the MW and local dwarf galaxies find evidence of a more bottom-heavy IMF compared to the canonical MW versions (Hallakoun & Maoz, 2021). These findings are similar to mass-to-light ratio constraints in early-type galaxies from absorption features specific to low or high-mass stars (van Dokkum & Conroy, 2012; Conroy & van Dokkum, 2012; Zhang et al., 2018). Moreover, the dynamical mass measurements of the early-type galaxies from gravitational lensing indicate a similarly bottom-heavy IMF even as far back as $z = 2$ (van Dokkum et al., 2024).

On the other hand, a lot of mixed evidence is found regarding the stellar mass function in various environments locally and extraglactically. For example, in young (a few Myr) star clusters with large stellar density in the Milky Way (Figer et al., 1999; Stolte et al., 2002; Kim et al., 2006) and Magellanic Clouds (Mackey & Gilmore, 2003), the mass function above ~ 1 $\mathrm{M}_{\odot}$ is found to be flatter than the Salpeter IMF. Although, some young stellar systems (e.g., NGC3603 in Nürnberger & Petr-Gotzens, 2002; Sung & Bessell, 2004; Stolte et al., 2006) and the dense Galactic centre (Bartko et al., 2010) are consistent with the canonical mass functions at the high-mass end. In addition, it is possible that the sub-solar mass function in these systems may be suppressed due to the feedback from the younger stars (McKee & Ostriker, 2007), although there have been only uncertain indications about the lack of the small stars from indirect methods (Nayakshin & Sunyaev, 2005) and the exact physical timescales for low-to-high mass stellar formation remain unknown. In turn, the high mass function end has been found consistent with the MW IMF in the studies of chemical abundances sensitive to stars of different mass in extragalactic H II regions and damped Ly-alpha galaxies (DLA) at around the cosmic noon (Pettini et al., 2000; Molaro et al., 2001; Pettini et al., 2008).

Although the tests of IMF variations have proven to be extremely challenging, most opposing arguments do not appear in direct contradiction. So far, there appears to be consensus regarding the older and more metal-rich systems (MW thick disc, early-type galaxies locally and up to $z \sim 2$) producing more low-mass stars canonically in the MW. Such effect could be explained by high gas metallicity and the lack of gas in the star clusters which can decrease an upper limit on the IMF (at least in the statistical sense) (Bruzual & Charlot, 2003; Larsen, 2006). Regarding the studies of young star-forming systems, differences in the upper end of the IMF are inconclusive, which may be either due to a large scatter in star-forming conditions in the local universe or that conditions of star formation in the local universe do not appear to be sufficiently extreme where the average cosmic star-formation rate density declines (e.g., lower rate of gas inflows and higher gas metallicity). At higher redshift ($z \sim 2-3$), the stellar type-specific relative abundances of C and O isotopes “locked” in the ISM of the sub-millimetre galaxies are solved for with a top-heavy IMF and no meaningful star formation history-MW IMF combinations (Zhang et al., 2018), while the [N/O] chemical abundances in DLAs at $2 < z < 4$ (Pettini et al., 2000, 2008) can be reproduced by varying star formation histories alone, making this approach less useful for IMF measurements.

The goal of the work presented in Chapter 2 is to expand the work on testing the IMF universality from predominantly small-sample case studies to a large sample which includes representative populations of active and passive galaxies across several billion years of the cosmic history.

1.3 Thesis Outline

This work investigates several directions within the topic of galaxy evolution that include composite stellar populations in normal star-forming environments of galaxies at different epochs and the possibility of star formation inside energetic active galactic nuclei. It also shows that the average star-forming conditions in a galaxy may be related to the morphological properties of galaxies. The common theme that runs through all of the chapters is the fundamental process of star formation which acts as a lifeline connecting small-scale physics and chemistry with the global evolution of galaxies and matter in the universe. The focus of the following chapters can be outlined by the following research questions:

- Do spectral energy distributions of galaxies hold information about the stellar IMF?
- Does the IMF vary systematically across cosmic epochs and galaxy populations?
- Do analogues of active galaxies at cosmic dawn exist in the local universe and at the cosmic noon?
- Can the potential IMF constraints from the cosmic noon explain the unusual properties of the galaxies in the first billion years?
- What are the missing physical processes describing the physics of the gas surrounding supermassive black holes? Can they shed more light on the extreme star-forming conditions in the early galaxies at high redshift?

This work addresses the questions, presents possible answers and suggests the next steps. Although it may make some of the right steps in that direction, these questions have been explored by the astrophysical community for decades and deserve a much more detailed approach than could be achieved in the course of this PhD. There is no doubt that exciting prospects await to either disprove or validate the ideas and results and to resolve existing extragalactic problems in the future.

Chapter 2 reiterates the motivation for including the IMF in the modelling framework of galaxies, describes the simple framework adopted here and the results of the experiment as well as their implications for some of the key galaxy observables and relations presented in Chapter 1. Chapter 3 reports extraordinary observations of one quasar, describes it in the context of existing phenomenological and theoretical models of quasars and provides a new interpretation for the nature of the observed spectroscopic features.

Finally, Chapter 4 briefly return to the broad picture and describes the results of this work in that context. It also mentions other ongoing work and outlines possible future directions for the work presented here before providing the final conclusion.

Chapter 2

Variations of the Stellar Initial Mass Function

This chapter contains the following journal article:

> **"A Value-added COSMOS2020 Catalog of Physical Properties: Constraining Temperature-dependent Initial Mass Function"**
>
> Published in The Astrophysical Journal Supplement Series (ApJS), Volume 268, Issue 1, id.10, 18 pages, September 2023.
>
> Authors: Vadim Rusakov, Charles L. Steinhardt, Albert Sneppen.

The chapter also contains materials from the following journal article:

> **"The Earliest Stage of Galactic Star Formation"**
>
> Published in The Astrophysical Journal Letters (ApJL), Volume 949, Issue 2, id.L38, 8 pages, June 2023.
>
> Authors: Charles L. Steinhardt, Vadim Rusakov, Thomas H. Clark, Andrei Diaconu, John Forbes, Conor McPartland, Albert Sneppen, John Weaver.

Abstract

This work presents and releases a catalog of new photometrically derived physical properties for the $\sim 10^5$ most well-measured galaxies in the COSMOS field on the sky. Using a recently developed technique, spectral energy distributions are modeled assuming a stellar initial mass function (IMF) that depends on the temperature of gas in star-forming regions. The method is applied to the largest current sample of high-quality panchromatic photometry, the COSMOS2020 catalog, that allows for testing this assumption. It is found that the galaxies exhibit a continuum of IMF and gas temperatures, most of which are bottom-lighter than measured in the Milky Way. As a consequence, the stellar masses and star formation rates of most galaxies here are found to be lower than those measured by traditional techniques in the COSMOS2020 catalog by factors of $\sim 1.6 - 3.5$ and $2.5 - 70.0$, respectively, with the change being the strongest for the most active galaxies. The resulting physical properties provide new insights into variation of the IMF-derived gas temperature along the star-forming main sequence and at quiescence, produce a sharp and coherent picture of downsizing, as seen from the stellar mass functions, and hint at a possible high-temperature and high-density stage of early galactic evolution.

2.1 Introduction

Most galaxies outside of the Local Group are studied by fitting photometric templates with known physical properties. These templates rely on strong assumptions about the formation and evolution of stellar populations (Conroy, 2013b). The problem is complicated, as most of the starlight is integrated and comes from the high-mass stars that compose a small fraction of its total stellar mass. Typically in models, the stellar population is produced by some form of a Galactic stellar initial mass function (IMF; such as Salpeter, 1955; Miller & Scalo, 1979; Kroupa, 2001; Chabrier, 2003) combined with a specific star formation history and dust extinction. Although the IMF is constrained fairly well in the locality of the Milky Way (MW), where it is possible to resolve individual stars, the same task is impossible for distant enough galaxies. Therefore, as this assumption fixes a certain stellar budget for galaxies, it is crucial that it holds so that the physical properties are estimated accurately. Otherwise, it can break the results and the interpretation of different stages of galaxy evolution.

Several observations have hinted that models of integrated starlight calibrated against stellar populations in the local universe may sometimes fail at increasingly high redshift. Large galaxy surveys (Hildebrandt et al., 2009; Caputi et al., 2015; Finkelstein et al., 2015b; Steinhardt et al., 2016) have reported that dark matter halos inferred from stellar masses at high redshift become too massive to fit cosmological predictions. Furthermore, recent observations of galaxies at $z > 8$ (Naidu et al., 2022; Atek et al., 2023a; Labbé et al., 2023, among others) have revealed that by drawing from the same stellar budget they require more baryons than there are produced at that time (Boylan-Kolchin, 2023). At the same time, the observed luminosity functions have been under-predicted in some of the semi-analytical simulations at $z > 13$ by a factor of 30[1].

On the other hand, low-redshift observations sensitive to low-mass stars hint at underestimated stellar mass in early-type galaxies. For example, measurements of stellar kinematics, absorption lines or various line indices find excess in mass-to-light ratio in local elliptical galaxies relative to the Milky Way IMF (Cappellari et al., 2012; Conroy & van Dokkum, 2012; van Dokkum & Conroy, 2012; Martín-Navarro et al., 2015; van Dokkum et al., 2017a). Other observations of resolved stellar populations in the MW or local dwarfs demonstrate similar IMF results in old stellar structures (Geha et al., 2013; Hallakoun & Maoz, 2021).

Together, these pieces of evidence independently suggest that the mass-to-light ratio in galaxy models appears to be off in the edge cases with drastically different star-forming conditions. It is too high for active galaxies at high redshift and too conservative for passive ones at low redshift. At the same time the galaxy populations with intermediate properties likely represent the bulk of the distribution.

In the high redshift cases where the tension with the cosmology arises, Steinhardt et al. (2023a) and Harikane et al. (2023) suggested that a bottom-lighter (or top-heavier) IMF can account for the over-estimation of stellar mass inferred from observations. Jermyn et al. (2018) and Steinhardt et al. (2023a) proposed that the bottom-light IMF at high redshift is likely driven by the cosmic microwave background (CMB) temperature. Similarly, Yung et al. (2023) proposed that the simulations can match the higher galaxy number densities with a top-heavier IMF. It was also possible to resolve the tension by more properly accounting for

---

[1] It is worth mentioning that other studies have not reported the tension with interpreted or simulated galaxy properties (Adams et al., 2023b; McCaffrey et al., 2023). Others have indicated that it can be resolved by changing assumptions in galaxy models (Yung et al., 2023). Therefore, the apparent nature of the tension reinforces the fact that it is likely a test of the galaxy models and not the cosmology.

cosmic variance, uncertainty in the stellar mass and accounting for possible additional gas for star formation (Chen et al., 2023).

Consequently, one could also argue for a more bottom-heavy IMF to solve the tension on the other redshift end (in the local universe) to account for the reported under-estimation of stellar mass in the early-type galaxies. This would be in agreement with the IMF measurements of Cappellari et al. (2012); Conroy & van Dokkum (2012); van Dokkum & Conroy (2012); Martín-Navarro et al. (2015); van Dokkum et al. (2017a). Therefore, if the shape of the IMF varies with average conditions of star formation in different galaxies, there is likely to be a continuum of stellar mass functions.

In theory, changes in temperature, density or metallicity of the star-forming material must lead to a corresponding change in the relevant mass scales of the stellar population (Jeans, 1902; Low & Lynden-Bell, 1976; Larson, 1998, 2005) and modify the shape of the IMF (Bate & Bonnell, 2005; Jappsen et al., 2005; Krumholz, 2011; Hopkins, 2012; Jermyn et al., 2018). Although, the star-forming gas conditions have been difficult to determine from line ratios at high redshift, the temperature of cold dust serves as a strong indicator of conditions of the interstellar medium (ISM). A possible link between the thermal state of the gas and dust in the main-sequence galaxies has been shown by comparing mass and luminosity-weighted dust temperatures with excitation temperature from [C I] line ratio (Valentino et al., 2020).

Empirically, measurements of dust temperature hint that the state of the ISM (and possibly the star-forming gas) changes with redshift and position with respect to the star-forming main sequence (SFMS; Magnelli et al., 2014; Lamperti et al., 2019). The latter studies show that the temperature of the cold component of dust measured from the far-IR (FIR) continuum increases from $\sim$ 20 to 40 K for galaxies depending on the offset from the SFMS. In addition, the average dust temperature increases with redshift (Schreiber et al., 2018; Cortzen et al., 2020), which is similar to the reported increase in the intensity of the radiation field at higher redshift (Béthermin et al., 2015; Magdis et al., 2017). If the molecular clouds exhibit similar behavior, this evidence builds to suggest that the IMF should change accordingly (Kroupa, 2001; Bastian et al., 2010).

Moreover, Gunawardhana et al. (2011) and Nanayakkara et al. (2017) show that the excessive equivalent widths of the $H\alpha$ line are likely due to a top-heavier IMF at $z \sim 0.35$ and $z \sim 2$. As this excess correlates with the star formation rate (SFR), they suggest that the effect increases with redshift for star-forming galaxies. In addition, a more direct probe of the

IMF in Zhang et al. (2018) – ^{13}C/^{18}O transitions – reveals a top-heavier IMF in several starbursts at $2 < z < 3$.

The recently introduced technique in Sneppen et al. (2022) was used to constrain the IMF in some of the most well-measured galaxies. However, it has been challenging to test the idea due to rare photometric band coverage and relatively low quality of available measurements. Therefore, most samples are prone to the strong covariances between various model parameters. As such, the lack of emission from the bulk of stellar mass leads to degeneracies between the IMF, the law of dust attenuation or the star formation history. However, Sneppen et al. (2022) showed that improved measurements in the recent data sets (such as COSMOS2015; Laigle et al., 2016) can provide more statistical power to relax the assumption of the local IMF and break the existing degeneracies to some extent.

This work employs the fitting technique to produce a catalog of new physical properties for galaxies in the COSMOS field, available for use by the community. It is expected that new higher quality observations released in the COSMOS2020 catalog (Weaver et al., 2022) can reveal fainter galaxies across a range of redshifts, as well as refine the observations of the previous catalogs. With these data, it is possible to improve on the estimates of stellar mass ($M_\star$) and SFR, by starting with the, possibly, more physically plausible set of assumptions for the stellar IMF. In addition, this update provides the IMF property theoretically related to the temperature of the star-forming gas (Jermyn et al., 2018) and argues for its importance for galaxy evolution. The work here shows that the measured change in stellar mass and star formation rate and the associated increase in the inferred gas temperature at lower redshifts ($0 < z < 2$) reinforces the importance of the proper treatment of stellar populations particularly at high redshift, where the cosmological predictions can be tested in the most direct way.

The data used in this work are described in § 2.2. Next, § 2.3 outlines the procedure of SED fitting, which includes the description of the temperature-dependent IMF and the associated templates. Then, § 2.4 details the quality choices made to produce the final data set and demonstrates the best-fit physical properties. The following subsections demonstrate some well-known relationships with the new properties and describe new insights driven by the best-fit IMF. Finally, the discussion in § 2.7 reiterates some of the most critical approximations made when interpreting observations in application to galaxy evolution. This work assumes a Flat Lambda Cold Dark Matter cosmology ($H_0 = 70$ km s^{-1} Mpc^{-1}, $\Omega_m = 0.3$, $\Omega_\Lambda = 0.7$).

2.2 Data catalog

Previously, work to constrain the IMF using this technique was done with the COSMOS2015 catalog (Laigle et al., 2016) in Sneppen et al. (2022), which when published was the largest existing multi-band photometric data set. COSMOS2020 (Weaver et al., 2022) is an updated catalog with more detections and deeper and more precise photometry than the previous versions in the COSMOS field (Capak et al., 2007; Scoville et al., 2007; Ilbert et al., 2009, 2013; Laigle et al., 2016). The most significant advantages arise from deeper infrared bands and from including bluer bands in its detection image. The latter is expected to result in a higher number of small blue galaxies, which is particularly useful for this work, where compact blue galaxies are of special interest, as discussed in § 2.4.

There are two primary versions of the COSMOS2020 catalog, `CLASSIC` and `FARMER`. This work makes use of the `CLASSIC` version, which is preferred for the brightest galaxies. In contrast to the modeled fluxes in the `FARMER` version, it derives aperture-based photometry from PSF-homogenized images similarly to the previous catalogs. Despite the differences in approach, the precision of measurements and the fraction of outliers in terms of photometric redshifts are similar between them on average. For the brightest galaxies `CLASSIC` performs marginally better both in precision and number of redshift outliers using the standard photometric fitting procedure.

The photometric bands were selected as per the suggestions in Weaver et al. (2022). Several filters were discarded as too shallow and thus not providing additional constraints: Spitzer/IRAC Channels 3 and 4; Subaru Suprime-Cam (SC) broad bands, $NB711$, $NB816$, $NB118$; and GALEX FUV and NUV. The final list of photometric bands included 25 filters: Canada France Hawaii Telescope (CFHT) u, u^*; five Subaru/Hyper Suprime-Cam (HSC) bands $grizy$; four UltraVISTA DR4 bands $YJHK_S$; twelve Subaru/Suprime-Cam (SC) bands $IB427$, $IB464$, $IA484$, $IB505$, $IA527$, $IB574$, $IA624$, $IA679$, $IB709$, $IA738$, $IA767$, $IB827$; and Spitzer/IRAC channels 1, 2. The work makes use of the deeper fluxes derived with the 2-arcsecond apertures. The photometry was corrected for aperture sizes and the Milky Way extinction based on the offsets provided in the catalog.

To obtain the most accurate and well-measured objects in the COSMOS2020 catalog, several selections were made. Of the 1,720,700 sources, approximately 437,000 were kept by removing the objects that were flagged by `SExtractor`, including sources biased by the bright neighbors, at the boundaries of the images, saturated detections or instances that failed at execution. These sources were selected in “ultradeep” stripes of the UltraVISTA photometry, which reduced the survey area from ~ 3.4 to 0.9 $\deg^2$ and decreases the volume completeness of the final catalog. Further selections of objects were made after solving for SED templates with the best-fit IMF, as some of the poor measurements were found to be most prone to degeneracies in the solutions and ended up at the edges of the IMF temperature range. This quality cut is described in § 2.4.

2.3 SED Fitting with `EAZY`

The algorithm for fitting photometric SEDs with `EAZY` (Brammer et al., 2008; Brammer, 2021) is based on a linear combination of SED templates from a model set. This procedure significantly reduces the computation time, as the best-fit linear combination can be determined via matrix inversion rather than via extended grid sampling.

However, if the set of basis templates is not carefully constructed, the best-fit linear combination may produce an nonphysical shortcut solution. This is possible as almost all of the resulting solutions are represented by a linear mixture of young and old stellar populations with varying amounts of dust. Even if the problem is well-determined, statistically, the ultraviolet and infrared components of observed SEDs can be reconstructed with different combinations of dust, star formation history and the shape of the IMF. Thus, for example, a quiescent galaxy at may be fitted with an SED of a dusty star-forming galaxy at lower redshift, unless the strong emission lines can be sampled by a fortunate coincidence of some narrow bands.

Therefore, it is crucial to construct a set of model templates to match the prior expectations of physical properties of galaxies in the targeted redshift regime. The templates are typically made to span a limited and physically-motivated space of such parameters, e.g., stellar metallicity, age and dust extinction. On the other hand, the spanned space is also made substantially large to sample the properties as much as possible and avoid forcing most of the inferred galaxy properties to look the same. The balance between asserting a narrow physical domain of templates and still obtaining a representative fit is achieved by ensuring that the template galaxies efficiently span the color space (Brammer et al., 2008). This work builds on the templates provided for COSMOS2020 at the time of publication[2].

---

[2] Standard COSMOS2020 templates made with a Chabrier IMF are available at: `https://github.com/gbrammer/eazy-photoz/`.

Temperature-dependent IMF

It is likely that different phases of gas in the giant molecular clouds result in IMF variability across individual galaxies at different physical locations and at different times of their evolution. Various dependencies of the IMF on the gas phase have been proposed (Bate & Bonnell, 2005; Jappsen et al., 2005; Hopkins, 2012; Krumholz, 2011), where some of the simplest approaches use the scaling of the IMF mass with the temperature only (Jermyn et al., 2018). The mass scale of cloud fragmentation in the Kroupa IMF (Kroupa, 2001) is made proportional to the square of the temperature:

$$\frac{dN}{dm}(T) \propto \begin{cases} m^{-0.3},\ m < 0.08M_\odot f(T) \\ m^{-1.3},\ 0.08M_\odot f(T) < m < 0.50M_\odot f(T) \\ m^{-2.3},\ 0.50M_\odot f(T) < m \end{cases}, \tag{2.1}$$

where $f(T) = (T/T_0)^2$ is the scaling factor and $T_0 = 20$ K is the reference temperature set to approximately the temperature of the molecular clouds in the Milky Way (Schnee et al., 2008). The scaling of the power-law breakpoints is tied to the minimum fragmentation mass of a gas cloud, i.e. the low-mass end of the IMF (Jermyn et al., 2018). Therefore, throughout this paper we refer to the relative IMF changes as bottom-light or bottom-heavy, although in practice the bottom-light(heavy) and top-heavy(light) shapes are degenerate here, as the power-law slopes are fixed.

Although it is unclear precisely how the complex interplay of various astrophysical mechanisms in molecular clouds sets their exact temperature, perhaps, a minimum at $z > 7$ is set by the CMB, where it exceeds the local temperature of 20 K. At lower redshifts, where the temperature exceeds the microwave background, as for the ~ 20 K in star-formirng regions of the Milky Way, it could be regulated by stellar radiation in regular main-sequence galaxies or by cosmic rays in stellar explosions (Papadopoulos, 2010).

Although theoretically, the IMF is parameterised using the gas temperature, it is unclear whether the best-fit IMF constrains this quantity or is degenerate with other model SED inputs. For example, it was argued by Steinhardt et al. (2022a) that the SED templates with a parametrised IMF are likely sensitive to either the sharp decline in the star formation history or just the IMF as the first order effect. There is less confidence that either of these can directly translate to the temperature of the molecular gas. However, the SFMS is found to correlate with the IMF similarly to the temperature of dust with redshift in Magnelli et al. (2014), which lends more credence to the IMF-temperature interpretation. Moreover, the connection of the IMF temperature to galaxy morphologies in Steinhardt et al. (2023b) further reinforces the physical origin of this property.

Photometric templates used in this work were constructed to have as similar properties as possible to the standard COSMOS2020 templates[3], with the sole exception of changing the IMF. The standard 17 templates span stellar populations with ages from 0.1 to 7 Gyr, dust extinction ranging $\sim 0-2$ magnitudes, a mixture of constant star formation histories (SFH) with specific star formation rate sSFR$\sim 2\times10^{-8}$ yr^{-1} and 1×10^{-12} yr^{-1} and lognormal SFH bursts at 0.1, 0.4, 1.7 and 6.7 Gyr with a width of 0.1 Gyr and the attenuation curve from Kriek & Conroy (2013) (Table 2.1). Building upon this 17-template basis, a series of templates was made with the varying IMF shapes that corresponded to molecular gas temperatures ranging from 10 to 60 K in steps of 1 K. They were produced using `Flexible Stellar Population Synthesis` (`FSPS`) code (Conroy et al., 2009; Conroy & Gunn, 2010) and made available publicly[4].

2.4 Results

Generally, parameters inferred from large photometric surveys are analyzed from the perspective of population statistics, rather than studying individual objects. In part, this is because the fits for any individual galaxy are often not well constrained, with star formation rates particularly poorly-determined. This is even more relevant when the SED fitting is performed with the addition of new parameters, which increases random uncertainty and possibly causes additional degeneracies or strong covariances between parameters. Therefore, it is necessary to consider quality cuts to maximize the statistical confidence of the fit results and identify potential outliers arising from the existing degeneracies. The relevant selections and validation of photometric redshifts are described below. Additionally, the subsections here show some of the well-known relationships, as well as the new ones driven by the change of the IMF shape.

---

[3] The standard templates preserved the records of their parameters, except for the star formation history. Therefore it was adjusted to produce as similar templates here as possible.

[4] The templates with a range of varying IMFs are made publicly available at https://github.com/vvrus/sed-templates.

Table 2.1: Properties of the stellar populations in the 17-template basis of standard templates used with COSMOS2020. The columns show the ID of a template; age of a stellar population; fraction of a solar metallicity $log(Z/Z_\odot)$; and dust extinction in the V band, A_V. The first 7 templates are produced using Padova isochrones with $Z_\odot = 0.019$ and for the last 10 MIST isochrones that assume $Z_\odot = 0.0142$ were used.

ID	Age (Gyr)	$log(Z/Z_\odot)$	A_V
1	0.1	0.0	0.005
2	0.1	0.0	0.5
3	0.1	0.0	0.005
4	0.1	0.0	0.5
5	0.1	0.0	1.0
6	0.1	0.0	2.0
7	0.1	0.0	3.0
8	0.31	0.0	0.005
9	0.31	0.0	1.0
10	0.31	0.0	2.0
11	0.62	0.0	0.005
12	0.62	0.0	1.0
13	0.62	0.0	2.5
14	1.76	0.0	0.005
15	1.76	0.0	1.0
16	7.18	0.0	0.005
17	0.91	0.0	0.005

Quality Cuts

At first, the results of the SED fitting were used to discard poor samples. The data here was cut based on photometric coverage to ensure that constraints on the IMF were as strong as possible. Then, the samples where no solutions could be found or they were poorly defined were discarded.

First, it is crucial to have a sample observed over as broad of a set of bands as possible in order to be able to constrain the solution parameters. Thus, the redshift range was reduced to include objects in the range $0 < z < 2$, as too many photometric bands drop out at $z > 2$.

It was demonstrated in Sneppen et al. (2022), using mock SED observations, that the IMF parameter can be safely recovered only for the objects with the highest S/N ratios and at the IMF temperature above $\sim 20 - 25$

K. Most of the objects in the COSMOS2020 catalog lie near the detection limit and thus have relatively low-quality flux measurements, which results in weaker constraining power for the given number of parameters and, ultimately, inferred physical properties that cannot be trusted. For example, some solutions were often found to be erroneously fit by the most bottom-heavy or bottom-light IMFs or, alternatively, by the IMFs at edges of the sampled T_{IMF} range. As such, some faint quiescent galaxies with high mass-to-light ratio and weak constraints in the UV can be sometimes fitted with the most bottom-heavy IMF or a bottom-light IMF and high dust extinction.

Therefore, Sneppen et al. (2022) and Steinhardt et al. (2022a) defined the quality cut $S/N > 10$ in the Suprime-Cam V band or UltraVISTA K band, at which the number of such objects best fitted at the boundaries of the temperature range dropped significantly to $\sim 10-15\%$. Here, instead most of the objects at the temperature boundaries are discarded as having poorly-defined solutions in their chi-squared landscapes $\chi^2(T_{IMF})$ at $10 < T_{IMF} < 60$ K with steps of 1 K. Specifically, the solutions with $\chi^2_{max} - \chi^2_{min} < 0.1$, $FWHM(T_{IMF}) < 4$ K were discarded. If several solution temperatures were identified, the ones with the largest area $\sum_{T_{IMF}} \chi^2(T_{IMF})$ were selected. As a result, $\sim 250,000$ samples out of $\sim 437,000$ (the 437,000 objects were selected as described in § 2.2) passed with best-fit temperatures, out of which only 60% of objects had $S/N < 10$. The fraction of any S/N at the margins of the temperature range did not exceed 7%. On the other hand, the discarded sample was the noisiest, with 90% of its objects having $S/N < 10$ in K_S flux.

By cutting objects based on the quality of their χ^2 peaks, the final sample comprised 249,494 objects with 205,750 in the range $0 < z < 2$ where they were still covered by most of the photometric bands. The sample was reduced even further to 156,389 objects by flagging the remaining solutions as outliers. Those were identified as faint objects with too low or too high mass-to-light ratios and, thus, likely suffering from degenerate template parameters (more description is included in Appendix 2.9). Alternatively, some objects discarded as outliers had additional local minima, similar to objects identified in Sneppen et al. (2022). They could arise due to incorrectly fitting the highest-mass breakpoint in the Kroupa IMF in galaxies that had recently lost their most massive stars, but still have the intermediate-mass population. Lastly, only 72,805 objects in the catalog have uncertainty in T_{IMF} estimated using the minimum variance bound, as described in § 2.4, as the rest of them had low significance of chi-square solutions. These best objects were used to obtain the results in § 2.4–2.4.

Stellar Mass Completeness

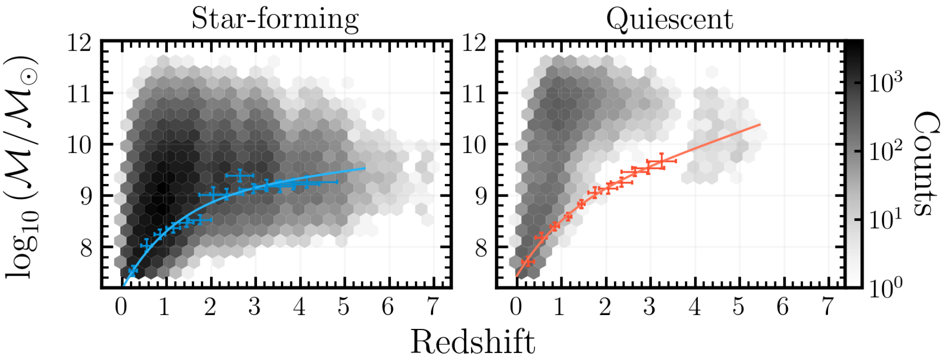

Figure 2.1: Counts of all galaxies in the bins of photometric redshift and stellar mass. The points show 95% mass completeness limits estimated by rescaling down to the detection limit in IRAC Channel 1 for star-forming and quiescent. These limits $\log_{10}\mathcal{M}(z)$ were fitted with a Schechter function and shown as solid lines. The uncertainties are taken as the median errors in bins of redshift and rescaled mass. The levels for star-forming galaxies are below the limits of quiescent galaxies by $0.2-0.3$ dex at $0<z<2$, which reflects the higher $\mathcal{M}/L$ ratio for the passive population.

The lower limit of stellar mass of a representative sample of galaxies depends on the survey depth and the mass-to-light ratio of galaxies and evolves with redshift. Owing to the lack of UV and optical emission per stellar mass, quiescent galaxies are expected to be less complete than the brighter star-forming sample at every redshift in the photometry of COSMOS2020. In addition, it is expected that at $0.0 < z < 2.0$ the galaxy sample is missing a population of blue dwarf galaxies, which fall outside of the detection image, and, possibly, some galaxies at the large stellar mass end at the lowest redshift due to a smaller volume. The separation of galaxies into star-forming and quiescent samples was done in the UVJ color space (Williams et al., 2009; Arnouts et al., 2013).

By using the approach of Pozzetti et al. (2010), the limiting mass was defined by taking the faint objects that are likely to have complete stellar masses in bins of redshift and rescaling their masses to the magnitude of the survey depth. Following the prescriptions in Weaver et al. (2023), 1% of the photometric fits with the largest chi-squared were removed from the sample. Then, the stellar masses $\mathcal{M}$ of the 30% faintest objects in IRAC Channel 1 magnitudes m were rescaled to the detection limit $m' = 26.4 \pm 0.1$ (Weaver et al., 2022) to obtain $\mathcal{M}'$:

$$\log_{10}\mathcal{M}' = \log_{10}\mathcal{M} + 0.4(m - m'). \tag{2.2}$$

Table 2.2: Best-fit parameters and their statistical uncertainties for the Schechter function representing the limits of mass completeness for star-forming and quiescent galaxy samples (see Eq. 2.3).

Sample	$\log_{10}\mathcal{M}^\star$	$z^\star$	α
Star-forming	9.56±0.53	-1.63±0.28	-1.01±0.01
Quiescent	9.10±0.24	-1.89±0.13	-1.03±0.01

The 95% completeness level $\log_{10}\mathcal{M}_{95}$ was taken as the 95th percentile of the $\log_{10}\mathcal{M}'$ distribution and is shown with dots on Figure 2.1. The calculation is done separately for star-forming and quiescent galaxies to account for their different $\mathcal{M}/L$ ratios. The key assumption made here is that galaxies with $\mathcal{M}'$ and $\mathcal{M}$ have the same relation to luminosity. However, as the IMF correlations with the physical properties in § 2.4–2.4 imply, $\mathcal{M}/L$ of star-forming galaxies correlates with the stellar mass and the proper scaling should account for this difference by using $(\mathcal{M}'/L')^{\beta_1}$ and $(\mathcal{M}/L)^{\beta_2}$, where β increases for larger stellar mass (i.e. $\beta_1 > \beta_2$). By assuming that $\beta_1 = \beta_2$, as it is done here, the rescaled stellar mass $\mathcal{M}'$ and, consequently, the mass completeness are overestimated, albeit insignificantly, as the difference between the 30% faintest galaxies in magnitude at the same redshift should be minor. Therefore, the completeness used here acts as conservative upper limit. Finally, although the IRAC bands were not included in the detection image of COSMOS2020, Weaver et al. (2023) argue that this should not affect the results significantly.

The completeness levels were calculated in bins of redshift at $0.1 < z < 3.4$ for quiescent galaxies and $0.1 < z < 4.3$ for star-forming galaxies in steps of 0.3. Finally, the 95% mass completeness levels $\mathcal{M}$ as a function of z were fitted with a Schechter function (Schechter, 1976; shown as solid lines in Figure 2.1; best-fit parameters are shown in Table 2.2):

$$\begin{aligned}\log_{10}\mathcal{M}(z) = {} & (0.4\ln 10)\log_{10}\mathcal{M}^\star \times \\ & \times [10^{0.4(z^\star - z)}]^{\alpha+1}\exp\left(-10^{0.4(z^\star - z)}\right),\end{aligned} \tag{2.3}$$

where uncertainties were taken as median σ_z in the bins of redshift and bins of stellar mass $\sigma_{\log_{10}\mathcal{M}}$ defined as $\log_{10}\mathcal{M}_{95} \pm 0.2\log_{10}\mathcal{M}$.

This work applies two separate 95%-completeness limits to star-forming and quiescent galaxies estimated in Weaver et al. (2023) for all relationships, except the redshift validation in Figure 2.2 and the change of properties due to the IMF modification in Figure 2.4.

Cross-check of Photometric Redshifts

Spectroscopic redshifts have usually been used as a partial validation of photometric template fits. Here, the same check is applied to the variable-IMF fits in the presented catalog. Figure 2.2 demonstrates the correspondence of the sample with the spectroscopic redshifts from the latest Super-deblended catalog (Jin et al., in prep.) and standard photometric redshifts based on Chabrier IMF (at 20 K in the Milky Way) from the COSMOS2020 survey (Weaver et al., 2022). The outliers in the one-to-one comparison are defined as points satisfying the condition $|\Delta z| > 0.15(1 + z)$ (Hildebrandt et al., 2009). The fraction of outliers η is indicated on the plot panels. It shows that the spectroscopic sample disagreed in ~ 3 % of cases, similar to the number outliers in the standard catalog, as shown in Figure 2.2 and in Weaver et al. (2022). The precision of the photo-z is estimated by using the normalized median absolute deviation σ_{NMAD} (Brammer et al., 2008), which is not strongly sensitive to outliers:

$$\sigma_{NMAD} = 1.48 \times median\left(\tfrac{|\Delta z - median(\Delta z)|}{1+z_{spec}}\right). \tag{2.4}$$

Finally, the bias in the estimates is denoted as $b = median(z_{phot} - z_{spec})$. These metrics perform similarly to the standard measurements reported in the COSMOS2020 catalog. The agreement confirms that even more significant differences in templates have little effect on the redshifts reconstructed with the same code (Sneppen et al., 2022). Finally, the outliers identified in Figure 2.2, have been discarded from the scientific results in the rest of the work.

IMF Temperatures

The main result in this work is that most of the galaxies are unlike the local analogs and have bottom-lighter IMFs, as traced by the IMF temperature parameter (Figure 2.3). These best-fit IMFs indicate the larger relative abundance of the most massive stellar populations at all redshifts. Theoretically, this change is expected to correspond to hotter (and, presumably, denser and metal-poorer) molecular gas.

Possible relationships in the distribution of IMF temperatures T_{IMF} at different redshifts z are investigated by fitting an exponential function $T_{IMF}(z) = A \exp(-z/\tau)$ (dashed lines in Figure 2.3). There is not a proper way in the SED-fitting procedure implemented here for estimating uncertainties in temperature, so the errors are calculated using the chi-square

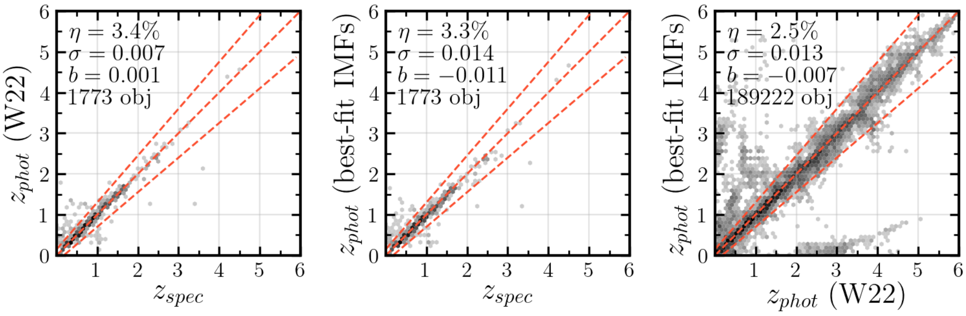

Figure 2.2: Density diagrams showing the validation of photometric redshifts z_{phot} obtained with the best-fit IMFs. Top panel: comparison of redshifts obtained with the Chabrier IMF at 20K (Weaver et al., 2022) against the spectroscopic redshifts z_{spec} from (Jin et al. in prep.) (1,773 objects). Middle panel: redshifts obtained with the Kroupa IMF at the best-fit temperature against the spectroscopic sample. Right panel: comparison of the photometric redshifts z_{phot} obtained with the Kroupa IMF at the best-fit temperature and with the Chabrier IMF at 20 K (189,231 objects). The fraction of higher than one-σ outliers is indicated as η. Overall, the redshifts constrained with the new SED templates appear to be consistent with the standard COSMOS2020 templates and the spectroscopic sample.

χ^2 statistic computed by `EAZY` for best-fit models produced at each IMF temperature in $10 < T_{IMF} < 60$ K in steps of 1 K. By assuming that the temperature estimator is unbiased (at $T_{IMF} \gtrsim 20-25$ K) and using the Minimum Variance Bound, the uncertainty $\hat{\sigma}_{\hat{T}}$ was calculated as $\Delta\hat{T}_-$ and $\Delta\hat{T}_+$ at $\log L(\hat{T} \pm \hat{\sigma}_{\hat{T}}) = \log L_{max} - 1/2$ with the likelihood as $\log L = -2\chi^2$. For the solutions that did not have the sufficient significance, the uncertainty fields in the catalog are left empty. The best-fit function in the total sample (left panel) shows that the temperature increases from ~ 25 K to 35 K at $0 < z < 2$, mostly driven by star-forming galaxies which were selected in UVJ color space (Williams et al., 2009; Arnouts et al., 2013).

Although there is a large scatter in solutions for IMF temperature in the whole sample, there is a systematic trend for increasing temperature at higher redshift. One component of the scatter is added by the fitting procedure and is expected to be mostly random at temperatures above ~ 25 K. Based on the fits of synthetic photometry, Sneppen et al. (2022) showed that scatter in the recovered temperature is $\sigma \approx 5 - 10$ K and the estimator is only slightly biased at those temperatures for the strongest photometric detections, while almost completely inaccurate for "cooler" galaxies (see Figure 13 in their publication). However, it is possible that other unaccounted systematic effects contribute to the obtained temperature distribution. For example, one of the critical limitations of the SED

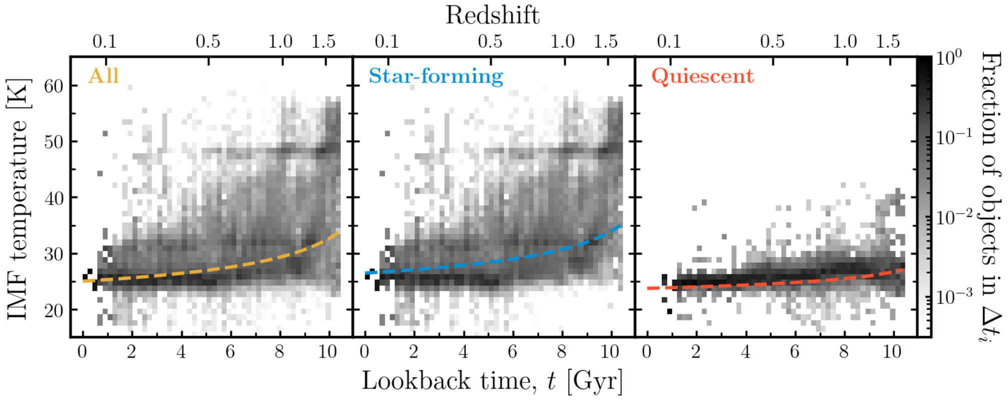

Figure 2.3: The number of objects in bins of IMF temperature and lookback time, normalized in lookback-time bins Δt_i, for the total (left), star-forming (middle) and quiescent sample (right). Dashed lines show best-fit exponentials fit in the space of temperature and redshift (T, z) using individual non-normalized data. Uncertainties in redshift are based on 1σ width of $p(z)$ solutions from `EAZY` (median binned errors range between $\sigma_z \sim 0.01 - 0.27$). The errors in IMF temperature are computed using the likelihood based on chi-squared of the SED solutions, and are very loose (see text for details; median binned errors range between $\sigma_{T_{IMF}} \sim 3-12$ K). Most of the objects have IMF temperature above that of the analogs in the local universe forming a continuum of bottom-lighter IMFs. On average, the best-fit IMF temperature increases with redshift as in Sneppen et al. (2022); Steinhardt et al. (2022b). Finally, the temperature and corresponding IMF behaviour is distinct between active and passive galaxy populations, where the former is almost exclusively responsible for the temperature increase in the total sample. This result for star-forming and quiescent galaxies is consistent with the observed trends in temperature of cold dust in similar redshift ranges (see text for references).

templates employed here is that the temperature, density and metallicity of the star-forming gas are not causally connected to the expected changes in the definition (Eq. 2.1) of the IMF. Therefore, the resulting "temperature" quantity is likely a combination of effects due to these three quantities.

The rest of the scatter appears to be due to the differences in the mass to light ratio, $\mathcal{M}/L$, of stellar populations in different galaxies. For example, the most common and strong distinction exists between active and quiescent galaxies, where the latter are expected to have bottom-heavier IMFs. Indeed, the right panel in Figure 2.3 shows that the passive population is consistent with the same $\mathcal{M}/L$ and has relatively small scatter. Given that the quiescent galaxies with very weak UV emission are expected to be the least sensitive to probing the IMF, this result validates the fitting procedure. This would be consistent with the measurements of dust temperatures in quiescent galaxies that appear to have a lower limit at $T_{dust} \sim 21 \pm 2$ K in a similar redshift range in Magdis et al. (2021). However, it is possible that the temperatures of the star-forming gas and dust are set by different mechanisms in quiescent galaxies and therefore the former does not have to be similarly bounded at $\sim$ 20 K. This possibility cannot be tested with the IMF estimator here, as it is completely biased in that temperature regime. On the other hand, the active population spans the full sampled temperature range at every epoch and is almost entirely consistent with the temperature increase in the total sample.

By isolating the quiescent galaxies, it appears that the large scatter is indicative of various star-forming galaxies. While most appear to be on the main sequence the rest can represent different sub-populations. Among others, ULIRGS that are thought to result from major mergers of gas-rich galaxies or close interactions (from observations Sanders et al., 1991; Solomon et al., 1997; from simulations Mihos & Hernquist, 1996), have been shown to exhibit a constant IMF temperature at $\sim$ 30 K up to $z = 2$ (Sneppen et al., 2022), consistently with dust temperature estimates in Béthermin et al. (2015). Among galaxies efficiently forming new stars are "green peas" (Cardamone et al., 2009) that have small stellar mass and compact morphology, little dust obscuration, and other starbursts that include galaxies with varying physical properties but appear to have similarly high sSFR due to a recently ignited burst of star formation (Kennicutt & Evans, 2012). Based on their properties, these types are likely to occupy the higher temperature tail, above ULIRGS and typical SFMS galaxies. Indeed, Zhang et al. (2018) showed that starbursts at $2 < z < 3$ have a top-heavy IMF by measuring ^{13}C/^{18}O transitions. Note, the density in Figure 2.3 reveals a grid pattern, which is likely due to fits with degenerate parameters, described in Appendix 2.9, that could not be removed entirely.

Finally, the large scatter in the IMF shapes here is in agreement with the broad distribution of equivalent widths of Hα at $z \sim 2$ in Nanayakkara et al. (2017). That work shows that the most likely contribution to the large widths is the top-heavy IMF. Moreover, the large scatter in the widths cannot be explained entirely by the starbursts and likely indicates either stochasticity or some underlying relationships in the shapes of the IMF.

This behavior of the IMF shape is similar to that found using galaxies in COSMOS2015 (Sneppen et al., 2022), although it now extends to fainter galaxies and lower temperatures at the higher redshift and includes galaxies with higher measurement quality on average. In particular, more data fills the lookback time $t > 8$ Gyr ($z > 1.1$) and $T_{IMF} < 30$ K in Figure 2.3. It represents a faint red sample at the lower tail of sSFR or faint blue galaxies, which have been observed owing to the depth of the COSMOS2020 surveys.

Physical Properties of Galaxies

If most studied galaxies have systematically different stellar populations from what was assumed previously, their inferred stellar mass and the rate of star formation must change correspondingly. Figure 2.4 shows the changes in these two properties at $0.2 < z < 2.0$.

Clearly, most of the objects have properties characteristic of the bottom-lighter IMFs, or higher temperature of the star-forming gas. As can be expected, the bias is associated predominantly with the bottom-lighter IMF solutions for the star-forming galaxies. There, the magnitude of the change appears to be correlated with the SFR of galaxies, or the strength of UV emission. The largest offset reaches ~ 1 dex in stellar mass and ~ 2 dex in SFR, while the median changes are ~ 0.2 and ~ 0.4 dex, respectively.

The best-fit properties for the quiescent population at these redshifts do not appear to be affected significantly by the change. This indicates two possibilities that: (1) their last stellar populations formed at the same temperature as in the local universe; (2) photometric IMF variations in the quiescent galaxies are below the sensitivity limit of our procedure of $T \sim 20$ K. Nevertheless, the most bottom-light quiescent galaxies are still found in the lowest redshift bins, at $z < 0.8$, which suggests that some internal feedback (stellar radiation or cosmic rays) on top of the CMB may heat the gas at the time of the last star-forming episode to above 25 K at $z > 0.8$. However, it is also likely that some of coldest faint quiescent galaxies at $z > 0.2$ may still be undetected.

It is also worth noting that the photometric fitting method is not capable of recovering IMF shapes with IMF temperature $T < 20$ K, as show in the mock simulations in Sneppen et al. (2022). Therefore, the lower bound found here is characteristic of the method. Although physically this bound coincides with the temperature background in the MW, it disagrees with the probes of even bottom-heavier IMFs in elliptical galaxies and other old stellar structures at low redshift in Conroy & van Dokkum (2012); van Dokkum & Conroy (2012); Geha et al. (2013); Martín-Navarro et al. (2015); Conroy et al. (2017); van Dokkum et al. (2017a); Hallakoun & Maoz (2021).

Star-forming Main Sequence

At every redshift, most of the actively star-forming galaxies of each stellar mass have been found to exhibit a narrow range of SFR, which defines the star-forming main-sequence (SFMS) (Brinchmann et al., 2004; Noeske et al., 2007a; Peng et al., 2010; Speagle et al., 2014). This relationship

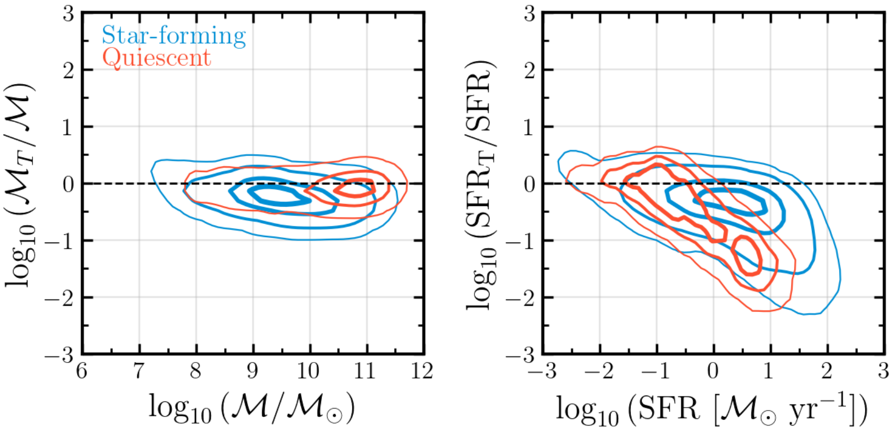

Figure 2.4: Difference in stellar mass and star formation rate between the "best-fit IMF sample" $(\mathcal{M}_T, SFR_T)$ and the standard properties from COSMOS2020 $(\mathcal{M}, SFR)$ at $0 < z < 2$. The properties $(\mathcal{M}_T, SFR_T)$ are taken at the best-fit IMF temperature T, while $(\mathcal{M}, SFR)$ are based on the local IMF, analogous to $T \sim 20$ K. The standard COSMOS2020 properties were converted from Chabrier to Kroupa IMF for a consistent comparison, scaling properties by 1.06 (eg., $\mathcal{M}_\mathcal{K} = 1.06\mathcal{M}_\mathcal{C}$, using the conversion from Zahid et al., 2012). The separation of galaxies into star-forming and quiescent was done in the UVJ color space of the best-fit IMF colors. The UVJ classification is consistent between two catalogs with 98.2% agreement. The contours outline 42,545 active and 8,416 passive galaxies. Clearly, as the best-fit IMF is almost always bottom-lighter than in the Milky Way, the masses and star formation rates shift to lower values. The median differences of the total sample correspond to $log(\mathcal{M}_T/\mathcal{M}) \approx -0.21$ (1/1.6 linear change) and $log(SFR_T/SFR) \approx -0.40$ (1/2.5 linear change). The offset is on average higher for star-forming galaxies with the highest SFR, while quiescent galaxies experience little to no change in stellar mass and a similar change in SFR. The contours in both plots are consistent and extend to the same number levels (outer contours cover 98% of the respective total numbers).

holds in both photometrically and spectroscopically-derived SFR and despite the fact that galaxies have a range of different star formation histories, supernova rates, strengths of active galactic nuclei feedback or cosmic environment. However, it can still be expected that variability in these factors can play role in changing the distribution of stellar masses in a galaxy. Therefore, one of the ways of testing the properties of the variable IMF fits is by verifying that the main sequence still holds.

Figure 2.5 shows all galaxies, where the star-forming ones still form the SFMS at each redshift despite the shift in stellar masses and star formation rates due to changing the Chabrier IMF at 20 K to IMFs at the best-fit temperatures. Similarly, the work of Steinhardt et al. (2022b) that implemented the same temperature-dependent IMF, showed that there is a correlation between SFR, stellar mass at every redshift, consistent with the

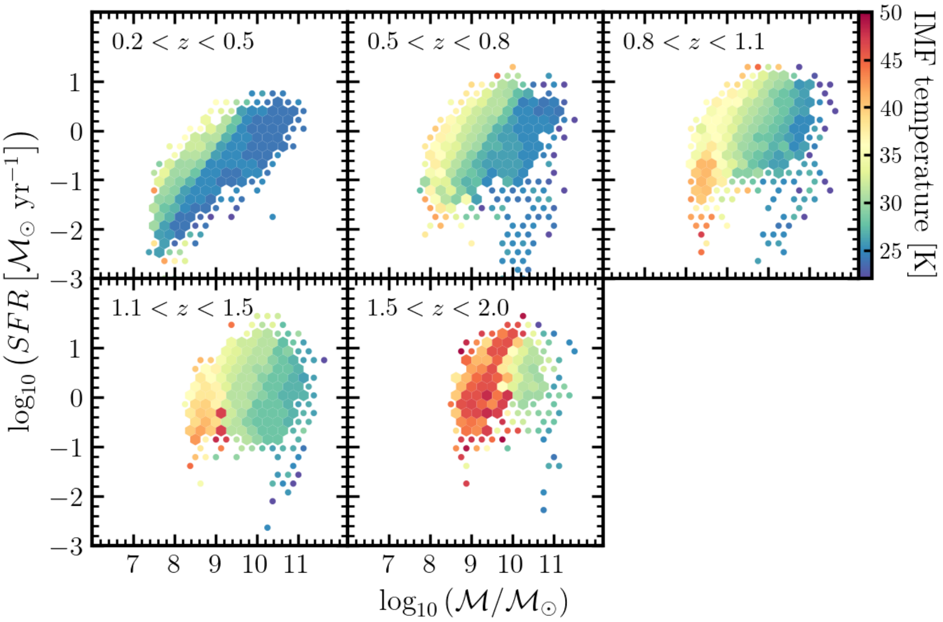

Figure 2.5: All galaxies plotted in the space of the star-forming main sequence in redshift windows from $z = 0.2$ to 2.0. The color corresponds to the median IMF temperature in a bin of stellar mass and SFR ($log(\mathcal{M})$, $log(SFR)$). Bins with ≥ 10 samples are filled, bins with $1 - 9$ samples are shown as scatter. Typical star-forming galaxies are found on the main sequence, showing a gradient of IMF temperatures correlated with the sSFR; quiescent galaxies turn off the sequence and extend to lower SFR at the highest stellar masses and lowest IMF temperatures; objects with the highest IMF temperatures at the low stellar mass end exhibit a distinct temperature relationship from the typical main sequence (the temperature relationship is shown on Figure 2.7).

known relationship. While the SFMS appears to be the same qualitatively, the exact offset and gradient of the relation should be sensitive to the shape of the best-fit IMF and should correlate with it, as suggested by the change of the SFR and stellar mass in Figure 2.4.

The best-fit properties here indicate that there is a gradient of IMFs along the SFMS at every redshift. The IMF temperature increases most rapidly towards the high SFR and low stellar mass end. The gradient becomes steeper at the higher redshift, with more extreme cases of the high-temperature galaxies. As shown in Figure 1 of Steinhardt et al. (2023b), the change of IMF shape may be correlated with the gradient of the temperature of dust continuum emission shown in Magnelli et al. (2014). This suggests that the "IMF temperature" parameter may trace the temperature of molecular clouds at star formation, as argued theoretically (Jermyn et al., 2018). Therefore, with the evidence presented here and in the previous work it may be compelling to model a possible relationship or an equilibrium state between temperature of the molecular clouds and cold dust. If calibrated at low redshift, this relationship can be used to constrain the IMF for galaxies at high redshift for which measuring gas temperatures from line ratios is challenging (see § 2.7 for further discussion).

As expected, the quiescent population is found at the highest mass bins for a given SFR and redshift. The colors in Figure 2.5 indicate that the quiescent galaxies are coolest at the lowest redshift, and gradually become warmer at the higher redshift. This effect demonstrates that either the star-forming gas used to form the last stellar population is hotter in earlier epochs due to some feedback mechanisms or that some of the coolest samples at the higher redshift are below the detection limit of the COSMOS2020 surveys. The last is more likely, as observations show that the average temperature in massive quiescent galaxies at $0.2 < z < 2.0$ is approximately constant at $T_d = 21 \pm 2$ K (Magdis et al., 2021). Finally, the quiescent galaxies are coolest among other galaxies at every epoch. Thus, they appear to turn off the main sequence once some critical mass is built up[5] which appears to be traced by the IMF temperature.

A population of low-mass and hot galaxies appears as indicated by the IMF temperature in the highest redshift panels of the SFMS. These galaxies have distinct combination of sSFR and IMF temperature, as discussed in more detail in § 2.4. Steinhardt et al. (2023b) suggested that they also appear to have compact morphologies. It has been hypothesized that these galaxies may represent the early, core-forming stage of galaxy evolution. If that is the case, this population is only cooling down onto the SFMS and thus can be expected to have a different $SFR - M_\star$ relationship or none, similarly to quiescent galaxies.

It is unclear whether this sample is separate from the typical star-forming galaxies on the main sequence and therefore requires investigation. Previously, it has been argued by Abramson et al. (2014) that the SFMS can be explained solely by the spatially-resolved evolution of the star-forming discs which host evolved bulges. If the fundamental SFMS evolution is driven purely by the physics of star formation, it is possible that the core-forming galaxies form a similarly straight SFMS. On the other hand, if the typical main sequence galaxies are driven by a combination of star formation and disc-morphology effects, the core-forming galaxies may exhibit a characteristically different main sequence: a power law with a different ex-

---

[5] Evidence in § 2.4 from quiescent galaxy fraction appears consistent with there being a characteristic mass for quenching at every redshift, which monotonically decreases towards the current epoch.

ponent, normalization or a different functional form (more details follow on this in § 2.4). Thus, morphology may present hints for the mechanisms driving the SFMS relation and other stages of evolution.

Finally, the galaxy sample covers almost 4 orders of magnitude in SFR with some of the fainter samples detected only in COSMOS2020 and not the previous COSMOS catalogs (Figure 2.5). The low-mass galaxies are cut sharply at the higher redshift due to a combination of the Malmquist bias at the low SFR, the quality cuts here at the higher SFR (see § 2.4) and mass completeness cuts. At the same time, the most massive and luminous galaxies are found in the most distant observations where the sampled cosmic volume is largest.

Stellar Mass Function

Stellar mass function, as the comoving volume density of star-forming and quiescent populations at different redshift snapshots, is an observational tracer of growth of stellar mass at different scales over time (Fontana et al., 2006; Drory & Alvarez, 2008; Marchesini et al., 2009; Peng et al., 2010; Pozzetti et al., 2010; Ilbert et al., 2013; Moustakas et al., 2013; Muzzin et al., 2013; Grazian et al., 2015; Song et al., 2016; Davidzon et al., 2017; Stefanon et al., 2021; Weaver et al., 2023). These observations provide constraints for theoretical models and simulations of galaxy evolution, and eventually help to study the mechanisms regulating galaxy assembly, growth and quenching of star formation. Here, the fraction of quiescent to total galaxies in terms of the mass functions is used to show the growth and the hierarchy of the quenched population.

The fraction of quiescent galaxies as a function of stellar mass obtained with the best-fit IMFs is reproduced with the same overall characteristic behaviour as in most studies that observe the effect of downsizing, reported first in (Cowie et al., 1996; Juneau et al., 2005; Fontanot et al., 2009). The mass scale of quenching on Figure 2.6 indicates that the most massive galaxies are formed at earlier epochs and evolve faster than the less massive populations at lower redshift.

According to the best-fit stellar masses obtained with a bottom-lighter variable IMF (Figure 2.4), the stellar mass function for star-forming galaxies is shifted towards the lower stellar mass with respect to the quiescent which stays unaffected (individual mass functions are shown in Appendix 2.10). Therefore, the passive galaxy population becomes more abundant for the most massive galaxies at every redshift. As a result, the evolution of the

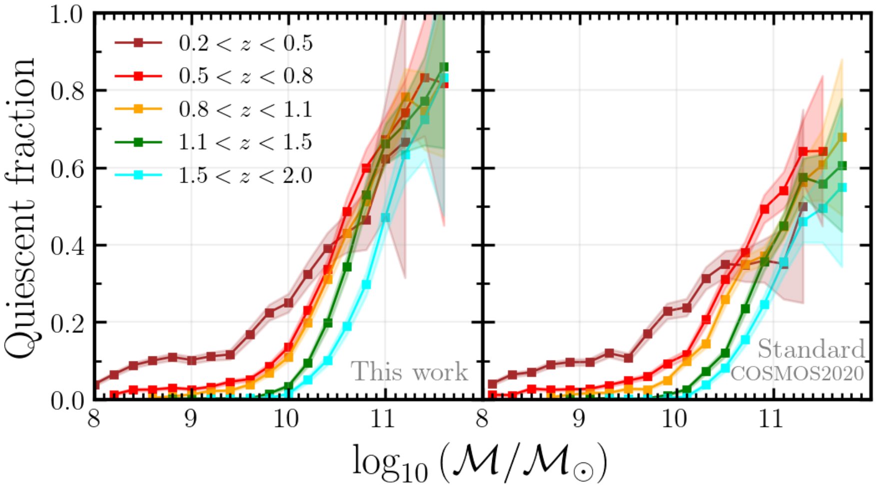

Figure 2.6: The observed fraction of the quiescent galaxies as a function of stellar mass defined as $log(\Psi_{QS}/[\Psi_{SF}+\Psi_{QS}])$ for a stellar masses derived with a best-fit IMF (left) and standard stellar masses form the COSMOS2020 catalog (right). The uncertainties include Poisson error in star-forming and quiescent galaxy counts. Stellar mass $log(\mathcal{M})$ is limited according to completeness levels at different redshift for star-forming and quiescent galaxies (Weaver et al., 2023). At every redshift, most massive galaxies complete their evolution first, and lowest mass galaxies take the longest time to evolve. The evolution from high to low mass end progresses smoothly with redshift. Overall, this picture is consistent with the effect of downsizing. Notably, for the properties with the best-fit IMF this effect appears consistently at all redshift bins – even at $z > 1$ – unlike in some of the previous studies of stellar mass functions (see text for details). These properties (left) show a systematically higher fraction of quiescent galaxies in the most massive tail than inferred from the standard property set (right). This difference comes from the differential change in the stellar mass, where the star-forming functions are shifted towards lower masses, while the quiescent ones mostly remain unchanged (this comparison is shown in Appendix 2.10).

quiescent mass scale is even more sharply consistent with mass downsizing in comparison to standard photometric properties, similarly to results in Steinhardt et al. (2022a).

The change in the quiescent galaxy fraction with redshift allows placing constraints on possible mechanisms of quenching. As shown in Steinhardt et al. (2022a), there appears to be a characteristic mass at every redshift, above which majority of the galaxies have stopped forming stars. This characteristic mass monotonically increases with redshift, consistent with downsizing. This behaviour is consistent with running out of cold molecular gas or some universal feedback mechanism and ability to cool it or, more broadly, with the framework of “mass quenching” (Peng et al., 2010). Some possible quenching mechanisms include morphological quenching, AGN feedback or cosmological starvation (Man & Belli, 2018).

Galaxy Population Diagram

This section shows a relation between the sSFR, or inverse galaxy growth timescale, and the temperature of the star-forming gas derived from the IMF constraints. It appears that main-sequence galaxies experience a decline in the efficiency of converting their gas into stars towards lower redshift from molecular gas studies (Magdis et al., 2021) or, more generally, from abundance matching (Finkelstein et al., 2015b). Similarly, there is a monotonic decrease in sSFR of main-sequence galaxies from photometric properties (Peng et al., 2010; Speagle et al., 2014). As seen from the SFMS in this work (Figure 2.5), the IMF temperature is proportional to sSFR for star-forming galaxies, but the relationship is likely different or breaks completely for quiescent galaxies. Should this behaviour break or change characteristically for any galaxies in our sample, this may signify a different regime of star formation, as argued in Steinhardt et al. (2023b).

Figure 2.7 shows the relationship between sSFR and the IMF temperature in the sample at $0.2 < z < 2.0$. As can be expected, the densest region of the diagram is populated by galaxies on the main sequence. There IMF temperature and sSFR appear to be coupled the strongest for these galaxies, albeit spanning a small range of both properties. Likely, this is consistent with the strong feedback mechanisms driving these galaxies on the SFMS.

The $sSFR - T_{IMF}$ coupling appears to break in two different ways for the extreme tails in temperature and mass, which suggests characteristically distinct galaxy populations. The low temperature end with the most massive objects is represented by the quiescent population. Finally, the population at the high temperature has the shortest growth timescales, lowest masses and thus is likely to be in the state of rapid star formation and cooling onto the "typical" main sequence. Perhaps these properties signify three distinct modes of star formation, connected by galaxy evolution tracks first from early rapid formation, then to the strongly-regulated main sequence and, finally, quiescence. Possible physical processes defining these modes are discussed in more detail in Steinhardt et al. (2023b).

In addition, Steinhardt et al. (2023b) suggest that the thermal evolution on and off the star-forming main sequence may be independently linked to the apparent morphological development of galaxies. The connection shows that the cooling off the main sequence galaxies is possibly associated with the transition from disc-like structures with a central bulge or a core to a more extended elliptical structure. The evolution is also apparent in the change of photometric colors, from predominantly blue discs with red cores to red ellipticals. Finally, the new, early stage of evolution appears to have blue compact cores as their morphological counterparts at all redshifts, which could be progenitors of the future disc-like galaxies with a predominatly quiescent core, similarly to the morphologically-driven evolution in Abramson et al. (2014).

Notably, $sSFR = 10^{-8}$ yr^{-1} is a common upper limit set by star formation rate in SED templates in different fitting codes. Greater sSFR are not allowed to avoid degeneracy between the star formation history and dust in solutions. Therefore, the real gradient at the high temperature tail may be steeper than observed here. The true slope is going to constrain the potential physical mechanism driving the evolution of this galaxy population.

On the other end, the quiescent population appears to be limited from the bottom at around $T_{IMF} \approx 20K$, which is either real or limited by the sensitivity of the photometric procedure to the weak UV signal. The 20 K limit is in agreement with the local molecular gas measurements in the Milky Way (Schnee et al., 2008). The Galaxy is likely on the way down in the quiescent branch at low temperature and at $sSFR \sim 10^{-11}$ yr^{-1} (Licquia & Newman, 2015) on Figure 2.7. Therefore, this suggests that the sharp cut at the low temperature and at least down to the MW sSFR is real. Nevertheless, the technique employed here cannot recover temperatures lower than $20-25$ K, as shown using mock galaxies in Sneppen et al. (2022). Therefore, the method here is not capable of recovering those IMF that have bottom-heavier shapes than in the MW, as reported for stellar systems with old stars in Conroy & van Dokkum (2012); van Dokkum & Conroy (2012); Geha et al. (2013); Martín-Navarro et al. (2015); Conroy et al. (2017); van Dokkum et al. (2017a); Hallakoun & Maoz (2021).

2.5 Interpretation as a Morphological Sequence

> This section is included in the Chapter during the writing of the thesis. It shows relevant results of morphological analysis of the `COSMOS` galaxies from Steinhardt et al. (2023b). It includes Section 4.1 “Core-forming Galaxies and Blue Nuggets” and Figures 3, 4 (with minor changes) from that publication, which were composed by the author of the thesis.

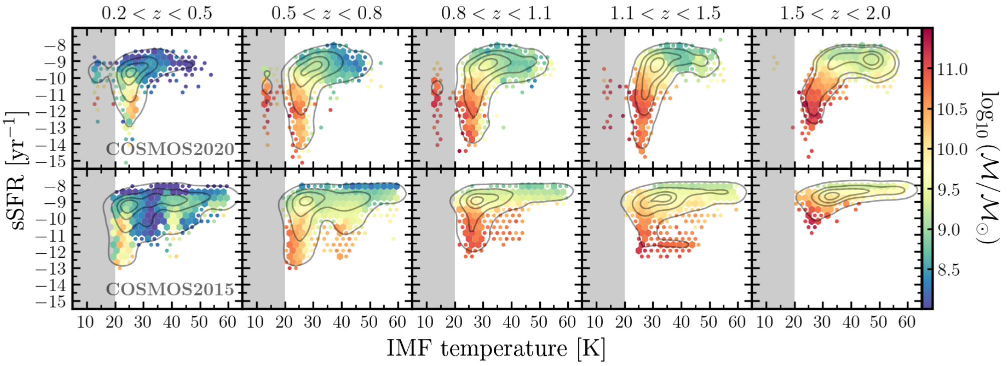

Figure 2.7: Diagram of sSFR as a function of IMF temperature T_{IMF} for several redshift windows in the COSMOS2020 (top row; provided here) and COSMOS2015 surveys (bottom; from Sneppen et al., 2022). The bins are colored by median stellar mass $log(\mathcal{M})$. The black contours show the sample density for reference. Bins with ≥ 10 samples are filled, while the bins with $1-9$ samples are shown as scatter. The gray-shaded area shows the range where the temperatures cannot be recovered. The densest regions are populated with the typical main-sequence galaxies, which appear to be driven by the coupling of sSFR and IMF temperature. The two tails with characteristically different $sSFR - T_{IMF}$ relationships from the typical main sequence appear to be quiescent (low T_{IMF}) and active (high T_{IMF}). These distinct galaxy regions show a smooth gradient of stellar mass, which together with the declining sSFR and T_{IMF} suggests a clear evolutionary sequence. The sample shown at the top excludes outliers resulting from spurious SED fits (see Appendix 2.9). According to the synthetic tests performed in Sneppen et al. (2022), the best-fit IMF properties cannot be trusted at $T_{IMF} \lesssim 20$ K. Therefore, sub-samples at $T_{IMF} \approx 10-20$ K that are present in most panels here cannot be trusted.

It is found here that the morphological properties of galaxies complement the galaxy-wide physical properties from SED fitting. For example, visual inspection of the images of the brightest candidates (in F814W and F160W HST ACS/WFC3 bands[6]) selected from each of the three groups on the $sSFR - T_{IMF}$ diagram at the same redshift shows distinct morphological and colour properties (Figure 2.8). The most top-heavy IMF and high-sSFR objects (top panel) have smaller spatial extent, irregular or disc-like shape and are predominantly blue. On the other end, the quiescent sample (bottom panel) has distinct elliptical morphology, large sizes and red colours. The typical MS galaxies appear to be in between with a range of morphologies, some of which have developed structure with spiral arms and bulges, and a red-blue colour gradient at increasing radius.

A more detailed analysis is shown in Figure 2.9. The images of galaxies are modelled with a single-component Sérsic profile in the F814W band,

---

[6] Observations are preformed and reduced as part of the COSMOS HST Treasury project

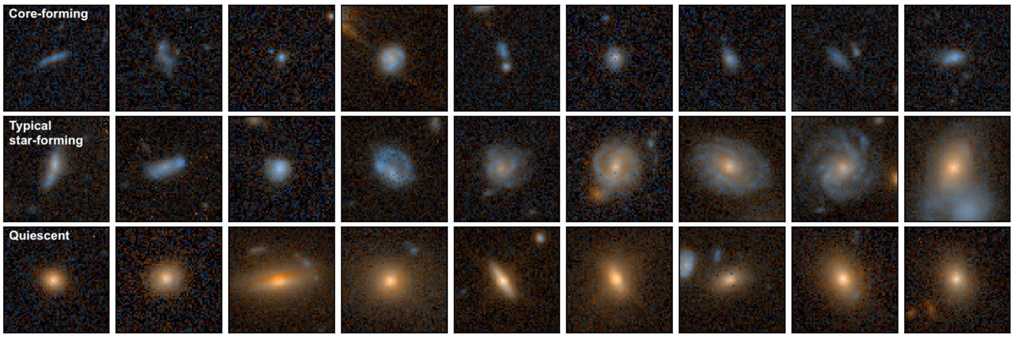

Figure 2.8: *Hubble* observations in the F814W (ACS) and F160W (WFC3) filters for core-forming (top), typical star-forming (middle), and quiescent (bottom) galaxies randomly selected from the highest S/N objects from the COSMOS2015 survey at $z \sim 0.8$.

which is then used to colour the $sSFR - T_{IMF}$ diagram by Sérsic indices n and radii containing 80, 50 and 20% of model flux (R_{80}, R_{50}, R_{20}). Based on this information, several behaviours are apparent from the figure: (1) most high-sSFR systems are dominated by an irregular or a disc+bulge structure ($n \sim 1$), while the quiescent ones have a compact luminous bulge ($n \sim 4$); (2) R_{80} and R_{50} show that the high-$T_{\rm IMF}$ objects have the smallest overall profiles, in contrast to large elliptical galaxies. The correlation of morphological profiles with the physical properties at $z \sim 0.8$ suggests that the $sSFR - T_{IMF}$ diagram represents an evolutionary sequence.

The core-forming galaxies bear strong resemblance to a population dubbed "blue nuggets"[7] most frequently found at $1 < z < 2$ (Huertas-Company et al., 2018; Lapiner et al., 2023). They have similarly high sSFR, which places them at the top of the star-forming main sequence, small stellar masses, young stars, little dust obscuration and compact morphologies, as seen in data (Cardamone et al., 2009; Huertas-Company et al., 2018) and simulations (Zolotov et al., 2015; Tacchella et al., 2016b,a; Lapiner et al., 2023). The increased abundance of core-forming galaxies towards $1 < z < 2$ also supports this comparison. The best-fit Sérsic indices of the core-forming galaxies indicate that they are predominantly smaller versions of the typical star-forming galaxies, consistent with a disc-like or irregular structure with the index of $n \sim 1$ (Fig. 2.9), and have concentration ($C = 5 \log{(R_{80}/R_{20})}$, Bershady et al., 2000) comparable or

---

[7] It is likely to be mixed with another group of galaxies called "green peas" at $0.1 < z < 0.4$ (Cardamone et al., 2009). Their physical properties appear to be the same, but their identification as distinct galaxies is based on their strong nebular emission observed in the SDSS r-band.

slightly higher than the typical main-sequence galaxies.

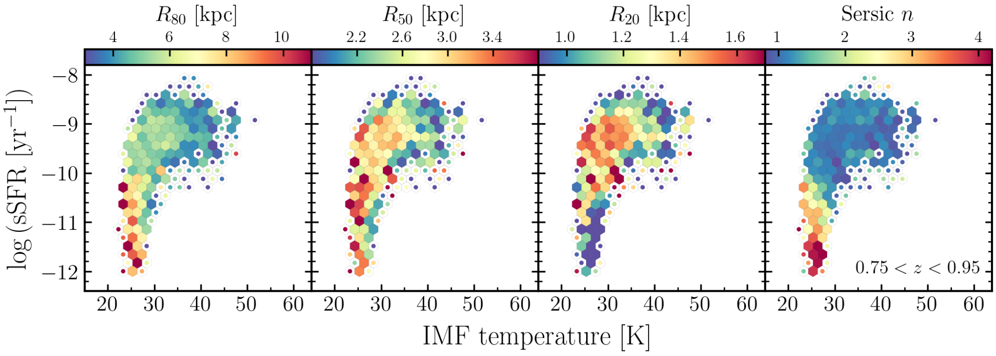

Figure 2.9: Density plots showing the best-fit Sérsic profile properties made with *Hubble* WFC3 observations in the F814W filter for galaxies at $0.8 < z < 0.9$ (i.e. $\sim 0.44\ \mu$m in the rest-frame). The panels show median quantities in each $T_{\rm SF}$-sSFR bin (left to right): the best-fit Sérsic index; the calculated aperture radius containing 20% of light, R_{20}, using definitions from Miller et al. (2019); the best-fit effective radius, R_{50}; and the calculated aperture radius containing 80% of light, R_{80}. Bins with fewer than 5 data points are shown as dots.

2.6 Evolutionary Interpretation

> This section is included in the Chapter during the writing of the thesis. It shows relevant results of morphological analysis of the `COSMOS` galaxies from Steinhardt et al. (2023b). It includes Figure 2 from that publication, which was produced by the author of the thesis.

The $sSFR - T_{IMF}$ diagram (Fig. 2.7) can be assigned an evolutionary interpretation. As it separates not only active and passive populations but also differentiates between different star-forming galaxies, it may be possible to track the change of physical properties associated with the location in this property space. Indeed, Figure 2.10 shows that the most top-heavy IMF objects are more commonly found at higher redshift, in contrast to the passive population. They also appear to be in the low-value tail of the stellar mass and age distributions, as well as have distinct overall size, morphology and (apparent from images) bluer colours. Overall, it appears that the smooth change in these properties (age, mass, redshift) is correlated with the IMF and sSFR, as shown by the black arrows. Therefore, it suggests that the changes along the black arrows indicate an evolutionary sequence.

One possible cause for the young galaxy population to have a top-heavy IMF can be high volume density of the gas that allows for cooling times that are shorter than the time required to develop stellar feedback from massive stars, as suggested by Dekel et al. (2023) for high-redshift galaxies with large luminosity. However, it is unclear if such conditions could be met, as based on the Sérsic profiles, these galaxies do not appear to have high stellar mass surface density, as for example starburst galaxies in Barro et al. (2017).

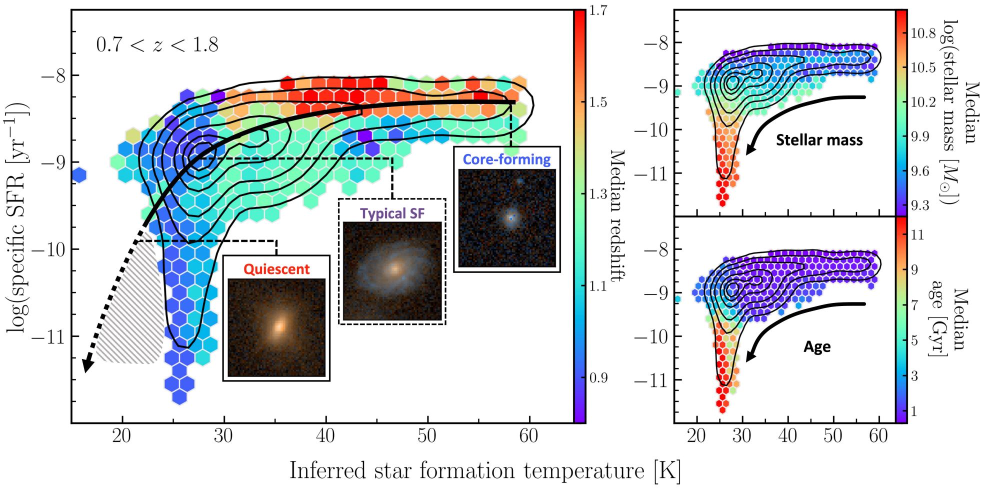

Figure 2.10: The $sSFR - T_{IMF}$ diagram for COSMOS2015 galaxies at $0.7 < z < 1.8$ showing bins with at least 10 data points. Panels are coloured by the median (left) redshift; (top-right) stellar mass; and (bottom-right) age of the stellar population. Moving from top-right to bottom left, galaxies become more massive, with older stellar populations, and are more commonly observed at later times. Although no morphological information was used to produce the diagram, this is also a morphological sequence (see also Figure 2.8). The dashed region in the left panel indicates that the IMF cannot be recovered at $T_{\mathrm{SF}} \lesssim 25$ K (Sneppen et al., 2022).

2.7 Discussion

The analysis here shows that the new properties show a clear picture of mass-dependent assembly of galaxies in terms of the stellar mass functions and provide new valuable insights into the star-forming processes along and "around" the star-forming main sequence. It is shown that the gas temperature derived from the best-fit IMF adds a new dimension to investigate efficiency of star formation and possibly dissect galaxy evolution into different stages. This is supported by the recent work that finds a connection between IMF-selected galaxies and their morphologies (Steinhardt et al., 2023b) and suggests a possible interpretation in which galaxies evolve from blue compact cores, through disc formation around the evolved core to elliptical extended structures.

This section emphasises a possible bias introduced by assuming a universal IMF based on the Milky Way, as well as the recently published issues with even averaging observations of different parts of individual galaxies. It finally discusses implications for the problem of the "impossibly early galaxies", which becomes relevant here by assuming that the observed increase in the temperature of the various parts of the ISM continues to high redshift, so that the bias in the estimated mass of the stellar populations becomes increasingly large.

The Milky Way Bias

Resolved observations in the local universe uncover the chemical and structural complexity of galaxies that translates into variations in their star formation processes (Hodge, 1989; Gallart et al., 1996b). It has been found that the cold ISM exists in a range of phases that are sensitive to the internal processes as well as the environment (Saintonge & Catinella, 2022). The latter review shows that there are systematic variations in the amount of molecular gas and the rate at which it is converted into stars across individual galaxy populations. These differences in the cold phase of the ISM are expected to produce different stellar populations resulting in different feedback, which can build up to produce strong differences in stellar masses, metallicities and other quantities over time. As a result, it is easy to introduce systematic bias in inferred astrophysics by making strong assumptions that neglect these differences.

Historically, the complexity in star-forming conditions has been dealt with by assuming that the IMF derived in the MW is universal (eg., Kroupa, 2001; Franceschini et al., 2006; Arnouts et al., 2013), although some hints of IMF variability have become available (Treu et al., 2010; Martín-Navarro et al., 2015; van Dokkum et al., 2017b). However, galaxy evolution over cosmic time has been shown to break even under different IMF measurements made only in the Milky Way (Speagle et al., 2014).

Evidence from cold dust continuum emission and atomic gas measurements (Valentino et al., 2020) suggests that molecular gas temperatures at high redshift are unlikely to be the same as in the local universe. The dust temperature from stacked measurements increases from 20 K at $z = 0$, equivalent of the MW gas temperature, to 40 K at $z = 2.3$ (Magnelli et al., 2014) and to 50 K at $z = 4$ (Schreiber et al., 2018; Cortzen et al., 2020). This is consistent with the evidence of increasing intensity of the radiation field (Béthermin et al., 2015; Magdis et al., 2017) in earlier galaxies. Based on theoretical work, temperature changes in the star-forming gas should be sensitive for the mass scale of the stellar population (Jeans, 1902; Low & Lynden-Bell, 1976; Larson, 1998, 2005) and modify the shape of the IMF (Jermyn et al., 2018).

Therefore, it is necessary to relax the assumption of the local IMF at least for non-local galaxies to reflect the expected changes in the star-forming conditions. Previous studies of Hα equivalent width (Gunawardhana et al., 2011; Nanayakkara et al., 2017; and references therein) indicated that galaxies at $z \sim 0.35$ and $z \sim 2$ have flatter high-mass IMF slopes, which likely evolve with redshift. Besides, Zhang et al. (2018) find a more direct indication of a top-heavy IMF in starburst galaxies at $2 < z < 3$ from ^{13}C/^{18}O lines. Based on the photometric constraints obtained in this work and previously in Sneppen et al. (2022), the IMF at $0 < z < 2$ is systematically different in star-forming galaxies and is likely to change as the CMB temperature increases at higher redshift and due to a complex interplay of various feedback processes. Consequently, the stellar masses of typical star-forming galaxies appear overestimated by up to 1.0 dex in the most extreme cases (Figure 2.4). As a result, the interpretation of such key processes in galaxy evolution as quenching becomes more pronounced - it is more consistent with the effect of downsizing (see § 2.4). In addition, the IMF-derived temperature of star-forming gas hints at an early and hot stage of galaxy evolution (Steinhardt et al., 2023b), as well as provides insights into the star-forming main sequence (see § 2.4).

When it is not possible to constrain an IMF, which is the case for most current observations outside the COSMOS field, it is instead necessary to assert a physically motivated IMF, because using the 20 K local IMF can break the inferred galaxy properties in the different ways addressed in this work in § 2.4–2.4. The assumption should be based on the CMB temperature at the relevant redshift regime[8] and the latest understanding of the ISM temperature. While there is no complete theory of the feedback-driven gas temperature in galaxies, it is possible that the temperature measurements of dust continuum or [C I] gas line ratio in specific galaxies or galaxy

---

[8] It is worth noting that the IMF-derived temperature theoretically corresponds to the temperature in the star-forming clouds of the photometrically-constrained stellar population. Thus, for the quiescent population this temperature is offset from the observation by the time when the last stellar population formed.

populations can be used as a proxy (more on this strategy in § 2.7).

Finally, the observations of galaxy populations throughout the cosmic time suggest that even if there is a most-likely universal IMF, it likely does not look like the MW IMF. The most typical observed galaxy at the currently sampled redshifts is on the star-forming main sequence. However, our Galaxy with $sSFR \sim 10^{-11}$ yr^{-1} (Licquia & Newman, 2015) is consistent with being quiescent. Besides, the existing empirical IMFs probe only small selected regions in the MW, which are not guaranteed to represent the average conditions in the Galaxy. Thus, if it is possible to fix an IMF in a random photometric-template fitting experiment, the local IMF is unlikely to be the preferred option.

Monolithic Galaxy Bias

Assuming that the diversity of gas temperatures and compositions can be solved for, the other key approximation is that of galaxies as point sources. The structural extent and large crowding of stars is neglected in spatially unresolved studies. So it is possible that the integrated light can be biased towards the brightest stars. In this case, the old stellar populations may be outshined by luminous young O and B-type stars in star-forming galaxies. Besides, galaxies can have different morphology, from compact cores to complex spiral arms with bars and ellipticals, where, depending on relative locations of different stellar populations, each probably results in a different bias.

Recent studies comparing spatially-resolved and integrated photometric observations discover relative bias in recovered stellar populations. Giménez-Arteaga et al. (2023) show that for five compact early galaxies at $5 < z < 9$ this leads to their masses being underestimated by a factor of up to 1.0 dex. It is found that the young stars born in the central compact region dominate the integrated photometry over the older stars. Sorba & Sawicki (2015, 2018) showed similar results, with up to 80% of the spatially-resolved stellar mass missing from their integrated analysis at $0.25 < z < 2.50$.

As most extragalactic observations lack spatial resolution, it is key to quantify the reported bias and factor it into physical properties of galaxy ensembles. This effect is likely to be the strongest for the most actively star-forming galaxies with blue colors and especially young starbursts. It is also likely that it is easier to “conceal” the stellar mass in the more compact structures. Therefore, it is necessary to investigate this effect for dusty star-forming galaxies, galaxies with different sSFR and various morphologies at different epochs. The empirical correction for stellar mass has been derived by Sorba & Sawicki (2018) for galaxies at $0.25 < z < 2.50$ based on the sSFR. The work reported the strongest bias at increasing redshift and high sSFR, but has not investigated the connection to galaxy morphology.

The effect of the combination of the temperature-dependent or else physically-motivated IMF with the integrated photometry bias will perhaps depend on the bottom-lightness of the IMF and the total galaxy luminosity at which the photometry is dominated by the youngest O and B-type stars. Calculating the total systematic effect is necessary to properly compare the observed physical properties of galaxies with the cosmological predictions.

Finally, the photometric decomposition of main-sequence galaxies into discs and buldges or central cores in Abramson et al. (2014) demonstrates that morphological properties of galaxies may be used to further dissect galaxy evolution into its fundamental constituents. It was shown that the SFMS may be reconstructed with the star-forming galaxy discs alone. Such interpretation would be consistent with the picture of galaxy evolution here and in Steinhardt et al. (2023b), where the core-forming galaxies may be progenitors of the main sequence discs (see § 2.4).

Temperature Proxies for IMF

In this work it was possible to constrain the IMF only for the $\sim 10\%$ of COSMOS2020 catalog with the widest wavelength coverage and highest S/N, leaving most of the observations unused. The unused part of the sample demonstrated strong covariances between IMF and other model parameters. Therefore, additional information in terms of extending the wavelength coverage, probing deeper photometry or setting a prior IMF is required to make use of the available data.

In the framework of finding best-fit model photometry it is common to impose a magnitude-based prior to zoom in on a physically motivated part of the parameter space, which would otherwise suffer from statistical degeneracies (Brammer et al., 2008). Similar approach is commonly performed with the IMF when the MW prior is used. If there are indications that the ISM changes at higher redshift can drive the changes in mass scale of stellar populations, a prior on the IMF should be set correspondingly to the relevant physical regime.

For setting the IMF, it is necessary to determine the gas temperature in the relevant redshift regime. It is thought that multiple feedback processes may be responsible for setting the temperature of the star-forming gas in the galaxy (Papadopoulos, 2010). However, currently there is no preferred method for predicting this temperature in a galaxy. Therefore, it is only possible to determine the minimum CMB temperature with certainty. As it is demonstrated in Steinhardt et al. (2023a), the starting point can be setting the IMF based on the redshift regime, which corresponds to an approximate CMB temperature band. Although not ideal, this method should almost certainly be more accurate than the assumption of the local IMF.

In absence of theoretical models for determining the gas temperatures at redshift $z > 2$, it may be possible to use the temperature of the cold dust component as a proxy. The possible correlation between excitation temperature of the gas and cool dust in galaxies on the main sequence (Valentino et al., 2020) may be used as prior temperature for IMF. Thus, at redshifts $2 < z < 6$ where the CMB is below the local MW temperature, such proxy for an IMF could be tested for galaxies on the main sequence. However, as discussed in § 2.4, different feedback processes are likely responsible for galaxies not on the main sequence, such as the starbursts or quiescent galaxies. Therefore, it is not guaranteed that the same temperature correlations can be expected in those galaxies.

A clear example when it is necessary to use prior temperature knowledge are early galaxies found with the James Webb Space Telescope. Their redshift regime ($z > 10$) corresponds to the most extreme star-forming conditions compared to the nearby galaxies, where even the CMB temperature places the lower temperature limit to over 30 K. Therefore, the local IMF assumption (equivalent to 20 K) is physically implausible in these galaxies. However, it is likely not possible to constrain the IMF due to insufficient photometric band coverage in the early observations. Therefore, it is necessary to ensure that the IMF shape meets the minimum temperature requirement set by the CMB. Alternatively, the masses can be overestimated by as much as $0.4 - 1.0$ dex (Steinhardt et al., 2023a).

Impossibly Early Galaxies

In the previous decade, it became possible to test the predictions of the hierarchical assembly of the early galaxies with the advent of such surveys as Cosmic Assembly Near-infrared Deep Extragalactic Legacy Survey (CANDELS; Grogin et al., 2011; Koekemoer et al., 2011) and Spitzer Large Area Survey with Hyper-Suprime-Cam (SPLASH) that allowed observations of sizeable samples of galaxies at $4 < z < 8$. Davidzon et al. (2017) and

Steinhardt et al. (2016), among others, reported a sharp problem where the observed stellar mass growth is more efficient than allowed in the current cosmological model at high redshift. It was found that by converting the photometrically-derived stellar masses to halo masses based on local measurements or by matching galaxies luminosities to the available dark matter halos, the inferred halo masses exceeded the theoretical predictions by as much as ~ 0.8 dex at $z = 10$ (Steinhardt et al., 2016). Similarly, the stellar mass functions appeared to outgrow the halo masses at $z > 3.5$ (Davidzon et al., 2017).

More recently, the disagreement between theory and observations has been extended even to higher redshift of $z > 8$ with some early JWST observations (eg., Labbé et al., 2023). It has been shown that these massive galaxies have outgrown their dark matter halos several times (Boylan-Kolchin, 2023) making it critical that either the Lambda Cold Dark Matter model (Planck Collaboration et al., 2020) is incorrect or the interpretation of observations has a fault. Further studies have either not found the same disagreement (Adams et al., 2023b; McCaffrey et al., 2023) or have resolved it by reducing its statistical significance (Chen et al., 2023) and by using a top-heavier IMF (Harikane et al., 2023; Yung et al., 2023).

It is possible that the increasing disagreement at higher redshift is propagated by the assumptions of the physics of star formation at low redshift. In this case, possibly the analysis of stellar populations at increasingly higher redshift in Davidzon et al. (2017); Labbé et al. (2023) and other work shows a progressively greater bias due to the bottom-heavy IMF. As it is argued in § 2.7, the conditions for star formation are expected to become increasingly different from the local universe in the regimes of higher CMB temperature and correspondingly higher stellar radiation and cosmic ray feedback at high redshift. If that is the case, the mass of the stellar populations in the early galaxies has been overestimated.

Although it is not yet possible to constrain an IMF at high redshift due to the lack of wide photometric information or a large ensemble of rest-frame UV and optical galaxy spectra, this work attempts to demonstrate the effect at lower redshift regime where the survey data are more abundant. It is found that stellar masses even in this already cosmologically "cold" regime at $0 < z < 2$ decrease by up to 0.6 dex with the best-fit IMF, with similar results shown in Sneppen et al. (2022) in COSMOS2015 galaxies.

With the constraints demonstrated at low redshift, it has been possible to make rough predictions of the IMF at much higher redshift regimes which can place the interpreted stellar masses of galaxies back in agreement with the cosmological predictions. Steinhardt et al. (2023a) showed that by assuming that the temperature of the star-forming gas and respective IMF is set only by the CMB, the stellar mass estimates at $z > 8$ can be placed well within the cosmologically allowed regime. Although at $z \sim 10$ the CMB temperature (~ 30 K) becomes substantially higher than in the Milky Way (~ 20 K), it is likely that the various feedback processes associated with the star formation and supernovae can set this temperature even higher leading to much lower estimates of the total stellar masses.

Finally, several assumptions have been made commonly to produce estimates of total galaxy masses at all redshifts, including the local IMF, the specific stellar baryon fraction from abundance matching and the stellar to halo mass fraction. It is argued here that the first assumption is one of the most counter-intuitive based on the expected temperature changes in the early galaxies. If the change in estimated stellar masses from lower redshift IMF constraints is extrapolated to higher redshift, it can be sufficient to reconcile tension with the theoretical predictions of halo masses. However, the fate of the stellar mass crisis will only be clearer after also incorporating the bias from spatially non-resolved stellar populations (Giménez-Arteaga et al., 2023). Among other assumptions, the stellar-to-halo mass conversion is also tied to the local measurements which do not have to hold at high redshifts and thus also have to be tested.

2.8 Conclusion

In summary, this work presents new physical properties of $\sim 10^5$ well-measured COSMOS2020 galaxies at $0 < z < 2$ for which it is most likely to constrain an IMF (Sneppen et al., 2022). It is found that the galaxies are best fitted with a continuum of IMFs. Most of these IMFs are bottom-lighter than measured in the Milky Way. As a result, stellar mass and star formation rate estimates change significantly. The decrease in $M_\star$ and SFR of stellar populations is indicative of the increasing gas temperature in molecular clouds at higher redshift, by construction of the IMF employed here. Consequently, this work also derives the IMF parameter as a measure of the IMF shape and the gas temperature, in theory. Below is a list of the main features and some of the most interesting general implications of this catalog to galaxy evolution identified so far.

- *Change in SFR and $M_\star$ properties.* From the perspective of the temperature-dependent IMF, stellar masses and star formation rates of star-forming galaxies reported in the standard COSMOS2020 catalog up to $z < 2$ are overestimated by factors of $\sim 1.6 - 3.5$ and $2.5 - 70.0$, respectively.

- *IMF shape as a probe of gas temperature.* The changes in physical properties correspond to the overall increase in the temperature of a star-forming gas as a function of redshift inferred form the IMF. The theoretical interpretation of the IMF shape as the gas temperature probe agrees with the evidence of increasing dust and gas temperature with redshift (Valentino et al., 2020; Magdis et al., 2017; Magnelli et al., 2014). The properties of quiescent galaxies exhibit only a small change towards $z \sim 2$, which is consistent with the measurements of dust temperature for quiescent galaxies in Magdis et al. (2021).

- *Sharp downsizing effect.* The fraction of quiescent galaxies as a function of stellar mass appears to be consistent with the effect of downsizing (Juneau et al., 2005; Cowie et al., 1996). The change in stellar masses with the best-fit IMF is differential, such that the star-forming stellar mass functions are shifted towards the lower stellar mass, while the masses of the quiescent galaxies mostly remain unchanged. As a result, there is a larger fraction of high-stellar mass passive galaxies at every studied redshift, which is more sharply consistent with the effect of mass downsizing in comparison with the standard set of properties.

- *The* $SFR - M_\star - T_{IMF}$ *relation.* The best-fit IMF parameter provides new insights about gas temperature on the SFMS and around it. There is a clear positive gradient of IMF temperatures with sSFR on the main sequence. In turn, quiescent galaxies have the lowest temperature at all redshifts. Additionally, the galaxies with the highest temperatures and lowest stellar masses appear to have a relationship with the IMF temperature distinct from that of the typical star-forming galaxies.

- *The* $sSFR - T_{IMF}$ *relation.* Main-sequence galaxies exhibit a strong $sSFR - T_{IMF}$ coupling. However, there appear to be two groups of galaxies for which this relation breaks. The first tail at low temperature corresponds to quiescent galaxies, while the tail at the high temperature is populated with the lowest-mass active galaxies. Based on the likely compact morphologies (Steinhardt et al., 2023b), it has been proposed that the last group is in the early phase of galactic evolution that is distinct from typical galaxies on the SFMS.

This work releases the new catalog and the photometric templates used here for public access.

2.9 Appendix A. Quality cuts & outliers

The best-fit SED templates of some samples converged around several very specific parts of the parameter space. They appear in a grid-like pattern shown in Figure 2.11 as a vertical stripe at the temperature $47 - 48$ K and a horizontal stripe at $-12.5 < sSFR < -11.5$ yr^{-1}. In addition, most objects at 18-20 K were part of the outliers as spurious fits with narrow chi-square solutions. Most of these fits appeared to have the IMF constraint degenerate with the star formation history. In comparison, the sample of COSMOS2015 objects with variable IMF had a smaller number of apparently similar outliers, although in a different part of the parameter space (cf. Steinhardt et al., 2022a).

These samples were removed from the results demonstrated in this work using the following selection criteria. They appeared to have distinct mass-to-light ratios M/L_V for their specific star formation rates $SFR/M_\star$, as well as unusually narrow width of the chi-squared solutions σ_T. Thus, the following criteria were used to cut the solutions corresponding to: horizontal outliers with $log_{10}(SFR/M_\star) < -11.5$ & $M/L_V < 0.9$ $M_\odot/L_\odot$; vertical outliers with $46 < T_{IMF} < 49$ & $M/L_V > 0.3$. These criteria were not optimal, as some viable solutions were cut as a result and some outliers remained in the sample.

Given that this catalog cuts the original data after several selections, and identifies outliers in the best-fit results, it is important to cross-check the data consistency at every stage. Figure 2.12 shows the distributions of K_S magnitude after each of the following selections (the sizes of the data sets are given in brackets):

- *Cut 1 (418,000)*: "ultradeep" stripes of the UltraVISTA photometry. Removing the sources that were biased by the bright neighbors, appeared at the image boundaries, were saturated or failed at execution, as flagged by `SExtractor`. The selection reduced the survey area from ~ 3.4 to 0.9 deg^2.

- *Cut 2 (243,774)*: valid IMF solutions, as defined by chi-squared values in the sampled temperature range $10 < T < 60$ K.

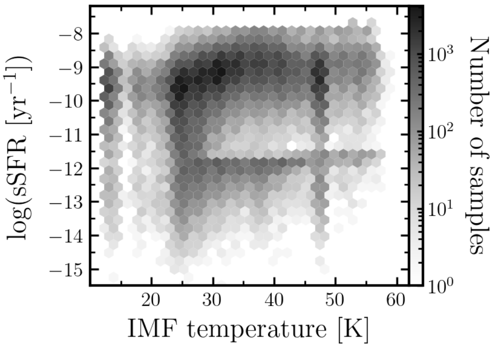

Figure 2.11: Diagram of sSFR as a function of temperature for galaxies at $0.2 < z < 2.0$. The grid-like pattern with the vertical stripe at the temperature $47 - 48$ K and the horizontal stripe at $-12.5 < sSFR < -11.5$ yr^{-1} was flagged as outliers. They likely originate due to the highest-mass IMF break being covariant with the star formation history.

- *Cut 3 (189,332)*: removing solutions flagged as "outlier" (appeared as a grid in Figure 2.11), based on the mass-to-light ratio cuts described above.
- *(Optional) Cut 4 (73,573)*: this sample includes only the solutions where the uncertainty could be estimated based on the chi-squared metric using the minimum variance bound estimator. This sample was used to demonstrate most results in this work and is optional. The histograms in Figure 2.12 show that this cut removes a fraction of faint sources.

The histograms of the K_S magnitude do not differ significantly and thus indicate that there are no major biases introduced by the selections made in the data. However, the last cut is not advised, as it appears to remove a fraction of K_S-faint source.

2.10 Appendix B. Changes in Stellar Mass Functions

This appendix shows the differences between the stellar mas functions of active and passive galaxies computed using the standard stellar masses from COSMOS2020 and the masses from the value-added catalog with the best-fit IMFs. These functions are plotted in Figure 2.13 for star-forming (top row) and quiescent (bottom row) galaxies separately.

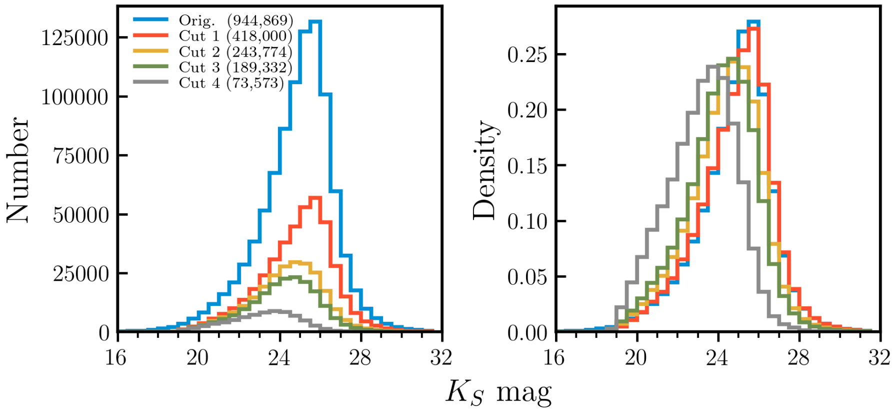

Figure 2.12: Distributions showing K_S magnitude number histogram (left) and density (right) of the data set after each selection or quality cut. The sizes of the data set are indicated in the brackets. The magnitude observable is used to cross-check that the selections do not introduce significant bias in the data.

2.11 Appendix C. Catalog Table

This appendix contains Table 2.3 that demonstrates contents of the value-added catalog that is produced as a result of this work.

Table 2.3: Description of the column labels in the value-added catalog. Rows 1-3: ID and the sky coordinates are taken from the COSMOS2020 `CLASSIC` catalog. Rows 4-55: standard `EAZY`-generated best-fit output. Rows 56-59: best-fit IMF temperature (i.e., bottom-lightness of the Kroupa IMF) with its uncertainties and outlier flags.

Num	Label	Unit	Description
1	ID	—	COSMOS2020 `CLASSIC` catalogue ID
2	ALPHA_J2000	deg	Right ascension (J2000)
3	DELTA_J2000	deg	Declination (J2000)
4	z_phot	—	`EAZY` maximum likelihood photo-z
5	z_phot_chi2	—	chi-squared at z_phot
6	z_phot_risk	—	risk parameter (Tanaka et al., 2018) at z_phot
7	z_min_risk	—	z_phot where risk parameter z_phot_risk is minimised
8	min_risk	—	risk at z_min_risk
9	z_raw_chi2	—	photo-z where z_phot_chi2 is minimised, without priors
10	raw_chi2	—	chi-squared at z_raw_chi2
11	z$_{xxx}$*	—	percentiles of photo-z
12	nusefilt	—	number of filters used for photo-z
13	lc_min	0.1nm	minimum effective wavelength of valid filters
14	lc_max	0.1nm	maximum effective wavelength of valid filters
15	restU	μJy	rest-frame U-band flux density
16	restU_err	μJy	rest-frame U-band flux density uncertainty
17	restB	μJy	rest-frame B-band flux density
18	restB_err	μJy	rest-frame B-band flux density uncertainty
19	restV	μJy	rest-frame V-band flux density
20	restV_err	μJy	rest-frame V-band flux density uncertainty
21	restJ	μJy	rest-frame J-band flux density
22	restJ_err	μJy	rest-frame J-band flux density uncertainty
23	dL	[Mpc]	$\log_{10}$ luminosity distance at z_phot
24	mass	$[M_\odot]$	$\log_{10} M_{star}$
25	sfr	$[M_\odot\ \mathrm{yr}^{-1}]$	$\log_{10} SFR$
26	ssfr	$[\mathrm{yr}^{-1}]$	$\log_{10}$ sSFR
27	Lv	$[L_\odot]$	$\log_{10} L$ (V-band)
28	LIR	$[L_\odot]$	$\log_{10} L$ (8-1000 μm)
29	energy_abs	$[L_\odot]$	$\log_{10} E_{absorbed}$ associated with A_V
30	Lu	$[L_\odot]$	$\log_{10} L$ (U band)
31	Lj	$[L_\odot]$	$\log_{10} L$ (J band)
32	L1400	$[L_\odot]$	$\log_{10} L$ in 200 Å-wide top-hat filter (at 1400 Å)
33	L2800	$[L_\odot]$	$\log_{10} L$ in 200 Å-wide top-hat filter (at 2800 Å)
34	LHa	$[L_\odot]$	$\log_{10} L(\mathrm{H}\alpha)$
35	LOIII	$[L_\odot]$	$\log_{10} L$(O III)
36	LHb	$[L_\odot]$	$\log_{10} L(\mathrm{H}\beta)$
37	LOII	$[L_\odot]$	$\log_{10} L$(O II)
38	MLv	$M_\odot\ L_\odot^{-1}$	mass-to-light ratio (V band)
39	Av	mag	extinction (V band)
40	lwAgeV	Gyr	light-weighted age (V band)
41	mass_p$_{xxx}$*	$[M_\odot]$	percentiles of $\log_{10} M_{star}$
42	sfr_p$_{xxx}$*	$[M_\odot\ \mathrm{yr}^{-1}]$	percentiles of $\log_{10}$ SFR
43	Lv_p$_{xxx}$*	$[L_\odot]$	percentiles of $\log_{10} L$ (V band)
44	LIR_p$_{xxx}$*	$[L_\odot]$	percentiles of $\log_{10} L$ (8-1000 μm)
45	energy_abs_p$_{xxx}$*	$[L_\odot]$	percentiles of $\log_{10} E_{absorbed}$ associated with A_V
46	Lu_p$_{xxx}$*	$[L_\odot]$	percentiles of $\log_{10} L$ (U band)
47	Lj_p$_{xxx}$*	$[L_\odot]$	percentiles of $\log_{10} L$ (J band)
48	L1400_p$_{xxx}$*	$[L_\odot]$	percentiles of $\log_{10} L$ in 200 Å-wide top-hat filter (at 1400 Å)
49	L2800_p$_{xxx}$*	$[L_\odot]$	percentiles of $\log_{10} L$ in 200 Å-wide top-hat filter (at 2800 Å)
50	LHa_p$_{xxx}$*	$[L_\odot]$	percentiles of $\log_{10} L(\mathrm{H}\alpha)$
51	LOIII_p$_{xxx}$*	$[L_\odot]$	percentiles of $\log_{10} L$(O III)
52	LHb_p$_{xxx}$*	$[L_\odot]$	percentiles of $\log_{10} L(\mathrm{H}\beta)$
53	LOII_p$_{xxx}$*	$[L_\odot]$	percentiles of $\log_{10} L$(O II)
54	ssfr_p$_{xxx}$*	$[\mathrm{yr}^{-1}]$	percentiles of $\log_{10}$ sSFR
55	Av_p$_{xxx}$*	mag	percentiles of extinction (V band)
56	t_imf	K	T_{IMF}, maximum-likelihood temperature of Kroupa IMF (Jermyn et al., 2018)
57	t_imf_siglo	K	T_{σ_-}, uncertainty in best-fit temperature of Kroupa IMF
58	t_imf_sigup	K	T_{σ_+}, uncertainty in best-fit temperature of Kroupa IMF
59	outlier	—	bad local solutions that appear as a grid of T_{IMF} and sSFR (see § 2.9)

[1] xxx is one of [025, 160, 500, 840, 975] percentiles, i.e. [2.5%, 16%, 50%, 84%, 97.5%], of a PDF of a quantity.

Note—Table 2.3 is published in its entirety in the machine-readable format and made available online. A portion is shown here for guidance regarding its form and content.

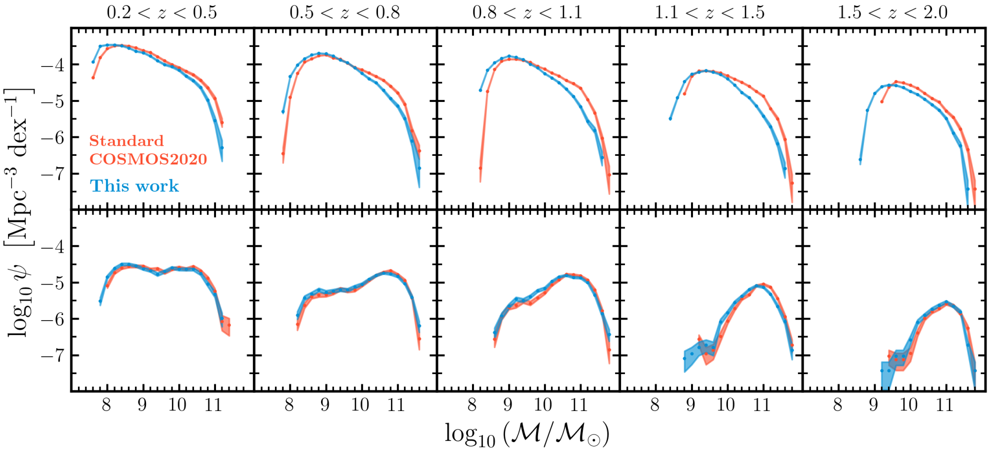

Figure 2.13: Stellar mass functions for star-forming (top) and quiescent (bottom) galaxies at different redshift windows in $0.2 < z < 2.0$. The standard stellar mass has been converted from Chabrier to Kroupa IMF to match the properties in the value-addded catalog. Most masses of active galaxies have been shifted towards lower values as a result of using the best-fit IMF. On the other hand, the masses of the passive galaxies remain similar to the properties with the Milky Way IMF. This differential change in stellar mass results in a systematic change of the quiescent galaxy fraction as a function of the mass, which implies a sharper effect of mass downsizing (see Figure 2.6).

Chapter 3

A Case Study of an Active Galactic Nucleus: A Candidate for the Most Extreme Star Formation?

This chapter contains the following journal article:

> **“A Broad-line Quasar with Unexplained Extreme Velocity Offsets: Post-shock Outflow?”**
>
> Published in The Astrophysical Journal (ApJ), Volume 944, Issue 2, id.217, 11 pages, February 2023.
>
> Authors: Vadim Rusakov, Charles L. Steinhardt, Malte Schramm, Andreas L. Faisst, Daniel Masters, Bahram Mobasher, and Petchara Pattarakijwanich.

Abstract

The quasar SDSS 0956+5128 exhibits three distinct velocity components with large offsets in emission: the systemic velocity of [O II], [O III] and [Ne III] narrow lines have redshift $z = 0.7142$; broad Mg II line is shifted by -1200 km s^{-1} with respect to the narrow lines; broad Hα, Hβ lines are at -4100 km s^{-1}. We present new Hubble Space Telescope spectra of Lyα and C IV emission lines and high-resolution images of the quasar. The offsets of these lines are consistent with the velocity component of the Balmer emission, and the photometry in optical and near-infrared wavelengths does not show any signs of recent mergers in the host galaxy or irregularities in the location of the quasar. The data do not confirm predictions of the previous most-likely hypotheses involving a special orientation and morphology of the quasar disk, such as in the recoiling black hole scenario, neither it is consistent with accretion disk winds. Instead, based on the cumulative evidence, we propose a new scenario, in which the broad line region is in the state of outflow caused by a strong shock wave, with a supernova as a possible event for producing the shock ejecta.

3.1 Introduction

Although there initially appeared to be several subtypes of active galactic nuclei (AGN) and quasars (QSO) (Antonucci, 1993), it has been believed for approximately three decades that nearly all observed AGN are consistent with being similar objects observed from different lines of sight (Urry & Padovani, 1995; Miller et al., 1991; Bailey et al., 1988; Lawrence & Elvis, 1982; Antonucci & Miller, 1985; other references in Antonucci, 1993). One consequence is that all quasar spectra exhibit the same set of significant spectral lines: (1) broad emission (or absorption) lines (BEL) including C IV, Lyα, Hα, Hβ and Mg II, among others, with Doppler widths of $\sim 10^4$ km s^{-1} (Vanden Berk et al., 2001; Murray et al., 1995; Wills et al., 1993), that are normally virialized (Shapovalova et al., 2001; Dietrich et al., 1998; Korista et al., 1995); (2) narrow emission lines, including [O III]$\lambda\lambda$4959,5007, [Ne II]λ3869 and [O II]λ3727 with widths of $\sim 500 - 1000$ km s^{-1}; and (3) a wide range of possible narrow emission or absorption lines from the host galaxy, with widths of < 500 km s^{-1}. These observations have led to a physical picture in which this emission originates, respectively, from a broad-line region (BLR) ~ 1 pc from the central supermassive black hole, a narrow-line region (NLR) $\sim 10^3$ pc away, and the remainder of the host galaxy, which might extend to $\sim 10^4 - 10^5$ pc out. Although inflows or outflows might skew the profiles of these lines (cf. Strateva et al., 2003; Eracleous et al., 1995; Gaskell, 1982), they all emanate from objects in the same host galaxy, and thus are likely centered at the same Doppler velocity (equivalently, redshift) with respect to the observer.

However, a single quasar among the more than 10^5 quasars found in Sloan Digital Sky Survey (SDSS) appears to be entirely incompatible with this model. SDSS J095632.49+512823.92 (hereafter, SDSS 0956+5128) exhibits three distinct and non-typical features that in combination make this object unique (Steinhardt et al., 2012) (hereafter, S12).

At first, there are three significantly different velocity components, corresponding to $z = 0.714$, $z = 0.707$, and $z = 0.690$. The narrow line emission of [O II], [O III] and [Ne III] provides the systemic redshift of the galaxy $z = 0.714$. The blueshift of broad Balmer emission lines and Mg II from the host galaxy is $\sim$ 4100 and $\sim$ 1200 km s^{-1}, respectively. It is not surprising on its own to observe three components. For example, such objects as I Zw 1 are known to exhibit more than two velocity systems with blueshifts from the systemic redshift (Laor et al., 1997; Vestergaard & Wilkes, 2001). However, unlike such quasars, the broad emission lines in SDSS 0956+5128 are not double-peaked or strongly skewed (as in the examples that were studied in detail in Eracleous et al., 1995; Tsalmantza et al., 2011; Eracleous et al., 2012). They are symmetric and completely offset and therefore appear to be consistent with some kind of physical offset of the BLR, such as an outflow.

Only a handful of objects studied in outflows have been observed with nearly as high offsets in Hβ, Hα and Mg II. In fact, offsets of the similar magnitude have been found more often in higher-ionization lines, such as Si IV, C IV or higher, and even so in the extreme tail of their offset distribution, as shown by Yu et al. (2021) in SDSS DR7 (Shen et al., 2011) and other quasar samples. The objects with symmetricaly-offset lines have been studied in connection with the recoiling black holes (BH; Bonning et al., 2007). In fact, no recoil candidates have been identified with the BLR velocity as high as in the SDSS 0956+5128 which is almost twice the second highest offset (Chiaberge et al., 2017).

In addition, the broad Mg II line, which is typically found to be consistent with the systemic velocity (Shen et al., 2016; Hewett & Wild, 2010), is offset by -1200 km s^{-1} from the host lines, and thus by $+2900$ km s^{-1} from Hα and Hβ. No other quasar spectra in the SDSS that have coverage of Balmer lines and Mg II are known to exhibit a strong velocity offset between these lines in the BLR, including the candidates for BH recoils (eg., Bonning et al., 2007). Indeed, such an offset between Mg II and hydrogen lines, which have similar ionization potentials, should not be possible if both are emitted from nearby parts of the BLR.

It is worth noting that originally S12 reported that Hα and Hβ broad lines are asymmetric, while Mg II is symmetric, contrary to the claim that all lines are symmetric in this work. This is because there does not appear to be a strong asymmetry indicative of different velocity components in the Balmer lines. It may rather be attributed to the clumpy nature of the BLR leading to a weak skew of the shapes of broad lines (Risaliti et al., 2005, 2002; references in Elitzur & Shlosman, 2006).

Several mechanisms or explanations were considered in S12 to describe SDSS 0956+5128, but none seems capable of producing all of the observed features. The ideas included multiple objects along the line of sight, accretion disk winds, special morphological configurations or a recoiling black hole. It is unclear which other known mechanism might be responsible for the behavior observed in SDSS 0956+5128. However, one way to distinguish between possible mechanisms is that different explanations make distinct predictions for the velocities of higher-ionization lines.

To examine the applicability of different scenarios, additional observations of high-ionization lines, like C IV, are needed. Combining it with the high-resolution photometry of the central region allows a test of these hypotheses.

Here, new *Hubble Space Telescope (HST)* observations of C IV and Lyα lines and photometry of the central region of the host galaxy are presented and analyzed. Based on these data, we attempt to distinguish between the previously proposed mechanisms. As none of them appears to match these observations, a new mechanism is proposed to explain SDSS 0956+5128.

New *HST* measurements of the previously unobserved C IV and Lyα BELs in the UV spectrum (§ 3.2) and photometric observations of the host galaxy at high resolution (§ 3.3) are presented in the following sections. The broad UV lines are symmetric and appear to have the offset consistent with the Balmer lines. No irregularities are seen in the photometry of the central region of the galaxy. While the QSO is seen as spatially offset, it is within 3σ resolution. § 3.4 reviews hypotheses that were previously proposed to explain SDSS 0956+5128, such as a combination of the recoiling BH scenario and a double-peaked emitter, and describes why it is a challenging problem. Instead, the cumulative evidence shows a peculiar velocity pattern of the BLR consistent with a strong shock outflow from the central region. Discussion of the observations and a new hypothesis along with final thoughts are presented in § 3.5.

This work adopts a flat ΛCDM cosmology with $\Omega_m = 0.3$, $\Omega_\Lambda = 0.7$, and $H_0 = 70$ km s^{-1} Mpc^{-1} throughout.

3.2 HST Spectrum

The near ultraviolet (NUV) spectrum of SDSS 0956+5128 was recorded with the Space Telescope Imaging Spectrograph (STIS) onboard the *HST* (Proposal 15872; Steinhardt et al., 2019). The first order G230L long slit grating was used allowing for spatially resolved spectroscopy with $0.025''$/pix ($\sim$ 180 pc/pix at $z = 0.7142$) and low-to-medium spectral resolution with $R \sim 500 - 1010$ (translates to $600 - 300$ km s^{-1} resolution at short to long wavelengths) in the NUV. The *HST* pipeline CALSTIS (Sohn, 2019) used to reduce the spectrum allowed the detection of C IV and Lyα lines. The NUV spectrum allowed the detection of C IV and Lyα lines.

The background in the spectrum was fitted with the exponential function in linear wavelength assuming that the continuum is dominated by the quasar emission. The wavelength windows used for the fit ($1290 - 1460$, $1580 - 1810$ Å) were expected to have little or no contamination from prominent line emission or Fe II, Fe III pseudo-continuum described in Vestergaard & Wilkes (2001) and were similar to the clear quasar-continuum windows in Francis et al. (1991). The slope of the model continuum was used to validate the quasar nature of the spectrum. Calculated as $F_{\nu 1}/F_{\nu 2} = (\nu_1/\nu_2)^\beta$, it was found to be $\beta = -1.18 \pm 0.01$, which loosely agrees with the observed distribution of slopes of typical quasars, although in the redder part (Davis et al., 2007). The model was used for the calculation as a cross-check, as the observed spectrum did not cover the wavelengths normally used above 1850Å.

The background-subtracted C IV and Lyα are shown in Figure 3.1. The systemic Lyα line is best fit with a Gaussian component at $z = 0.7135 \pm 0.0003$, at 2.3σ deviation from the systemic redshift measured in S12. The line profile is strongly asymmetric, with the most likely contribution from a blueshifted broad Lyα component. This component is best fit at $z = 0.6909 \pm 0.0026$ with FWHM $\sim 11511 \pm 1781$ km s^{-1}. This profile is consistent with the observations of Balmer lines in S12, where the narrow peaks are accompanied by the completely blue-shifted broad emission. When considering other possible contributions to this blueshifted excess, Si III λ1206.5 and O V λ1218 lines coincide with the profile at $z = 0.707$

and $z = 0.690$, respectively (associated with two offsets identified in S12). However, neither the expected narrow width of these lines, nor the expected low flux can explain the strong broad excess that is best described by the broad Lyα emission.

Additionally, there appears to be a broad excess of flux in the red wing of the profile, which could not be caused by either Si III, O V, Fe II or Fe III lines at any one of the involved redshifts. Including this component of the profile improves the fit. However, the widths and positions of the broad Lyα and the unknown component become less constrained, as reflected in their uncertainties (see Table 3.1). The small bump at rest wavelength 1240 Å suggests that the unknown broad component may be the offset N V emission. With this, the fit of the whole profile was produced with $\chi^2_\nu = 0.77$, where the suspected broad N V line had FWHM $= 2907 \pm 2862$ km s^{-1} at $z = 0.6914 \pm 0.0051$. There is however no distinct narrow N V λ1240 component. The offset of the broad Lyα and N V components is at 1.4 and 3.2σ levels, respectively.

The redshift of C IV is measured at $z = 0.6907 \pm 0.0008$ with $\chi^2_\nu = 0.69$ per degree of freedom. Although due to low spectral resolution and spectral purity the line appears to be strongly affected by the noise, it is above 4.2σ noise level. The spectrum was resampled to improve its signal to noise ratio. No other distinct emission or absorption features could be observed; however, the line can usually be contaminated by some narrow features.

As the left wing of the profile at $1490 - 1520$ Å (rest frame) could be affected by the Fe II and Fe III and Si II at 1531 Å emission at the systemic redshift (Vestergaard & Wilkes, 2001), the width of the C IV fit was cross-checked by estimating the BH mass. The empirical mass estimator from Dalla Bontà et al. (2020) for single epoch measurements yields $log(M_{BH}/M_\odot) = 8.80 \pm 0.16$, which is 1.0$\sigma$ away from the Mg II-based estimate of $log(M_{BH}/M_\odot) = 8.65$ from S12. The relations based on the C IV line width are less well constrained than those made with the Hβ line mainly due to the lack of observations in the UV. The literature on the most commonly identified agreements and differences in the estimators has been summarized in Dalla Bontà et al. (2020). Their empirical estimator was calibrated against identified correlations in the residuals with the reverberation mapping measurements. In this specific case if the Fe emission acted to decrease the width of the C IV profile, this would only make the disagreement with other estimators worse. Therefore, the cross-check above is used as the main argument for the broad C IV line producing dominant contribution to the profile. It is concluded that the C IV profile is observed as emission coming entirely from the BLR with the velocity offset. How-

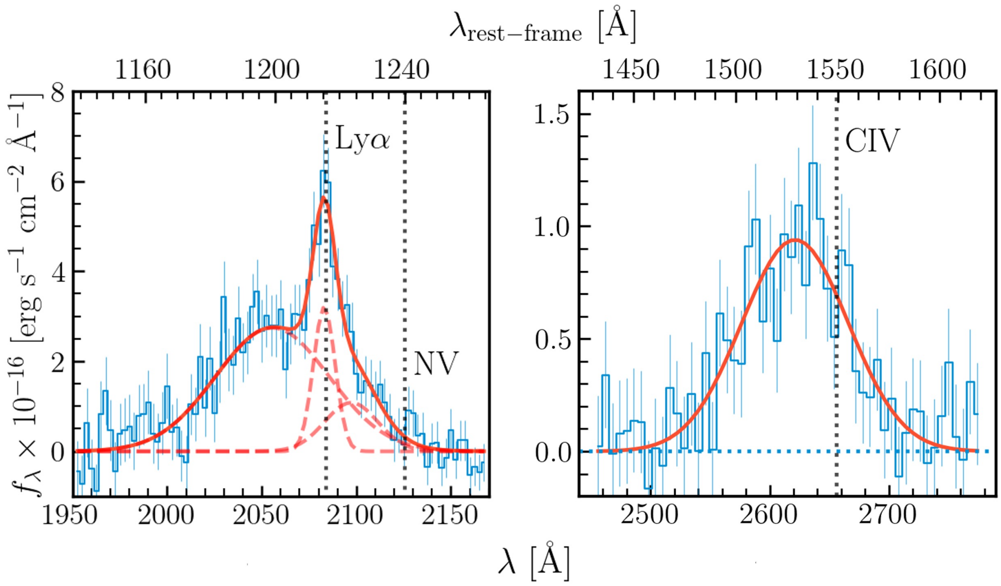

Figure 3.1: Lyα λ1215 and C IV λ1549 spectrum profiles. Vertical dotted lines indicate the systemic redshift of line centroids. Lyα profile shows significant flux excess at $\sim$ 2055 Å in the observed frame, fitted here as the offset broad Lyα emission. The excess of flux in the long-wavelength tail is suggested to arise from the offset N V broad emission, as there is a hint at the narrow N V λ1240 line, which is unresolved in this spectrum. The spectrum is resampled to $\sim$ 3 Å per bin. C IV profile does not appear affected by strong emission or absorption features when resampled to $\sim$ 6 Å per bin. Verifying the BH mass using the C IV estimator suggests the width of the fitted profile is the real C IV width (see text). The line appears completely offset from the host quasar redshift.

ever, it should be stated that applying mass estimators to strong outflows makes the estimates not trustworthy and speculative.

3.3 HST Images

As part of the same proposal (15872), ACS/WFC camera of the *HST* was used to take 6 dithered images in F606W and 4 in F850LP filters to produce the combined images totaling 2075 and 2300 second exposures, respectively. The individual exposures were aligned, background-subtracted and drizzled by `grizli` pipeline (Brammer & Matharu, 2021). The final products represent the combined mosaics of these dithered images for each filter.

The reconstruction of the quasar emission was performed by using an effective PSF (ePSF) constructed with `photutils` package (Bradley et al., 2020) and based on 6 foreground stars in the images utilised here. It is an empirical model based on the selection of stars in the images (Anderson

Table 3.1: Measurements of lines in NUV spectrum (this work), optical and NIR (S12). The offsets are stated with respect to the systemic redshift ($z = 0.7142$) reported in S12.

Line	Redshift	FWHM (km s^{-1})	Offset (km s^{-1})
	Broad Emission Lines		
N V $\lambda1240$?	0.6914 ± 0.0051	4917 ± 4840	-3996 ± 893
C IV $\lambda1549$	0.6907 ± 0.0008	12491 ± 953	-4107 ± 143
Lyα $\lambda1215$	0.6909 ± 0.0026	11511 ± 1781	-4079 ± 457
Hα $\lambda6563$	0.690	$\sim$7200	-4100
Hβ $\lambda4861$	0.690	$\sim$7200	-4100
Mg II $\lambda2798$	0.7071 ± 0.0006	12800 ± 490	-1200
	Narrow Emission Lines		
Lyα $\lambda1215$	0.7135 ± 0.0003	1978 ± 565	-123 ± 48
[O III] $\lambda4959$	0.714		
[O III] $\lambda5007$	0.714		
[O II] $\lambda3727$	0.714		
[Ne III] $\lambda3881$	0.714		

& King, 2000; Anderson, 2016). It is produced by simply measuring the flux of stellar sources in the vicinity of the target at individual pixels and it represents a map of fractional flux produced by a point source given the optics and the detector sensitivity, i.e. the instrumental PSF scaled by the pixel sensitivity map. This method was shown to be more precise and numerically efficient than deconvolving the photometry and instrumental effects, assuming and then fitting an analytical function. The advantages are particularly justified, when only a single point source is investigated.

Figure 3.2 shows the residuals after fitting and subtracting the best-fit PSF from the images. The fit was performed using the 2D image profile fitting code `IMFIT` (Erwin, 2015) with reduced $\chi_r^2 = 2.83$ for F606W and $\chi_r^2 = 1.36$ for F850LP images. With the pixel scale of 0.03 (0.22 kpc per pixel) the images allowed to resolve the host structure around the AGN. The figure shows both the residuals in terms of the instrumental read-errors and the residuals in units of Poisson σ defined using the average of the counts in the observed and model images. These maps indicate that the residual host emission around the AGN is most significant in the F606W band (up to 5σ, Poisson), while the emission in F850LP (up to $2-3\sigma$) is shallower and more extended outside of the central region than in F606W. This is

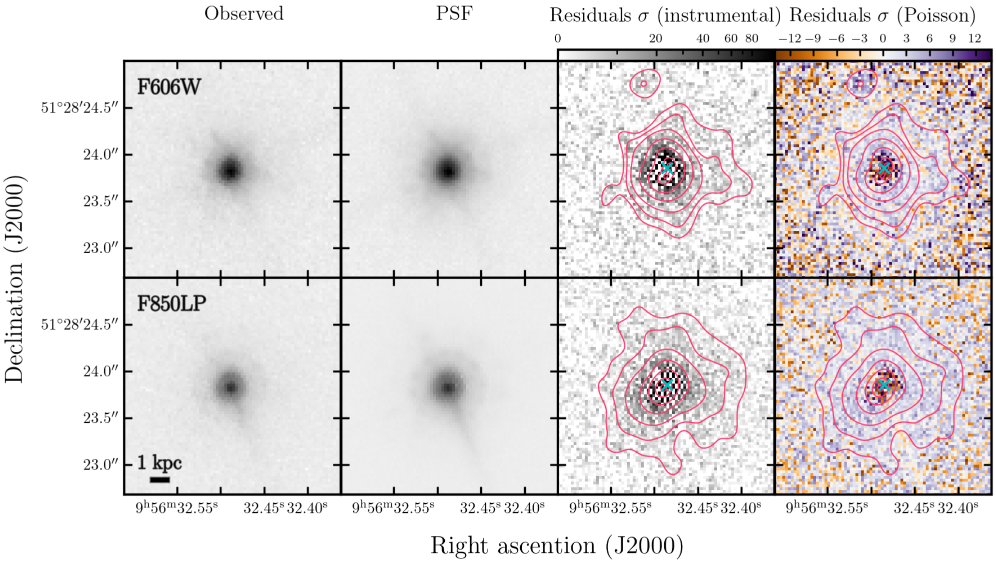

Figure 3.2: HST/ACS images of SDSS 0956+5128: observed image (first column); model PSF (second column); positive residuals after subtracting the PSF in units of instrumental σ-noise (third column); residuals after subtracting the PSF in units of Poisson σ (fourth column). The top and bottom rows shows photometry in F606W and F850LP filters, respectively. Contours show the residual host emission without strong eccentricity or possible post-merger disruption (smoothed with a 3.3-pixel Gaussian kernel). The outer-most isophotes extend to the 50th percentile in F606W and F850LP indicating that the emission is more centrally concentrated in F606W and more extended in F850LP. The best-fit centers of the quasar emission are marked with the cyan crosses, where the PSF centers are offset by 1.1 (F606W) and 1.4 (F850LP) pixels from the isophotal centers. This offset is within the 3σ offset of ~ 1.5 pixels). The scale is 0.03 arcsec per pixel (0.22 kpc).

roughly in agreement with the relative amount of flux of the model SED emission of the host galaxy at the respective wavelengths presented in S12.

The residuals in either filter do not indicate any disruption or deformation in the central structure of the apparently elliptical light profile, which would be expected from a recent galaxy merger. However, it was not possible to perform a detailed study of the host galaxy profile due to the overall shallow photometry. The cyan 'x'-marks indicate the best-fit centers of the quasar emission, which are misplaced from the center of the isophotal host emission by 1.1 (0.24 kpc) and 1.4 (0.31 kpc) pixels in F606W and F850LP, respectively. Given the resolution, the offset up to ~ 1.5 (3σ) pixels is allowed, which makes the best-fit QSO location consistent with the center of the host emission.

3.4 Previously Proposed Explanations

There exist several mechanisms that are responsible for creating different distinct velocity components in BLRs of quasars. However, none of them appears to provide a full explanation for the observed features of SDSS 0956+5128. Those include outflows, quasar morphology and orientation or quasar motion with respect to its host that could correspond to one or both of the velocity components in SDSS 0956+5128. Specifically, S12 considered multiple objects along the line of sight, double-peaked emitter profile and a recoiling black hole. Another considered mechanism is accretion disk winds that may be responsible for velocity profiles typically seen in most of the QSOs with outflows. This section describes how the previous and new evidence from SDSS 0956+5128 fits within these scenarios and shows that none of them are capable of explaining the observation completely.

Multiple objects along the line of sight

Perhaps the simplest explanation for multiple velocity components would be multiple objects along the same line of sight. However, this explanation cannot produce the broad lines observed in SDSS 0956+5128, There is a unique set of narrow lines, consistent in their redshift, and two velocity components, represented by either broad Mg II or Balmer lines, but not both. With two objects along the line of sight, two sets of narrow lines would have to be present, even if there was a specific combination with a strong Mg II broad emission and very weak Balmer lines in one object and a very weak Mg II and strong Balmer emission in the other.

In addition, the narrow lines argue against this explanation. Narrow Balmer lines at the systemic velocity indicate that the central region of the presumed host galaxy is illuminated by the quasar. The broad Balmer lines are bluer than the host. Thus, if along the same line of sight, they would need to be in front of the host and unable to produce these features. Therefore, a scenario with three distinct components in the same system has to be considered: emission of the host ($z = 0.714$) in the NLR, Mg II ($z = 0.707$) and Balmer ($z = 0.690$) emission in the BLR.

Disk winds

In the context of a single QSO system, one common mechanism thought to be responsible for outflows in the BLR is accretion disk winds (e.g., models by Murray et al., 1995; Mathews & Blumenthal, 1977). In support of these models, Gaskell (1985) found evidence that BLR clouds could be radiatively accelerated. It was proposed and modeled that radiation pressure could be responsible for accelerating the gas clouds radially outwards (Emmering et al., 1992; Everett, 2005).

In such a scenario, the velocity of the outflow is highest for the high-ionization material of the BLR and decreases for species with lower-ionization energies. Examples of such profiles can be seen in Meyer et al. (2019); Shen et al. (2016); Marziani et al. (2010, 1996); Brotherton et al. (1994). As the ionization potentials are correlated with the radial distances of emission lines, the lines like N V, C IV and other high-ionization lines experience some of the largest relative velocities reaching several thousands km per second (Yu et al., 2021). The intermediate- to low-ionization emission, including hydrogen lines and Mg II is typically seen accelerated to at most a few hundred km s^{-1}. Often Hα, Hβ and Mg II are consistent with the systemic velocity to within $\sim$ 200 km s^{-1} (Shen et al., 2016; Hewett & Wild, 2010).

Although such a negative velocity gradient could produce a difference in emission line velocities, the difference seen between the hydrogen lines and Mg II in SDSS 0956+5128 is too steep and too high for the lines of such similar ionization potentials. For instance, Meyer et al. (2019) show that the offset velocities of Mg II and other low-ionization lines are typically identical in spectroscopically observed SDSS quasars, with velocity shifts well within a few hundred km s^{-1} at $z < 7$. Moreover, in the rare cases where Mg II blueshifts of $\sim 10^3$ km s^{-1} are reported, they are generally connected with other mechanisms (as in the recoiling black hole candidate, 3C 186, in Chiaberge et al., 2017).

The similarity between ionization potentials of Hβ and Mg II alone may not be indicative of their physical proximity, especially if the lines originate from fully and partially-ionized regions and their emission is driven by different excitation mechanisms. However, the correlation between the radius of the species in the BLR and the accompanying continuum luminosity (at $\lambda = 5100$Å and 3000 Å) indicates that they are likely coming from the adjacent gas shells in the BLR. Figure 3.3 shows estimates with several of such empirical relations. They may not be applicable to all quasars, because they are based on different sample selections. However, any pair of radius estimates show that Hβ and Mg II here are closely spaced and Hβ is closer to the center on average.

Thus, if a negative velocity gradient is responsible for the extreme offsets of the hydrogen and Mg II lines in SDSS 0956+5128, there should be an even larger difference when Mg II is compared with high-ionization lines. For example, such trend was found in the offsets of emission lines of I Zw 1 (Laor et al., 1997; Vestergaard & Wilkes, 2001) and other quasars (Corbin, 1990; Espey et al., 1989; Wilkes, 1986). However, as shown in § 3.2, this is inconsistent with the new *HST* observations presented in this work, especially with the C IV, possibly N V and the hydrogen lines being symmetric and part of the same velocity system at -4100 km s^{-1}.

QSO jets

Alternatively, QSO jets that provide a way of losing the angular momentum for the supermassive black hole (SMBH) can cause QSO outflows (Zheng et al., 1990). Even though the jets are highly collimated, they may cause outflows in the BLR assuming a high covering factor of the clouds. It was shown in Zheng et al. (1990) that double-peaked Balmer emission can be produced in such AGN models. However, this does not explain the symmetric single-peaked lines observed in SDSS 0956+5128.

Double-peaked emitter

In another scenario, large line shifts of over 4000 km s^{-1} observed in some galaxies can be described by models with non-axisymmetric accretion disks (Strateva et al., 2003): flattened, eccentric disks (or other forms of asymmetries) and a preferred inclination angle (Chen & Halpern, 1989; Eracleous et al., 1995). The problem in this case is that BELs in such systems produce double or asymmetric profiles. S12 reported that the Balmer lines in SDSS 0956+5128 have asymmetric profiles, with a faint, broad component and that Mg II, in contrast, is symmetric. However, the asymmetry appeared only in one of three independent observations (S12).

If the model of a double-peaked emitter is allowed to have sufficiently many parameters, it is possible to produce a reasonable fit to the spectrum in most cases. However, in this case one double-peaked emitter is not able to explain scenarios in which different lines show different offsets. At least two eccentric emitter components are required to provide an explanation for the two offsets, but still not sufficient to produce a symmetric (non-double) Mg II, Lyα and C IV (and possibly N V), unless these lines have double profiles with the second component being very weak.

Recoiling black hole

Finally, S12 suggested that SDSS 0956+5128 may be a recoiling BH in a post-merger galaxy, in which the BLR is a combination of eccentric and circular components. A SMBH resulting from coalescence of two smaller SMBHs can receive a kick in some direction, depending on the rotation properties of the system (Campanelli et al., 2007b; Schnittman & Buonanno, 2007; Loeb, 2007).

It was shown that such a BH can still exhibit symmetric BELs with the offset of over 1000 km s^{-1} (Merritt et al., 2006; Loeb, 2007). However, an offset of $\sim$ 4000 km s^{-1} would be difficult to produce. Some analytical and numerical considerations limit the maximum recoil velocity to $\sim$ 4000 km s^{-1} (Baker et al., 2008; Campanelli et al., 2007a,b) or even lower (Healy et al., 2014), while others can reach up to $\sim$ 5000 km s^{-1} for special configurations (Lousto et al., 2012). In observations, one potential candidate is the object CID-42 (Civano et al., 2010, 2012; Blecha et al., 2013), with the offset of up to 1300 km s^{-1} detected in the broad Balmer emission. Another candidate for a SMBH recoil with more BEL detections, 3C 186 Chiaberge et al. (2017), shows the highest known offset of $\sim$ 2100 km s^{-1}, which is second only to SDSS 0956+5128 with the offset nearly twice as high ($\sim$ 4100 km s^{-1}). In addition, the spectroscopic velocity profile of 3C 186 appears to be constant with respect to the ionization potential of C IV, C III] and Lyα, as well as Mg II.

In SDSS 0956+5128, C IV (and possibly N V) and the hydrogen lines are consistent with this scenario; however, Mg II is not. Given the similarity of the ionization potentials of hydrogen and Mg II lines, it seems very unlikely that the Mg II region could be moving $\sim$ 2900 km s^{-1} slower than the rest of the recoiling BLR. One possibility is to assume that Mg II is consistent with the recoil scenario and all of the BLR is offset by at least the offset of Mg II (-1200 km s^{-1}). Then even slightly higher-ionization lines, including the hydrogen lines, could arise due to an eccentric emitter disk that introduces additional offset on top of the recoil and causes asymmetry of the Balmer lines. Therefore, in this scenario, the Balmer and Mg II emission must come from separate locations, with the latter being further out and the higher-ionization lines, like C IV or N V, must also have the same asymmetry, as reported for the Balmer lines in S12.

In support of the idea of the recoiling BH, S12 showed using ground-based photometry that the peak of intensity in SDSS 0956+5128 was possibly offset from the center of light in the host galaxy, although the data had low resolution and systematic effects in PSF fitting were not ruled out.

Additionally, photometric decomposition showed that the host is a dusty galaxy, which can be consistent with various states of galaxy evolution, including a possible post-merger. S12 showed that based on the timescale for the BLR to sustain emission after the quasar accretion was disrupted, the recoil could have occurred in the past 140 Myr. This could allow for the host galaxy to preserve the evidence of a recent merger on a less than dynamical time, detectable in the follow-up resolved observations.

However, the new evidence presented from *HST* does not hold any indications of a BH recoil that could result from a previous galaxy merger. It is shown in § 3.3 that the QSO, fitted with a PSF, is spatially consistent with location of the isophotal center of the residual galaxy emission and no strong irregularities in the structure are seen that could result from a recent galaxy merger, although the photometry is not deep enough to accurately fit the host morphology. It remains possible that the strong signatures of the merger could have been erased to the point of being undetected at the given resolution. Nevertheless, new observations of the high-ionization line C IV and low-ionization Lyα appear to be consistent with the offset of the Balmer lines, they are symmetric (see Section 3.2). The symmetry is contrary to the expectation from the BH recoil hypothesis. It was also shown by S12 that the system lies on the standard $M_{BH} - M_{bulge}$ galaxy mass relation, with the virial mass of the SMBH of $log(M_{BH}/M_{\odot}) = 8.65$ (S12) lying close to the empirical relation in the plane of the galaxy luminosity and the black hole mass. Therefore, this does not provide any sharp indications that the SMBH does not belong to the host. In this context, the evidence suggests that the offsets in SDSS 0956+5128 do not appear to be caused by the motion of the quasar, but are rather intrinsic to the QSO.

In § 3.5, we argue that the radial velocity profile in the BLR of SDSS 0956+5128 is reminiscent of the post-shock outflow and use the idea of star formation in the accretion disks (eg., from Goodman & Tan, 2004) to support this mechanism for causing strong outflows in the BLR of quasars.

3.5 Interpretation

The observations of SDSS 0956+5128 appear to be inconsistent with known physical mechanisms and suggest that an outflow with very distinct velocity signature is responsible.

The event that produced the outflow must have an origin at the BH or close to it. This appears to be the case, because the symmetry of the BELs suggests a spherically uniform outflow. Additionally, the whole BLR

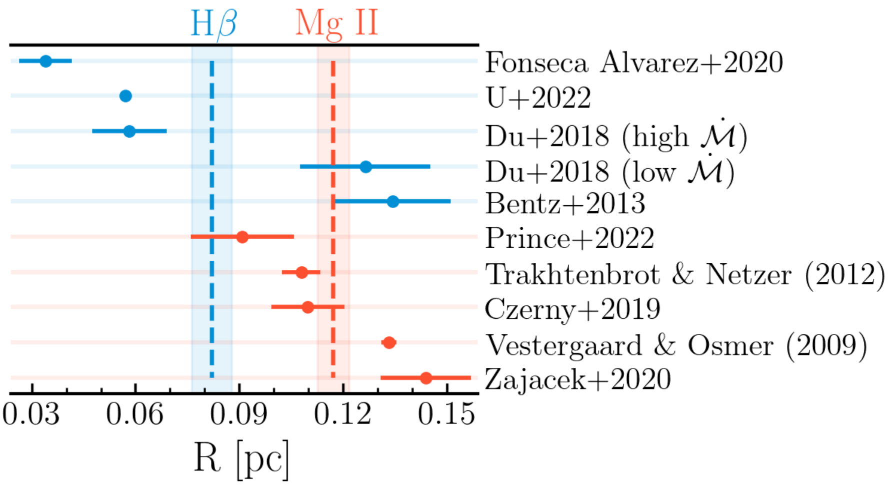

Figure 3.3: Compilation of various calculations of the radii of Hβ and Mg II obtained using the respective luminosities λL_{5100} and λL_{3000} of the continuum in SDSS 0956+5128. Individual estimates are shown with 1-σ uncertainties. The average radii are shown as vertical dashed lines with their corresponding shaded uncertainty bars. The estimates are based on the empirical radius-luminosity relations for quasars. Some of the studies use very different sample selections, such as different accretion rates $\dot{\mathcal{M}}$ in Du et al. (2018), to define the relations. Nevertheless, they produce similar radii for the two species here, where Hβ is on average is closer to the center than Mg II.

appears to be affected, where the radial velocity is constant across a large fraction of the BLR, between the high-ionization region and low-ionization hydrogen lines. Finally, there appears to be a drop-off of the outflow velocity starting from the location where Mg II is produced. Therefore, it may be safe to assume any origin of such event within the inner boundary of the BLR, with its effects limited to the BLR outskirts.

Clearly, some extreme physical conditions must be at play. The event has to be consistent with the outflow energetically and with the observed radial velocity profile, as indicated by the offsets of the broad lines and their expected radial distances. The upper limit on the time of the event can be placed by using the velocity of the outflow.

Below, a shock wave from an energetic explosion is postulated as a mechanism for causing an outflow. It is shown that this mechanism can be consistent with the observed features in SDSS 0956+5128. Then the plausibility of the extreme physical conditions due to a supernova explosion is considered, along with a discussion of whether stars can exist in close proximity of a SMBH and how they can appear there in the first place.

Post-shock outflow

The velocity profile of the outflow as a function of radius in the BLR of SDSS 0956+5128 is strongly reminiscent of that of a “shocked” material (Taylor, 1950), as it shown in this section. It is expected that the radial profile in terms of increasing radial distances is as follows: C IV, Lyα, Hα, Hβ, Mg II, where Mg II must be at least as far out as the Balmer line emission. Based on the spectroscopic observations made in Section 3.2 here and in S12, the outflow velocity profile is constant at $\Delta V \approx -4100$ km s^{-1} starting at the location of the C IV line and extending out to the hydrogen lines. Then the radial velocity drops to -1200 km s^{-1} at the location of Mg II. Assuming the velocities estimated from several spectra across an extended timeline are accurate, there would be only one explanation for different offset velocities of the Balmer lines and Mg II: the latter line must originate at larger radii due to its lower ionization energy. In this case, the overall velocity profile is characteristic of a post-shock outflow, such as the outflows in the interstellar medium (ISM) produced by supernova (SN) explosions.

Assuming a uniform density of the medium, the evolution of shocks can be described as a three-phase process that starts with a *free expansion* at high pressure relative to the surroundings, during which the mass of the medium swept up by the shock wave along the direction of travel is insignificant compared to the mass of the shock material itself. Thus, the energy and momentum of the wave are conserved and the kinetic energy E_k is:

$$E_k = M_{ej} V_{ej}^2 / 2, \tag{3.1}$$

where M_{ej} and V_{ej} are the mass and velocity of the ejecta.

As the shock shell expands in radius, it is opposed by a larger mass of the ambient medium. When the two masses become equal, the shock enters the *Sedov-Taylor phase* (Taylor, 1950). There, the ejecta start to lose its momentum, while the matter is too heated to irradiate, so the system remains adiabatic. At this stage, the expansion of the shock radius R_S with time t is found to depend entirely on the initial kinetic energy E_k and density of the medium ρ_0:

$$R_s(t) \propto E_k^{1/5} \rho_0^{-1/5} t^{2/5}. \tag{3.2}$$

Finally, as the temperature of the shock drops, C, N, O ions start to recombine helping to cool the shock material efficiently, which starts to loose its energy radiatively until the flow becomes subsonic and merges with the surrounding medium.

This evolution can be matched with the velocity components observed in SDSS 0956+5128, as illustrated by the velocity and distance profiles of a shock wave in Figure 3.4. In this interpretation, the velocities presented here sample the first two phases: C IV, Lyα, Hβ and Hα represent the region in the *free expansion phase*, while Mg II is in the *Sedov-Taylor region.* Also, in the analysis above the high-ionization N V line[1] was possibly identified with the offset placing it consistently with the lines in the first phase. This phase is sampled well with 4 or 5 lines probably spanning a significant fraction of the BLR radial profile. However, the second phase is only seen with one BEL (Mg II). Fortunately, there have been two observations of this line 7 years apart to confirm the detection.

The velocity profile of the shock stages shown in Figure 3.4 is annotated with the offset velocities of the corresponding broad lines. While the source energy sets the initial velocity of the flow, the density of the BLR sets the distance and time scale of the shock profile. Here, it was assumed that the density is uniform throughout the region and is equal to the lower limit of $n_e = 10^9$ cm^{-3} in the BLR (Osterbrock, 1989; Kwan & Krolik, 1981). Higher densities act to shrink the distance and time scales.

The velocity that the ambient BLR material gains when it crosses over the shock boundary depends on the ratio between the speed of sound and the shock. The speed of sound in the BLR gas is $c_s \approx 10$ km s^{-1}, assuming the BLR is in photoionization equilibrium and has the uniform temperature of $T = 10^4$ K, which is the minimum required for photoionization (Osterbrock, 1989). Therefore, the outflows observed in SDSS 0956+5128 ($\sim$ 4100 and 1200 km s^{-1}) are strongly supersonic. Hence, the shock wave should be expected even more so, such that the limit as the Mach number $\mathcal{M} \to \infty$ for $\mathcal{M} = v/c_s$ can be safely used. In the reference frame with the shock at rest, the velocity of the post-shock material (v_2, downstream) can be related to the velocity of the pre-shock material (v_1, upstream) using the Rankine-Hugoniot jump condition:

$$\frac{v_1}{v_2} = \frac{(\gamma+1)\mathcal{M}^2}{(\gamma+1)+(\gamma-1)(\mathcal{M}^2-1)}, \tag{3.3}$$

---

[1] N V is the line with the highest ionization potential in our sample, which places it closest to the SMBH.

where $\gamma = 5/3$ is the adiabatic index for an ideal monoatomic gas. The assumption here is that the flow is adiabatic and the entropy is constant across the shock boundary, which holds for the first two stages of the shock wave, before it becomes subsonic and its viscosity cannot be neglected leading to the start of radiative cooling. At $\mathcal{M} \to \infty$, $v_2 \to 0.25 v_1$. Therefore, we would expect the shock to have traversed the locations of the observed broad emission at $v_1 \approx 16400$ km s^{-1} and $v_1 \approx 4800$ km s^{-1} to produce the high ($v_2 \sim 4100$ km s^{-1}) and low ($v_2 \sim 1200$ km s^{-1}) observed velocity components in the BLR, respectively.

Interestingly, under the assumption of the BLR gas density of $n_e = 10^9$ cm^{-3} two key model predictions are in agreement with the independent expectations from the empirical radius-luminosity (RL) relations.

First, the model correctly predicts the location of the Mg II gas. This prediction is made by using the time when the calculated downstream flow (black solid line; left panel in Fig. 3.4) matches the observed velocity offset of Mg II (orange solid line): $t \approx 27$ yr. Based on this time the predicted radius of the Mg II line is 0.131 pc (blue arrow; right panel). This closely agrees with the mean of the estimates from various RL relations: $R_{Mg\ II} = 0.117 \pm 0.005$ pc (see Figure 3.3; Prince et al., 2022; Zajaček et al., 2020; Czerny et al., 2019; Trakhtenbrot & Netzer, 2012; Vestergaard & Osmer, 2009).

Second, the location of the boundary between the first two phases ($\approx$ 0.057 pc) agrees with the location of Hβ from RL relations (blue solid line; right panel). The average of several RL estimators yields $R_{H\beta} = 0.082 \pm 0.006$ pc (see Figure 3.3; U et al., 2022; Fonseca Alvarez et al., 2020; Du et al., 2018; Bentz et al., 2013). This is consistent with the observation that the hydrogen lines are part of the high velocity component. These two predictions are possible only for a narrow range of BLR gas densities around $n_e = 10^9$ cm^{-3} and for a constant density as a function of radius, where the time scale goes as $t \propto n_e^{-1/3}$ in the first phase and $t \propto n_e^{-1/5}$ in the second.

Predicting the mass and type of the candidate supernova star is beyond the scope of this work, but it is possible to estimate an order of magnitude mass of the ejecta and their kinetic energy. The ejecta mass can be obtained by locating the boundary between the first two shock regions. This radial distance encloses the mass of the swept up gas comparable to the mass of the shocked ejecta, as this is the approximate condition for termination of the first phase.

The boundary must lie between the hydrogen lines (eg., Hβ) and Mg II, which are close spatially (see Figure 3.3), but correspond to different velocity components in the BLR. Assuming Hβ is at the boundary (as shown in the right panel of Figure 3.4), we can use the estimated radius of the boundary of 0.057 pc and the BLR density of $n_e = 10^9$ cm^{-3} to estimate the ejecta mass. This produces $M_{ej} \sim 2 \times 10^4$ M$_\odot$.

With the velocities of the BEL offsets in the first phase, the kinetic energy of the event is $E_K = 5 \times 10^{55}$ erg[2]. Here, it is assumed that most of this mass is contained in a thin shell at the radius of Hβ. Therefore, the exploded star must have had an initial mass $M_* \geq M_{ej}$. Such objects have not been observed before, although theoretical considerations of instability growth in the accretion disks of quasars suggest a possibility for formation of stars with masses at least as high as $10^2 - 10^7$ M$_\odot$ (Goodman & Tan, 2004).

Origin of stars in AGN

If a stellar explosion produced the observed features in the spectrum of SDSS 0956+5128, how could a star appear in the vicinity of a SMBH in the first place? And how could it be nearly as massive as 2×10^4 $M_\odot$? The star might be formed either in the proximity of the SMBH or in a host galaxy and then captured into the accretion disk. One way or another, it probably owes its large mass to the abundance of material in the accretion disk of a SMBH.

The growth of supermassive stars may stem from the capture of stars from the host galaxy. The closest galactic source of stars is the bulge that encircles the quasar. Stochastic encounters can result in significant changes of stellar velocities on a relaxation timescale that could lead to stars being deflected off their orbits. A “lucky” star brought to the central object with the mass $10^{8.6}$ M$_\odot$ would not risk being disrupted due to tidal forces, unless it sinks into the black hole. The reason is the tidal radius of BHs with masses $> 10^8$ M$_\odot$ becomes smaller than the Schwarzschild radius. In fact, sinking into the BH would be a more likely outcome, as otherwise reaching an exact stable orbit around the BH would require acquiring a very specific velocity making it very unlikely.

Following on the idea of disk-star interactions as a potential mechanism for removal of angular momentum from AGNs (Ostriker, 1983), Syer et al. (1991) investigated a possibility for stars to be captured by the accretion

---

[2] This energy is 10^4 times higher than the kinetic energy of the ejecta of a core-collapse SN explosion of an 8 M$_\odot$ star.

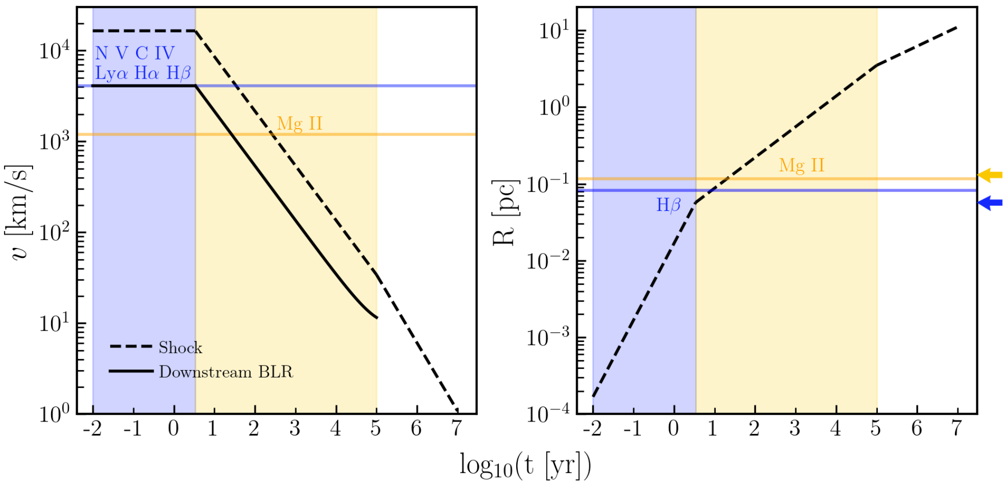

Figure 3.4: Velocity (left) and distance (right) profiles of a shock wave produced by an explosion of a star associated with the ejecta mass $M_{ej} = 2 \times 10^4 \mathrm{M}_\odot$ and kinetic energy $E_K = 5 \times 10^{55}$ erg. The BLR medium has a uniform density ($n_e = 10^9$ cm^{-3}); other main assumptions are stated in the text. Shadowed regions represent different stages of a shock wave traveling through the medium: *free expansion* (momentum and energy conserving); *Sedov-Taylor phase* (adiabatic; energy conserving); *snowplow phase* (radiative and momentum conserving). *Left panel*: two observed offset velocities of BELs are indicated by the horizontal solid lines and correspond to different stages by color, as deduced from their predicted downstream flow velocities (black solid line). The predicted downstream velocity profile is calculated only for the first two phases, before the shock becomes nearly sonic and valid approximations break. *Right panel*: predicted radial profile of the shock wave (black dashed line); the observed radii of Hβ and Mg II are obtained using the mean of the estimates from the RL relations and shown by the horizontal lines with the same colors as before; the yellow arrow indicates the Mg II radius predicted from the time when the shock reaches Mg II location, i.e. the time when the downstream flow coincides with the observed velocity of Mg II in the left panel; the blue arrow show the location of the boundary between the first two phases of the shock flow.

disk for favorable inclinations of stellar orbits. This mechanism was characterised by shorter than the relaxation timescale for delivering stars into the disk. It could be possible as the growth of the gaseous disk and clouds would be expected to extend as far as to the edge of influence of the BH for the stellar bulge. Stars would then be dragged down by the viscous forces to the stable circular orbit over time. If such stellar migration is real, then according to the predictions of Artymowicz et al. (1993), after the QSO acquires a disk and turns on, in the span of 10^8 yr there can be as many as 10^4 captured stars. They would be dragged down the disk, enmassed by the disk material to as high as $\sim 10^2$ $M_\odot$ and evolve on their respective main-sequence timescale leading to Type II SNe. For the case of SDSS 0956+5128 a single core collapse supernova with such initial mass would not be able to explain the observed BLR offsets. Although $\sim 10^2 - 10^3$ such SNe simultaneously would, this could hardly be a plausible scenario. In addition, it was argued that the stars might more likely be destroyed by the release of energy for circularization of their orbit in the accretion disk, as a very limited set of conditions for entry must be met to stay bound (Goodman & Tan, 2004).

On the other hand, Goodman & Tan (2004) considered in situ star formation and growth of massive stars. The main argument that stars can and possibly should form in BH accretion disks was that starting from a distance of $\sim 10^3\ R_S$, where R_S is the Schwarzschild radius, the disks are dominated by self-gravity and are expected to fragment via local dynamical instability. Goodman & Tan (2004) considered fragmentation at the exact boundary, where the radiation pressure equals the gas pressure, as at this location, any fragments would be well-separated and therefore likely to grow via accretion of the surrounding gas. The authors showed that given the strong accretion in the disk, the star is more likely to grow than fragment.

The properties of the protostar would be defined by the instability. As mentioned previously, the initial overdensity masses could reach anywhere in the range $10^2 - 10^7 M_\odot$ and are likely to grow by further accretion. The mass growth continues until the gap roughly of the size of the protostar's Roche lobe is cleared in the accretion disk. Finally, the material in the Roche lobe would contract until the star reaches the main sequence. Such stars are likely to be supported by radiation pressure and experience significant mass loss, although the levels are not known for the very high masses over $10^2\ M_\odot$.

In the theoretical framework of Goodman & Tan (2004), the mass of a protostar in a disk of $10^{8.6}\ M_\odot$ SMBH is expected to be $\sim 10^5 M_\odot$, if it forms at the edge of the low self-gravity of the disk. The likely outcome of the SNe of stars with mass $> 10^2\ M_\odot$ is a complete collapse to a BH (Fryer et al., 2001), although an instability from e^+e^- pair production may occur that would convert all of the stellar mass to ejecta at explosion. Therefore the scenario in which a star with an initial mass $10^5\ M_\odot$ evolves into a less massive $\sim 10^4\ M_\odot$ star by mass loss and causes a pair-instability supernova that ejects all of the material in an explosion would be consistent with the observation in SDSS 0956+5128.

Following Goodman & Tan (2004), if the star is stable on the main sequence, it can be expected to migrate inwards, preserving the disk gap, and reach the tidal radius on the time ($\sim 10^5$ yr) shorter than the main sequence time ($\sim 10^6$ yr). It would be of particular interest here to know whether the star is expected to disintegrate once on the main sequence or if it survives for some parameters. Future numerical simulations of such processes would be of particular interest to answer these questions.

If star formation in accretion disks is common, how frequently would an SDSS 0956+5128-like event occur? Goodman & Tan (2004) estimate that if star formation in a QSO happens at a rate of one per viscous time, then given the approximate number density of QSOs at redshifts $0.5 < z < 1.5$, 10^{-5} massive stars per QSO per year should form, for a total of a few stars per year in a survey the size of SDSS.

However, most of those stars will not produce an observable supernova. Goodman & Tan (2004) argued that sinking into the SMBH is the typical outcome. Fresh, hydrogen-rich material from the accretion disk can mix into the convective stellar core, so that the main sequence lifetime becomes longer than the timescale for reaching the event horizon. Thus, their deaths would not be observable.

Perhaps if the accretion disk becomes sparse towards either near the Eddington luminosity or towards the end of a quasar's lifetime, there might be just a high enough density to form a massive star, yet not enough additional material to sustain that star until it reaches the event horizon. The resulting supernovae might even provide a turnoff mechanism, so that quasars die with a bang rather than with a whimper. As SDSS 0956+5128 lies at $z = 0.7$, below which relatively few quasars are observed, it is likely to turn off in the near future. It is therefore plausible to associate the extreme features of SDSS 0956+5128 with a short-lived turnoff mechanism. If such a process lasts for $\sim 10^3 - 10^4$ yr (based on the timeline of the shock wave in Fig. 3.4), finding one example in all of SDSS is plausible.

3.6 Discussion

It is argued here that none of the common and less so mechanisms, except for the shock wave, are likely to produce a spectroscopic signature observed in the BLR of SDSS 0956+5128. The scenarios that involve special morphology, alignment of multiple objects, radiation output of the QSO or SMBH mergers each have at least one sharp inconsistency with the evidence (see Section 3.4). Instead, this work proposes the idea of shock waves to explain the observed spectroscopic offsets. The toy model requires the tuning of only the BLR density parameter to match the velocity offsets in SDSS 0956+5128, as well as the location of Mg II line.

To support or reject the idea of the supernova shock causing the outflow in the BLR it is necessary to collect more observational evidence. Below is the list with a couple of possibilities.

- *Other offset lines?* The shock mechanism predicts that there must be a continuum of velocity components in the second phase of the shocked BLR (see Section 3.5 and Figure 3.4), as opposed to only one that was observed. Although the most prominent BEL in the second phase (Mg II) was already observed, lower-ionization lines in the NUV, like O I, Si II or C II are not detected in the HST spectrum here. Instead, they could be targeted with higher signal-to-noise spectra. Additionally, Fe Kα line in the X-rays would be expected to have the high velocity offset of 4100 km s^{-1}, as the other lines of that velocity component. Probably, the direction of the offset and the line symmetry would depend on the position relative to the potential SN explosion site in the accretion disk. If any of these lines are inconsistent with the prediction, this will rule out the hypothesis.
- *Traces of neutrinos and electromagnetic emission.* From another perspective, SN shocks act as neutrino production sites, through pion decays as a result of proton-proton interactions. It was suggested that the diffuse neutrino background may be substantially contributed to by AGN stellar explosions (Zhu et al., 2021). In order to detect these events, it was shown (though for much less massive stars) that short bursts in the diffuse neutrino background and the ensuing lasting electromagnetic emission can be used. Therefore, such signature may be used to search for potential candidates for follow-up observations or for testing models of neutrino and electromagnetic emission produced by energetic stellar explosions.

After all, the shock hypothesis here is an analytical solution based on the simple assumptions of shock-medium interaction and lacks a more detailed insight. Therefore, numerical modeling of the involved processes would be required to test the idea more robustly. Below are the suggestions for possible experiments and predictions.

- *Downstream velocity as function of time.* The BLR gas with different offsets starts mixing in the *snowplow* phase altering the velocity of the BLR outflow. If one can calculate the outflow velocity of every one of the observed emission lines as a function of time, it will be possible to predict the blueshift that the lines should have at a time of a possible future observation. Besides, it will also be possible to predict how the strength of the broad line emission will change over time, as the emitting gas moves away from its ionization zone. Additionally, the density of the BLR assumed here corresponds to a rather conservative lower limit and it has a uniform radial profile, which can be tested by modeling the broad line emission observed in SDSS 0956+5128.

- *Numerical simulation of stars in a strong gravitational potential.* One of the main problems in the shock hypothesis is what caused it. The only possibility to create a shock wave of the required energy known to us is a potential supernova. If the outflow profile in SDSS 0956+5128 is a signature of an SN (see Section 3.5), then the mass of the ejecta is estimated to be $\sim 10^4\ M_\odot$ and the kinetic energy is $E_k \sim 10^{55}$ erg. It is unclear whether stars can be "safely" delivered to accretion disks of SMBHs and then grow to such extent by accretion, but there exist theoretical models that predict formation of such supermassive stars in these extreme environments in the first place. To shed more light on the possibility of the supermassive stars leading to SNe shocks, numerical simulations of their formation and evolution are required. In this regard, the most important questions are: (1) whether a stellar explosion is close to being spherical in a strong gravitational field (to offset a BLR entirely rather than in the plane of the disk); (2) whether a proto-star can remain stable to reach and stay on the stellar main sequence; (3) if the star's main sequence lifetime is shorter than the timescale for spiralling down into the SMBH; (4) if the "spiralling down" timescale wins, whether it may be reversed in special cases when the QSO shuts down accretion and turns off.

Solving the problem posed by SDSS 0956+5128 may shed new light on the evolution of quasars and formation of massive stars in extreme environments. There is a potential for studying the physics of star formation and evolution in QSO disks, as potentially a few stars per year may form in an SDSS-sized survey of quasars. In addition, if stellar explosions are shown to be possible, this may improve the understanding of extreme stellar evolution and BLR outflows. However, it is less clear how frequent supernovae may be. If the offset emission of the BLR in SDSS 0956+5128 is the result of an SN, it is likely only one such event in the SDSS, as no similar candidates have been reported. Although, new multi-line observations of the evolved quasars with strong outflows may reveal more of these objects in the future. On the other hand, it is believed that they are not observable and more likely to cross the event horizon before they explode, because their lifetimes are prolonged by the freshly accreted gas. Although, this may not be the case in sparse accretion disks of the old quasars, where little gas may not be enough to support the stars before sinking into the SMBH. Therefore, if the occurrence rate is low because the SN-induced velocity offsets of BLRs in old quasars are transient on some timescale, then it is possible that SNe are more frequent and could also play an important role in turning off QSOs.

Chapter 4

Current Work and Future Perspectives

This chapter contains several materials from the following journal article:

> **“Templates for Fitting Photometry of Ultra-high-redshift Galaxies”**
>
> Published in The Astrophysical Journal Letters (ApJL), Volume 951, Issue 2, id.L40, 7 pages, July 2023.
>
> Authors: Charles L. Steinhardt, Vasily Kokorev, Vadim Rusakov, Ethan Garcia, Albert Sneppen.

4.1 Variations of the Stellar Initial Mass Function

Templates for High-redshift Galaxy Candidates

> This section contains Table 3 and Figure 3 from Steinhardt et al. (2023a). The author of the thesis produced the table and constructed galaxy templates as part of the publication.

The work presented in Chapter 2 suggests that star-forming galaxies exhibit IMF-driven mass-to-light variations across $0 < z < 2$. It shows that even at this redshift range the changes in photometrically inferred stellar mass of star-forming galaxies can substantially modify the stellar mass functions. If the formalism of temperature-dependent IMF in Jermyn et al. (2018) is accurate, the changes in the temperature of the star-forming gas at higher redshift may produce much stronger effects. This becomes particularly relevant for the luminous galaxies that are found to have elevated stellar-to-halo mass ratios in Davidzon et al. (2017); Weaver et al. (2023) and in the most recent JWST studies (Boylan-Kolchin, 2023). Is their stellar mass a result of an increased star formation efficiency or an overestimation due to a more top-heavy IMF at high redshift?

With the goal of testing whether the potential changes in the IMF could explain the excessive masses alone, the work of Steinhardt et al. (2023a) modelled some of these extraordinary galaxies using new galaxy templates. The study produced a set of galaxy templates using `FSPS` (Conroy & Gunn, 2010) that assume an IMF tied to the temperature of the cosmic microwave background (CMB). As the gas in galaxies may be heated significantly above the CMB by stellar feedback (e.g., by cosmic rays), this assumption represented a lower limit on potential IMF changes. The final templates also include adjustments for the strength of nebular emission lines, which are found to have higher equivalent widths at $z \gtrsim 8$ (details are in Table 4.1).

It was found that the combined effect of the IMF and nebular lines can reduce inferred stellar mass by as much as a factor of ~ 50 for the sample of luminous galaxies, with the IMF alone probably contributing up to a factor of 10 reduction in mass (Figure 4.1). Although the nature of the stellar populations in these galaxies has not been established yet, it is clear that systematic uncertainties due to the IMF alone can reduce the statistical significance of the possible tension with the predicted star formation efficiency.

Table 4.1: Properties of the stellar populations of the 6 new FSPS templates for `EAZY` at $T_g = 45$ K and 60 K. The templates all have young stellar populations with ages between 0.05 and 0.20 Gyr for 45 K and between 0.1 and 0.5 Gyr for 60 K. The low extinction and metallicity are expected to be typical of ultra-high-redshift galaxies. Because of the strong emission lines present in early NIRSpec observations (Carnall et al., 2023a), two templates are included with strongly enhanced EW(Hβ + [O III]λ5007) with respect to the standard FSPS setting of $\sim 274\ \mathring{A}$.

ID	t_{45} (Gyr)	t_{60} (Gyr)	$A_{V,45,60}$	$Z_{45,60}$	Neb. Em.
1	0.1	0.05	0.005	0.0012	1x (std.)
2	0.1	0.05	0.5	0.0012	5x
3	0.3	0.1	0.005	0.0012	1x (std.)
4	0.3	0.1	0.5	0.0012	1x (std.)
5	0.5	0.2	0.005	0.0012	1x (std.)
6	0.5	0.2	0.5	0.0012	5x

Future Perspectives

The work demonstrated in Chapter 2 shows that well-sampled SEDs of galaxies possibly hold information about IMF-driven mass-to-light variations, although it is hard to keep track of all systematic effects using UV-to-NIR photometry alone. From the mock tests of Sneppen et al. (2022) this information appears to be most cleanly available for the model galaxies that have the most top-heavy IMF. In the work here, these galaxies have been established as the youngest and most actively star-forming population with distinct morphology. Intuitively, this makes sense as these galaxies are expected to have the shortest star formation and metallicity evolution history which may not have had enough time to erase most of the information about their earliest stellar populations. Still, this work provides only statistical and phenomenological evidence, while lacking some physical insights.

Therefore, it is going to be extremely valuable to look for independent evidence of IMF variations in the galaxies studied here either in FIR and sub-mm wavelengths or in the optical spectroscopic features. For example, if there are more massive stars in galaxies with a top-heavy IMF, they can be expected to heat up the dust in H II regions accordingly. This effect could shift the modified black body peak positions to shorter wavelengths, than in some control sample of typical galaxies. Although it is possible that these galaxies have little dust, which in that case may further support that they are in the early evolutionary phase.

Furthermore, if galaxies have a top-heavy IMF in the early stages of

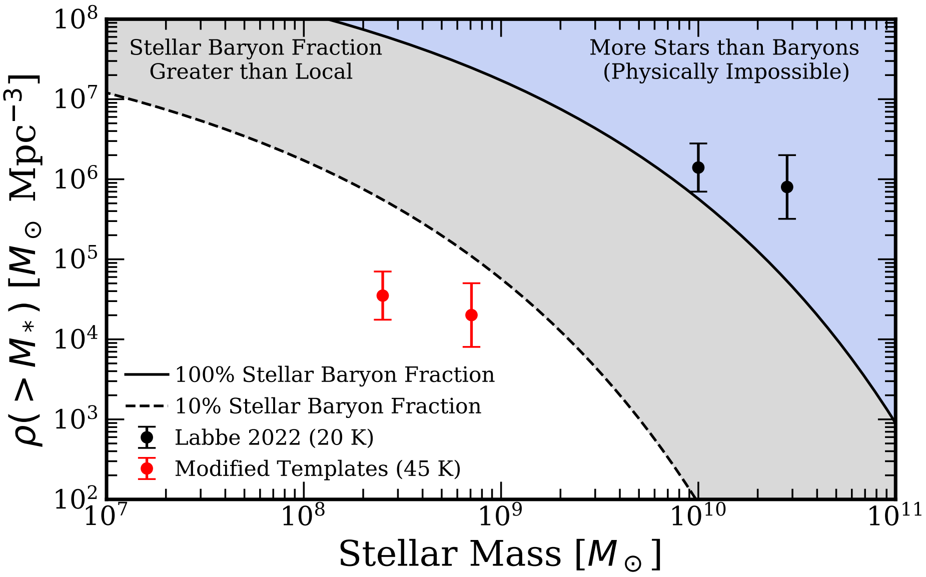

Figure 4.1: Change in the stellar mass and stellar mass density of two $z = 10$ galaxy candidates (in the Early Release Science data) associated with the change in the assumed IMF and stronger nebular emission lines in Steinhardt et al. (2023a). The IMF shape is extrapolated using the CMB temperature at that redshift as the lower limit on the temperature of the star-forming gas. Note, that the estimates of the stellar mass of these galaxies in Labbé et al. (2023) with the updated photometric calibrations for NIRCam and although are no longer in the "Physically Impossible" region, but still imply a higher stellar baryon fraction than locally.

their formation, this can be explained by large gas density that reduces the cooling timescale and allows to form stars quicker than the time it takes to produce stellar feedback to regulate their formation (Dekel et al., 2023). This hypothesis can be tested by studying the gas-phase conditions in a sub-sample of COSMOS galaxies. For example, the density-sensitive level populations of [O II] $\lambda\lambda 3726, 3729$ and S II $\lambda\lambda 6716, 6731$ can be used to measure the nebular gas density (Osterbrock, 1989). Finally, galaxies with similar physical properties to the top-heavy IMF sample, have been detected in SDSS surveys and called "green pea" galaxies because of their strong nebular emission in the "green" SDSS bands and small physical sizes (Cardamone et al., 2009). In this case, evidence of high electron temperature of the gas from e.g., the temperature-sensitive [O I] $\lambda\lambda 5577, 6300, 6364$, [N II] $\lambda\lambda 5755, 6548, 6584$ and [O III] $\lambda\lambda 4364, 4959, 5007$ lines could be another useful indicator of distinct state of the ISM.

Finally, most direct information about distinct stellar populations may come from observations with JWST/NIRSpec at high redshift, where the conditions of the ISM may be extreme in all galaxies. It is established from stellar evolution models that intermediate and high-mass stars dominate production of different chemical elements – for example, nitrogen and oxygen, respectively (Henry et al., 2000; Pettini et al., 2008). Given that the lifetime of these stars is different, the most massive ones have a head-start to disperse "primary" oxygen before the next generation intermediate-mass stars (with nitrogen-rich yields) start to produce nitrogen ∼250 Myr after (Henry et al., 2000). If at this stage, when the massive stars dominate, the $[N/O]$ abundance is lower than in the local universe, this may indicate a top-heavy IMF. If on the other hand, the intermediate-mass stars start to produce an excessive $[N/O]$, this can indicate an intermediate-heavy IMF. So far there has been no strong evidence of such deviations from extragalactic H II regions or DLA systems at $2 < z < 4$. However, at higher redshift, where the relevant stellar timescales represent a considerable fraction of the star formation history of galaxies, such deviations may not be washed-away yet (Pettini et al., 2000, 2008). In fact, recent studies find over-abundance of nitrogen at $z > 10$ (Cameron et al., 2023a), which can motivate wider search campaigns for similar chemical signatures and their physical origin in the near future.

4.2 Star Formation in Extreme Environments

Chapter 3 presents a new interpretation of a unique observational signature in a quasar SDSS 0956+5128 and considers the possibility of star formation in the gas medium surrounding supermassive black holes. Such events may be the laboratories for studying extreme star formation, if confirmed. Moreover, massive star formation in active galactic nuclei can be an important mechanism for explaining the evolution of the early supermassive black holes, which are currently found to grow very rapidly and reach the large relative mass of $M_{BH}/M^{\star} \sim 0.1$ early on (e.g., Maiolino et al., 2023).

So far, there are only theoretical arguments showing that star formation in accretion discs is possible (Goodman & Tan, 2004). If it is possible, the massive stars have to be universally common and have to satisfy a number of criteria to produce spectroscopic features observed in SDSS 0956+5128: (a) the main sequence lifetime needs to become shorter than the time for spiralling into the SMBH; (b) the explosion has to have approximately spherical symmetry. Testing these conditions requires numerical modelling in the future work. According to the cosmic star formation history, a few stars per year are expected to form in an SDSS-sized quasar survey. If point (a) is satisfied for quasars that are old and about to turn off, this can explain possibly lower SN rates. Therefore, a search for similar objects can follow the quenching history of quasars in the low-redshift universe.

Any alternative explanations of such objects, such recoiling SMBH, can benefit from larger samples of candidates for studying their population properties. The reason for the lack of detected candidates is possibly the shortage of spectroscopic data – few objects have similarly wide wavelength coverage as SDSS 0956+5128 in this case, which is the key to differentiating it from a typical quasar.

4.3 Conclusion

In the past, many discoveries in extragalactic astrophysics followed after technological advancements: from Edwin Hubble's censuses of "extragalactic nebulae" with the largest optical telescopes at the time, through the revolutions in cosmology and large scale structure driven by the microwave anisotropy observatories, recently largest and most sensitive optical Hubble Space Telescope and to the direct images of massive black holes and exquisite aspects of star formation and chemical evolution by the Atacama Large Millimetre Array in the sub-millimetre wavelengths. Now, with the help of James Webb Space Telescope, it has just become possible to probe the earliest and possibly most extreme environments in the history of galaxies and the universe.

The work presented here has been motivated by the inconsistencies that started to arise between the predictions of galaxy assembly with the best cosmological theory and the observations in the first 1 to 1.5 billion years of galaxy evolution. Already in the deep Hubble fields the most massive galaxies appear to grow larger than expected from their dark matter halos at $z \sim 6$ (Steinhardt et al., 2016; Davidzon et al., 2017). Observational and modelling improvements seem to help to reconcile the disagreement (Weaver et al., 2023), but the deeper observations with the James Webb continue to bring it back (Harikane et al., 2023; Finkelstein et al., 2023). Biggest galaxies are too luminous than expected from simulations and extrapolated models and this likely prompts further revisions of the galaxy models.

Open possibilities for revisions in the models of galaxy-wide star formation include changes to the assumed ratio between the total stellar mass and light, such as that determined by the stellar initial mass function (IMF). So far, the evidence of IMF variations has come from detailed case studies of old and young stellar systems in the local universe and early-type galaxies (e.g., Conroy & van Dokkum, 2012; Hallakoun & Maoz, 2021; Freundlich & Maoz, 2021; van Dokkum et al., 2024), but lacked the evidence of the possible systematic IMF variations. Chapter 2 approaches this problem from the galaxy population perspective. Based on a large sample of photometric measurements, it presents the evidence that the IMF may exhibit two systematic behaviours in different galaxies: (1) an IMF-driven mass to-light ratio decreases from $z \sim 0$ to $z \sim 2$ in star-forming galaxies (i.e., the IMF becomes more top-heavy); and (2) the mass-to-light ratio in quiescent galaxies is at least as large as in the Milky Way (i.e., the IMF is at least as bottom-heavy). As a result, the inferred stellar masses and star formation rates of actively star-forming galaxies change by factors of $\sim 1.6 - 3.5$ and

$2.5 - 70.0$, respectively. Besides, the IMF may provide another dimension to study star formation as a key process driving galaxy evolution. Later, it is shown that extrapolations of these findings can explain the excessive physical properties of galaxies found with the JWST.

However, it becomes clear in this work that it is extremely difficult to constrain useful information with few degrees of freedom allowed in photometric modelling. Therefore, case studies of the most well-measured objects that can help to uniquely constrain models of star formation are likely to be the most efficient strategy for validating the results here in the future. If some of the suggested tests confirm IMF variations (see Chapter 4), then the current galaxy models have to be reconsidered, especially when applied to the galaxies in the first billion years. In this regard, the work in Chapter 3 turns to one of the most extreme environments for star formation that may mimic those of the first early galaxies: active galactic nuclei.

Chapter 3 presents the latest observations of the quasar SDSS 0956+5128 at $z \sim 0.7$ with very distinct outflow features that appear to be unique in over 10^5 QSO observed in the SDSS. Apart from the cosmological redshift, the object has two distinct velocity components in the broad line region (BLR). Unlike typical outflows driven for example by accretion disk winds, the emission lines in this object do not show a decrease in the kinetic energy of the outflow as a function of distance (Yu et al., 2021). It is argued that such specific velocity profile is consistent with the scenario where supernova shocks waves traverse the BLR. It is going to be very challenging to prove the occurrence of such events, and possibly one of the best future directions is numerical simulations. This could form the basis for future studies of star formation in extreme physical conditions, as well as help to understand the growth of supermassive black holes in the early galaxies.

Bibliography

Abbott, B. P., Abbott, R., Abbott, T. D., et al. 2017, , 551, 85, doi: 10.1038/nature24471

Abramson, L. E., Gladders, M. D., Dressler, A., et al. 2016, , 832, 7, doi: 10.3847/0004-637X/832/1/7

Abramson, L. E., Kelson, D. D., Dressler, A., et al. 2014, , 785, L36, doi: 10.1088/2041-8205/785/2/L36

Adams, F. C., & Fatuzzo, M. 1996, , 464, 256, doi: 10.1086/177318

Adams, N. J., Bowler, R. A. A., Jarvis, M. J., Häußler, B., & Lagos, C. D. P. 2021, , 506, 4933, doi: 10.1093/mnras/stab1956

Adams, N. J., Conselice, C. J., Austin, D., et al. 2023a, arXiv e-prints, arXiv:2304.13721, doi: 10.48550/arXiv.2304.13721

Adams, N. J., Conselice, C. J., Ferreira, L., et al. 2023b, , 518, 4755, doi: 10.1093/mnras/stac3347

Anders, P., & Fritze-v. Alvensleben, U. 2003, , 401, 1063, doi: 10.1051/0004-6361:20030151

Anderson, J. 2016, Empirical Models for the WFC3/IR PSF, Space Telescope WFC Instrument Science Report: 2016wfc..rept...12A

Anderson, J., & King, I. R. 2000, , 112, 1360, doi: 10.1086/316632

Andrews, B. H., & Martini, P. 2013, , 765, 140, doi: 10.1088/0004-637X/765/2/140

Antonucci, R. 1993, , 31, 473, doi: 10.1146/annurev.aa.31.090193.002353

Antonucci, R. R. J., & Miller, J. S. 1985, , 297, 621, doi: 10.1086/163559

Arnouts, S., Schiminovich, D., Ilbert, O., et al. 2005, , 619, L43, doi: 10.1086/426733

Arnouts, S., Le Floc'h, E., Chevallard, J., et al. 2013, , 558, A67, doi: 10.1051/0004-6361/201321768

Arrabal Haro, P., Dickinson, M., Finkelstein, S. L., et al. 2023, , 951, L22, doi: 10.3847/2041-8213/acdd54

Artymowicz, P., Lin, D. N. C., & Wampler, E. J. 1993, The Astrophysical Journal, 409, 592, doi: 10.1086/172690

Atek, H., Shuntov, M., Furtak, L. J., et al. 2023a, , 519, 1201, doi: 10.1093/mnras/stac3144

Atek, H., Labbé, I., Furtak, L. J., et al. 2023b, arXiv e-prints, arXiv:2308.08540, doi: 10.48550/arXiv.2308.08540

Bailey, J., Axon, D. J., Hough, J. H., et al. 1988, , 234, 899, doi: 10.1093/mnras/234.4.899

Baker, J. G., Boggs, W. D., Centrella, J., et al. 2008, , 682, L29, doi: 10.1086/590927

Baldry, I. K., Glazebrook, K., & Driver, S. P. 2008, , 388, 945, doi: 10.1111/j.1365-2966.2008.13348.x

Barro, G., Faber, S. M., Koo, D. C., et al. 2017, , 840, 47, doi: 10.3847/1538-4357/aa6b05

Bartko, H., Martins, F., Trippe, S., et al. 2010, , 708, 834, doi: 10.1088/0004-637X/708/1/834

Bastian, N., Covey, K. R., & Meyer, M. R. 2010, , 48, 339, doi: 10.1146/annurev-astro-082708-101642

Bate, M. R., & Bonnell, I. A. 2005, , 356, 1201, doi: 10.1111/j.1365-2966.2004.08593.x

Beckwith, S. V. W., Stiavelli, M., Koekemoer, A. M., et al. 2006, , 132, 1729, doi: 10.1086/507302

Behroozi, P. S., Wechsler, R. H., & Conroy, C. 2013a, , 762, L31, doi: 10.1088/2041-8205/762/2/L31

—. 2013b, , 770, 57, doi: 10.1088/0004-637X/770/1/57

Bekki, K., & Tsujimoto, T. 2023, , 526, L26, doi: 10.1093/mnrasl/slad108

Bell, E. F., McIntosh, D. H., Katz, N., & Weinberg, M. D. 2003, , 149, 289, doi: 10.1086/378847

Bentz, M. C., Denney, K. D., Grier, C. J., et al. 2013, , 767, 149, doi: 10.1088/0004-637X/767/2/149

Bershady, M. A., Jangren, A., & Conselice, C. J. 2000, , 119, 2645, doi: 10.1086/301386

Béthermin, M., Daddi, E., Magdis, G., et al. 2015, , 573, A113, doi: 10.1051/0004-6361/201425031

Bhatawdekar, R., & Conselice, C. J. 2021, , 909, 144, doi: 10.3847/1538-4357/abdd3f

Blecha, L., Civano, F., Elvis, M., & Loeb, A. 2013, , 428, 1341, doi: 10.1093/mnras/sts114

Bonning, E. W., Shields, G. A., & Salviander, S. 2007, , 666, L13, doi: 10.1086/521674

Bottorff, M. C., Ferland, G. J., & Straley, J. P. 2006, , 118, 1176, doi: 10.1086/506974

Bouwens, R. J., Illingworth, G. D., Oesch, P. A., et al. 2010, , 709, L133, doi: 10.1088/2041-8205/709/2/L133

—. 2012, , 754, 83, doi: 10.1088/0004-637X/754/2/83

Bouwens, R. J., Oesch, P. A., Stefanon, M., et al. 2021, , 162, 47, doi: 10.3847/1538-3881/abf83e

Bowler, R. A. A., Jarvis, M. J., Dunlop, J. S., et al. 2020, , 493, 2059, doi: 10.1093/mnras/staa313

Bowler, R. A. A., Dunlop, J. S., McLure, R. J., et al. 2012, , 426, 2772, doi: 10.1111/j.1365-2966.2012.21904.x

Boyer, M. L., Anderson, J., Gennaro, M., et al. 2022, Research Notes of the American Astronomical Society, 6, 191, doi: 10.3847/2515-5172/ac923a

Boylan-Kolchin, M. 2023, Nature Astronomy, doi: 10.1038/s41550-023-01937-7

Bradley, L., Sipőcz, B., Robitaille, T., et al. 2020, Zenodo, doi: `10.5281/zenodo.4044744`

Brammer, G. 2021, gbrammer/eazy-py: Tagged release 2021, 0.5.2, Zenodo, Zenodo, doi: `10.5281/zenodo.5012705`

Brammer, G., & Matharu, J. 2021, gbrammer/grizli: Release 2021, 1.3.2, Zenodo, Zenodo, doi: `10.5281/zenodo.1146904`

Brammer, G. B., van Dokkum, P. G., & Coppi, P. 2008, , 686, 1503, doi: `10.1086/591786`

Brinchmann, J., Charlot, S., White, S. D. M., et al. 2004, , 351, 1151, doi: `10.1111/j.1365-2966.2004.07881.x`

Bromm, V., & Larson, R. B. 2004, , 42, 79, doi: `10.1146/annurev.astro.42.053102.134034`

Brotherton, M. S., Wills, B. J., Steidel, C. C., & Sargent, W. L. W. 1994, , 423, 131, doi: `10.1086/173794`

Bruzual, G., & Charlot, S. 2003, , 344, 1000, doi: `10.1046/j.1365-8711.2003.06897.x`

Bruzual A., G., & Charlot, S. 1993, , 405, 538, doi: `10.1086/172385`

Bullock, J. S., & Boylan-Kolchin, M. 2017, , 55, 343, doi: `10.1146/annurev-astro-091916-055313`

Bunker, A. J., Saxena, A., Cameron, A. J., et al. 2023, , 677, A88, doi: `10.1051/0004-6361/202346159`

Cameron, A. J., Katz, H., Rey, M. P., & Saxena, A. 2023a, , 523, 3516, doi: `10.1093/mnras/stad1579`

Cameron, A. J., Katz, H., Witten, C., et al. 2023b, arXiv e-prints, arXiv:2311.02051, doi: `10.48550/arXiv.2311.02051`

Campanelli, M., Lousto, C., Zlochower, Y., & Merritt, D. 2007a, , 659, L5, doi: `10.1086/516712`

Campanelli, M., Lousto, C. O., Zlochower, Y., & Merritt, D. 2007b, , 98, 231102, doi: `10.1103/PhysRevLett.98.231102`

Capak, P., Aussel, H., Ajiki, M., et al. 2007, The Astrophysical Journal Supplement Series, 172, 99, doi: `10.1086/519081`

Cappellari, M., McDermid, R. M., Alatalo, K., et al. 2012, , 484, 485, doi: 10.1038/nature10972

Caputi, K. I., Ilbert, O., Laigle, C., et al. 2015, , 810, 73, doi: 10.1088/0004-637X/810/1/73

Cardamone, C., Schawinski, K., Sarzi, M., et al. 2009, , 399, 1191, doi: 10.1111/j.1365-2966.2009.15383.x

Carnall, A. C., Begley, R., McLeod, D. J., et al. 2023a, , 518, L45, doi: 10.1093/mnrasl/slac136

Carnall, A. C., McLure, R. J., Dunlop, J. S., et al. 2023b, , 619, 716, doi: 10.1038/s41586-023-06158-6

Casey, C. M., Zavala, J. A., Spilker, J., et al. 2018, , 862, 77, doi: 10.3847/1538-4357/aac82d

Castellano, M., Fontana, A., Paris, D., et al. 2010a, , 524, A28, doi: 10.1051/0004-6361/201015195

Castellano, M., Fontana, A., Boutsia, K., et al. 2010b, , 511, A20, doi: 10.1051/0004-6361/200913300

Castellano, M., Fontana, A., Treu, T., et al. 2022, , 938, L15, doi: 10.3847/2041-8213/ac94d0

Chabrier, G. 2003, , 115, 763, doi: 10.1086/376392

Chapman, S. C., Blain, A. W., Smail, I., & Ivison, R. J. 2005, , 622, 772, doi: 10.1086/428082

Chary, R., & Elbaz, D. 2001, , 556, 562, doi: 10.1086/321609

Chen, K., & Halpern, J. P. 1989, The Astrophysical Journal, 344, 115, doi: 10.1086/167782

Chen, Y., Mo, H. J., & Wang, K. 2023, arXiv e-prints, arXiv:2304.13890, doi: 10.48550/arXiv.2304.13890

Chiaberge, M., Ely, J. C., Meyer, E. T., et al. 2017, , 600, A57, doi: 10.1051/0004-6361/201629522

Civano, F., Elvis, M., Lanzuisi, G., et al. 2010, , 717, 209, doi: 10.1088/0004-637X/717/1/209

—. 2012, , 752, 49, doi: 10.1088/0004-637X/752/1/49

Cole, S., Norberg, P., Baugh, C. M., et al. 2001, , 326, 255, doi: 10.1046/j.1365-8711.2001.04591.x

Colless, M., Dalton, G., Maddox, S., et al. 2001, , 328, 1039, doi: 10.1046/j.1365-8711.2001.04902.x

Connolly, A. J., Szalay, A. S., Dickinson, M., SubbaRao, M. U., & Brunner, R. J. 1997, , 486, L11, doi: 10.1086/310829

Conroy, C. 2013a, , 51, 393, doi: 10.1146/annurev-astro-082812-141017

—. 2013b, , 51, 393, doi: 10.1146/annurev-astro-082812-141017

Conroy, C., & Gunn, J. E. 2010, , 712, 833, doi: 10.1088/0004-637X/712/2/833

Conroy, C., Gunn, J. E., & White, M. 2009, , 699, 486, doi: 10.1088/0004-637X/699/1/486

Conroy, C., & van Dokkum, P. G. 2012, , 760, 71, doi: 10.1088/0004-637X/760/1/71

Conroy, C., van Dokkum, P. G., & Villaume, A. 2017, , 837, 166, doi: 10.3847/1538-4357/aa6190

Conselice, C. J. 2014, , 52, 291, doi: 10.1146/annurev-astro-081913-040037

Conselice, C. J., Mundy, C. J., Ferreira, L., & Duncan, K. 2022, , 940, 168, doi: 10.3847/1538-4357/ac9b1a

Corbin, M. R. 1990, , 357, 346, doi: 10.1086/168925

Cortzen, I., Magdis, G. E., Valentino, F., et al. 2020, , 634, L14, doi: 10.1051/0004-6361/201937217

Cowie, L. L., Songaila, A., Hu, E. M., & Cohen, J. G. 1996, , 112, 839, doi: 10.1086/118058

Cresci, G., & Maiolino, R. 2018, Nature Astronomy, 2, 179, doi: 10.1038/s41550-018-0404-5

Cullen, F., McLure, R. J., McLeod, D. J., et al. 2023, , 520, 14, doi: 10.1093/mnras/stad073

Curti, M., Mannucci, F., Cresci, G., & Maiolino, R. 2020, , 491, 944, doi: 10.1093/mnras/stz2910

Curtis-Lake, E., Carniani, S., Cameron, A., et al. 2023, Nature Astronomy, 7, 622, doi: 10.1038/s41550-023-01918-w

Czerny, B., Olejak, A., Rałowski, M., et al. 2019, , 880, 46, doi: 10.3847/1538-4357/ab2913

da Cunha, E., Charlot, S., & Elbaz, D. 2008, , 388, 1595, doi: 10.1111/j.1365-2966.2008.13535.x

Daddi, E., Dickinson, M., Morrison, G., et al. 2007, , 670, 156, doi: 10.1086/521818

Dalla Bontà, E., Peterson, B. M., Bentz, M. C., et al. 2020, , 903, 112, doi: 10.3847/1538-4357/abbc1c

Davé, R., Anglés-Alcázar, D., Narayanan, D., et al. 2019, , 486, 2827, doi: 10.1093/mnras/stz937

Davidzon, I., Ilbert, O., Laigle, C., et al. 2017, , 605, A70, doi: 10.1051/0004-6361/201730419

Davis, S. W., Woo, J.-H., & Blaes, O. M. 2007, , 668, 682, doi: 10.1086/521393

De Rossi, M. E., Bower, R. G., Font, A. S., & Schaye, T. 2018, Boletin de la Asociacion Argentina de Astronomia La Plata Argentina, 60, 121, doi: 10.48550/arXiv.1805.06119

de Swart, J. G., Bertone, G., & van Dongen, J. 2017, Nature Astronomy, 1, 0059, doi: 10.1038/s41550-017-0059

de Vaucouleurs, G. 1959, Handbuch der Physik, 53, 275, doi: 10.1007/978-3-642-45932-0_7

Dekel, A., Sarkar, K. C., Birnboim, Y., Mandelker, N., & Li, Z. 2023, , 523, 3201, doi: 10.1093/mnras/stad1557

Dietrich, M., Peterson, B. M., Albrecht, P., et al. 1998, The Astrophysical Journal Supplement Series, 115, 185, doi: 10.1086/313085

Donnan, C. T., McLeod, D. J., Dunlop, J. S., et al. 2023, , 518, 6011, doi: 10.1093/mnras/stac3472

Driver, S. P., Hill, D. T., Kelvin, L. S., et al. 2011, , 413, 971, doi: 10.1111/j.1365-2966.2010.18188.x

Drory, N., & Alvarez, M. 2008, , 680, 41, doi: 10.1086/588006

Du, P., Zhang, Z.-X., Wang, K., et al. 2018, , 856, 6, doi: 10.3847/1538-4357/aaae6b

Dunlop, J. S., McLure, R. J., Robertson, B. E., et al. 2012, , 420, 901, doi: 10.1111/j.1365-2966.2011.20102.x

Dunlop, J. S., Rogers, A. B., McLure, R. J., et al. 2013, , 432, 3520, doi: 10.1093/mnras/stt702

Eddington, A. S. 1913, , 73, 359, doi: 10.1093/mnras/73.5.359

Elbaz, D., Daddi, E., Le Borgne, D., et al. 2007, , 468, 33, doi: 10.1051/0004-6361:20077525

Elbaz, D., Dickinson, M., Hwang, H. S., et al. 2011, , 533, A119, doi: 10.1051/0004-6361/201117239

Elitzur, M., & Shlosman, I. 2006, , 648, L101, doi: 10.1086/508158

Elmegreen, B. G. 2006, , 648, 572, doi: 10.1086/505785

Emmering, R. T., Blandford, R. D., & Shlosman, I. 1992, , 385, 460, doi: 10.1086/170955

Engler, C., Lisker, T., & Pillepich, A. 2018, Research Notes of the American Astronomical Society, 2, 6, doi: 10.3847/2515-5172/aabcce

Eracleous, M., Boroson, T. A., Halpern, J. P., & Liu, J. 2012, , 201, 23, doi: 10.1088/0067-0049/201/2/23

Eracleous, M., Livio, M., Halpern, J. P., & Storchi-Bergmann, T. 1995, The Astrophysical Journal, 438, 610, doi: 10.1086/175104

Erwin, P. 2015, , 799, 226, doi: 10.1088/0004-637X/799/2/226

Espey, B. R., Carswell, R. F., Bailey, J. A., Smith, M. G., & Ward, M. J. 1989, , 342, 666, doi: 10.1086/167627

Everett, J. E. 2005, , 631, 689, doi: 10.1086/432678

Faber, S. M., & Gallagher, J. S. 1979, , 17, 135, doi: 10.1146/annurev.aa.17.090179.001031

Faber, S. M., Willmer, C. N. A., Wolf, C., et al. 2007, , 665, 265, doi: 10.1086/519294

Faisst, A. L., Capak, P. L., Davidzon, I., et al. 2016, , 822, 29, doi: 10.3847/0004-637X/822/1/29

Figer, D. F., Kim, S. S., Morris, M., et al. 1999, , 525, 750, doi: 10.1086/307937

Finkelstein, S. L., Papovich, C., Salmon, B., et al. 2012, , 756, 164, doi: 10.1088/0004-637X/756/2/164

Finkelstein, S. L., Ryan, Russell E., J., Papovich, C., et al. 2015a, , 810, 71, doi: 10.1088/0004-637X/810/1/71

Finkelstein, S. L., Song, M., Behroozi, P., et al. 2015b, , 814, 95, doi: 10.1088/0004-637X/814/2/95

Finkelstein, S. L., Bagley, M. B., Ferguson, H. C., et al. 2023, , 946, L13, doi: 10.3847/2041-8213/acade4

Fonseca Alvarez, G., Trump, J. R., Homayouni, Y., et al. 2020, , 899, 73, doi: 10.3847/1538-4357/aba001

Fontana, A., Salimbeni, S., Grazian, A., et al. 2006, , 459, 745, doi: 10.1051/0004-6361:20065475

Fontanot, F., De Lucia, G., Monaco, P., Somerville, R. S., & Santini, P. 2009, , 397, 1776, doi: 10.1111/j.1365-2966.2009.15058.x

Franceschini, A., Rodighiero, G., Cassata, P., et al. 2006, , 453, 397, doi: 10.1051/0004-6361:20054360

Francis, P. J., Hewett, P. C., Foltz, C. B., et al. 1991, , 373, 465, doi: 10.1086/170066

Freundlich, J., & Maoz, D. 2021, , 502, 5882, doi: 10.1093/mnras/stab493

Fryer, C. L., Woosley, S. E., & Heger, A. 2001, , 550, 372, doi: 10.1086/319719

Furlong, M., Bower, R. G., Theuns, T., et al. 2015, , 450, 4486, doi: 10.1093/mnras/stv852

Gallart, C., Aparicio, A., Bertelli, G., & Chiosi, C. 1996a, , 112, 1950, doi: 10.1086/118154

Gallart, C., Aparicio, A., & Vilchez, J. M. 1996b, , 112, 1928, doi: 10.1086/118153

Gallart, C., Bernard, E. J., Brook, C. B., et al. 2019, Nature Astronomy, 3, 932, doi: 10.1038/s41550-019-0829-5

Gaskell, C. M. 1982, The Astrophysical Journal, 263, 79, doi: 10.1086/160481

—. 1985, The Astrophysical Journal, 291, 112, doi: 10.1086/163045

Geha, M., Brown, T. M., Tumlinson, J., et al. 2013, , 771, 29, doi: 10.1088/0004-637X/771/1/29

Giavalisco, M., Dickinson, M., Ferguson, H. C., et al. 2004, , 600, L103, doi: 10.1086/381244

Giménez-Arteaga, C., Oesch, P. A., Brammer, G. B., et al. 2023, , 948, 126, doi: 10.3847/1538-4357/acc5ea

Goodman, J., & Tan, J. C. 2004, , 608, 108, doi: 10.1086/386360

Grazian, A., Fontana, A., Santini, P., et al. 2015, , 575, A96, doi: 10.1051/0004-6361/201424750

Grogin, N. A., Kocevski, D. D., Faber, S. M., et al. 2011, , 197, 35, doi: 10.1088/0067-0049/197/2/35

Gunawardhana, M. L. P., Hopkins, A. M., Sharp, R. G., et al. 2011, , 415, 1647, doi: 10.1111/j.1365-2966.2011.18800.x

Hallakoun, N., & Maoz, D. 2021, , 507, 398, doi: 10.1093/mnras/stab2145

Harikane, Y., Nakajima, K., Ouchi, M., et al. 2024, , 960, 56, doi: 10.3847/1538-4357/ad0b7e

Harikane, Y., Ouchi, M., Inoue, A. K., et al. 2020, , 896, 93, doi: 10.3847/1538-4357/ab94bd

Harikane, Y., Ouchi, M., Oguri, M., et al. 2023, , 265, 5, doi: 10.3847/1538-4365/acaaa9

Häring, N., & Rix, H.-W. 2004, , 604, L89, doi: 10.1086/383567

Hathi, N. P., Ryan, R. E., J., Cohen, S. H., et al. 2010, , 720, 1708, doi: 10.1088/0004-637X/720/2/1708

Healy, J., Lousto, C. O., & Zlochower, Y. 2014, , 90, 104004, doi: `10.1103/PhysRevD.90.104004`

Henry, R. B. C., Edmunds, M. G., & Köppen, J. 2000, , 541, 660, doi: `10.1086/309471`

Hewett, P. C., & Wild, V. 2010, , 405, 2302, doi: `10.1111/j.1365-2966.2010.16648.x`

Hildebrandt, H., Pielorz, J., Erben, T., et al. 2009, , 498, 725, doi: `10.1051/0004-6361/200811042`

Hodge, P. 1989, , 27, 139, doi: `10.1146/annurev.aa.27.090189.001035`

Holmberg, E. 1937, Annals of the Observatory of Lund, 6, 1

Hopkins, P. F. 2012, Monthly Notices of the Royal Astronomical Society, 423, 2037, doi: `10.1111/j.1365-2966.2012.20731.x`

Hopkins, P. F., Hernquist, L., Cox, T. J., & Kereš, D. 2008, , 175, 356, doi: `10.1086/524362`

Hubble, E. 1929, Proceedings of the National Academy of Science, 15, 168, doi: `10.1073/pnas.15.3.168`

Hubble, E. P. 1926, , 64, 321, doi: `10.1086/143018`

Huertas-Company, M., Primack, J. R., Dekel, A., et al. 2018, , 858, 114, doi: `10.3847/1538-4357/aabfed`

Hunt, L., Dayal, P., Magrini, L., & Ferrara, A. 2016a, , 463, 2002, doi: `10.1093/mnras/stw1993`

—. 2016b, , 463, 2020, doi: `10.1093/mnras/stw2091`

Hunt, L., Magrini, L., Galli, D., et al. 2012, , 427, 906, doi: `10.1111/j.1365-2966.2012.21761.x`

Ilbert, O., Capak, P., Salvato, M., et al. 2009, , 690, 1236, doi: `10.1088/0004-637X/690/2/1236`

Ilbert, O., Salvato, M., Le Floc'h, E., et al. 2010, , 709, 644, doi: `10.1088/0004-637X/709/2/644`

Ilbert, O., McCracken, H. J., Le Fèvre, O., et al. 2013, , 556, A55, doi: `10.1051/0004-6361/201321100`

Jakobsen, P., Ferruit, P., Alves de Oliveira, C., et al. 2022, , 661, A80, doi: 10.1051/0004-6361/202142663

Jappsen, A. K., Klessen, R. S., Larson, R. B., Li, Y., & Mac Low, M. M. 2005, , 435, 611, doi: 10.1051/0004-6361:20042178

Jeans, J. H. 1902, Philosophical Transactions of the Royal Society of London Series A, 199, 1, doi: 10.1098/rsta.1902.0012

Jermyn, A. S., Steinhardt, C. L., & Tout, C. A. 2018, Monthly Notices of the Royal Astronomical Society, 480, 4265, doi: 10.1093/mnras/sty2123

Juneau, S., Glazebrook, K., Crampton, D., et al. 2005, , 619, L135, doi: 10.1086/427937

Kauffmann, G., Guiderdoni, B., & White, S. D. M. 1994, , 267, 981, doi: 10.1093/mnras/267.4.981

Kaviraj, S., Laigle, C., Kimm, T., et al. 2017, , 467, 4739, doi: 10.1093/mnras/stx126

Kelson, D. D. 2014, arXiv e-prints, arXiv:1406.5191, doi: 10.48550/arXiv.1406.5191

Kennicutt, Robert C., J. 1998, , 498, 541, doi: 10.1086/305588

Kennicutt, R. C., & Evans, N. J. 2012, , 50, 531, doi: 10.1146/annurev-astro-081811-125610

Kim, S. S., Figer, D. F., Kudritzki, R. P., & Najarro, F. 2006, , 653, L113, doi: 10.1086/510529

Klessen, R. S., & Glover, S. C. O. 2023, , 61, 65, doi: 10.1146/annurev-astro-071221-053453

Koekemoer, A. M., Faber, S. M., Ferguson, H. C., et al. 2011, , 197, 36, doi: 10.1088/0067-0049/197/2/36

Korista, K. T., Alloin, D., Barr, P., et al. 1995, The Astrophysical Journal Supplement Series, 97, 285, doi: 10.1086/192144

Kriek, M., & Conroy, C. 2013, , 775, L16, doi: 10.1088/2041-8205/775/1/L16

Kroupa, P. 2001, , 322, 231, doi: 10.1046/j.1365-8711.2001.04022.x

Krumholz, M. R. 2011, , 743, 110, doi: 10.1088/0004-637X/743/2/110

Kwan, J., & Krolik, J. H. 1981, , 250, 478, doi: 10.1086/159395

Labbé, I., van Dokkum, P., Nelson, E., et al. 2023, , 616, 266, doi: 10.1038/s41586-023-05786-2

Lagos, C. d. P., Tobar, R. J., Robotham, A. S. G., et al. 2018, , 481, 3573, doi: 10.1093/mnras/sty2440

Laigle, C., McCracken, H. J., Ilbert, O., et al. 2016, The Astrophysical Journal Supplement Series, 224, 24, doi: 10.3847/0067-0049/224/2/24

Laigle, C., Davidzon, I., Ilbert, O., et al. 2019, , 486, 5104, doi: 10.1093/mnras/stz1054

Lamperti, I., Saintonge, A., De Looze, I., et al. 2019, , 489, 4389, doi: 10.1093/mnras/stz2311

Laor, A., Jannuzi, B. T., Green, R. F., & Boroson, T. A. 1997, , 489, 656, doi: 10.1086/304816

Lapiner, S., Dekel, A., Freundlich, J., et al. 2023, arXiv e-prints, arXiv:2302.12234, doi: 10.48550/arXiv.2302.12234

Larsen, S. S. 2006, arXiv e-prints, astro, doi: 10.48550/arXiv.astro-ph/0606625

Larson, R. B. 1998, , 301, 569, doi: 10.1046/j.1365-8711.1998.02045.x

—. 2005, , 359, 211, doi: 10.1111/j.1365-2966.2005.08881.x

Laursen, P. 2023, in Multiplicity of Time Scales in Complex Systems, 71, doi: 10.1007/16618_2023_71

Lawrence, A., & Elvis, M. 1982, , 256, 410, doi: 10.1086/159918

Leitherer, C., Schaerer, D., Goldader, J. D., et al. 1999, , 123, 3, doi: 10.1086/313233

Leja, J., Carnall, A. C., Johnson, B. D., Conroy, C., & Speagle, J. S. 2019, , 876, 3, doi: 10.3847/1538-4357/ab133c

Licquia, T. C., & Newman, J. A. 2015, , 806, 96, doi: 10.1088/0004-637X/806/1/96

Lilly, S. J., Carollo, C. M., Pipino, A., Renzini, A., & Peng, Y. 2013, , 772, 119, doi: 10.1088/0004-637X/772/2/119

Loeb, A. 2007, , 99, 041103, doi: 10.1103/PhysRevLett.99.041103

Long, A. S., Casey, C. M., del P. Lagos, C., et al. 2023, , 953, 11, doi: 10.3847/1538-4357/acddde

Lotz, J. M., Koekemoer, A., Coe, D., et al. 2017, , 837, 97, doi: 10.3847/1538-4357/837/1/97

Lousto, C. O., Zlochower, Y., Dotti, M., & Volonteri, M. 2012, , 85, 084015, doi: 10.1103/PhysRevD.85.084015

Lovell, C. C., Vijayan, A. P., Thomas, P. A., et al. 2021, , 500, 2127, doi: 10.1093/mnras/staa3360

Low, C., & Lynden-Bell, D. 1976, , 176, 367, doi: 10.1093/mnras/176.2.367

Mackey, A. D., & Gilmore, G. F. 2003, , 338, 85, doi: 10.1046/j.1365-8711.2003.06021.x

Madau, P., & Dickinson, M. 2014, , 52, 415, doi: 10.1146/annurev-astro-081811-125615

Magdis, G. E., Rigopoulou, D., Daddi, E., et al. 2017, , 603, A93, doi: 10.1051/0004-6361/201731037

Magdis, G. E., Gobat, R., Valentino, F., et al. 2021, , 647, A33, doi: 10.1051/0004-6361/202039280

Magnelli, B., Lutz, D., Saintonge, A., et al. 2014, , 561, A86, doi: 10.1051/0004-6361/201322217

Maiolino, R., & Mannucci, F. 2019, , 27, 3, doi: 10.1007/s00159-018-0112-2

Maiolino, R., Scholtz, J., Curtis-Lake, E., et al. 2023, arXiv e-prints, arXiv:2308.01230, doi: 10.48550/arXiv.2308.01230

Malmquist, K. G. 1922, Meddelanden fran Lunds Astronomiska Observatorium Serie I, 100, 1

Man, A., & Belli, S. 2018, Nature Astronomy, 2, 695, doi: 10.1038/s41550-018-0558-1

Mannucci, F., Cresci, G., Maiolino, R., Marconi, A., & Gnerucci, A. 2010, , 408, 2115, doi: `10.1111/j.1365-2966.2010.17291.x`

Maraston, C. 2005, , 362, 799, doi: `10.1111/j.1365-2966.2005.09270.x`

Marchesini, D., van Dokkum, P. G., Förster Schreiber, N. M., et al. 2009, , 701, 1765, doi: `10.1088/0004-637X/701/2/1765`

Martín-Navarro, I., Pérez-González, P. G., Trujillo, I., et al. 2015, , 798, L4, doi: `10.1088/2041-8205/798/1/L4`

Marziani, P., Sulentic, J. W., Dultzin-Hacyan, D., Calvani, M., & Moles, M. 1996, The Astrophysical Journal Supplement Series, 104, 37, doi: `10.1086/192291`

Marziani, P., Sulentic, J. W., Negrete, C. A., et al. 2010, Monthly Notices of the Royal Astronomical Society, 409, 1033, doi: `10.1111/j.1365-2966.2010.17357.x`

Mason, C. A., Trenti, M., & Treu, T. 2015, , 813, 21, doi: `10.1088/0004-637X/813/1/21`

Mathews, W. G., & Blumenthal, G. R. 1977, The Astrophysical Journal, 214, 10, doi: `10.1086/155225`

McCaffrey, J., Hardin, S., Wise, J., & Regan, J. 2023, arXiv e-prints, arXiv:2304.13755, doi: `10.48550/arXiv.2304.13755`

McKee, C. F., & Ostriker, E. C. 2007, , 45, 565, doi: `10.1146/annurev.astro.45.051806.110602`

McLeod, D. J., McLure, R. J., Dunlop, J. S., et al. 2021, , 503, 4413, doi: `10.1093/mnras/stab731`

Merritt, D., Storchi-Bergmann, T., Robinson, A., et al. 2006, , 367, 1746, doi: `10.1111/j.1365-2966.2006.10093.x`

Meyer, R. A., Bosman, S. E. I., & Ellis, R. S. 2019, , 487, 3305, doi: `10.1093/mnras/stz1504`

Mihos, J. C., & Hernquist, L. 1996, , 464, 641, doi: `10.1086/177353`

Milgrom, M. 1983, , 270, 365, doi: `10.1086/161130`

Miller, G. E., & Scalo, J. M. 1979, , 41, 513, doi: `10.1086/190629`

Miller, J. S., Goodrich, R. W., & Mathews, W. G. 1991, , 378, 47, doi: 10.1086/170406

Miller, T. B., van Dokkum, P., Mowla, L., & van der Wel, A. 2019, , 872, L14, doi: 10.3847/2041-8213/ab0380

Molaro, P., Levshakov, S. A., D'Odorico, S., Bonifacio, P., & Centurión, M. 2001, , 549, 90, doi: 10.1086/319072

Moster, B. P., Naab, T., & White, S. D. M. 2013, , 428, 3121, doi: 10.1093/mnras/sts261

Moster, B. P., Somerville, R. S., Newman, J. A., & Rix, H.-W. 2011, , 731, 113, doi: 10.1088/0004-637X/731/2/113

Moustakas, J., Coil, A. L., Aird, J., et al. 2013, , 767, 50, doi: 10.1088/0004-637X/767/1/50

Moutard, T., Sawicki, M., Arnouts, S., et al. 2020, , 494, 1894, doi: 10.1093/mnras/staa706

Murray, N. 2011, , 729, 133, doi: 10.1088/0004-637X/729/2/133

Murray, N., Chiang, J., Grossman, S. A., & Voit, G. M. 1995, The Astrophysical Journal, 451, 498, doi: 10.1086/176238

Muzzin, A., Marchesini, D., Stefanon, M., et al. 2013, The Astrophysical Journal Supplement Series, 206, 8, doi: 10.1088/0067-0049/206/1/8

Naidu, R. P., Oesch, P. A., van Dokkum, P., et al. 2022, , 940, L14, doi: 10.3847/2041-8213/ac9b22

Nanayakkara, T., Glazebrook, K., Kacprzak, G. G., et al. 2017, , 468, 3071, doi: 10.1093/mnras/stx605

Nandal, D., Regan, J. A., Woods, T. E., et al. 2024, arXiv e-prints, arXiv:2402.03428, doi: 10.48550/arXiv.2402.03428

Narayanan, D., Lower, S., Torrey, P., et al. 2024, , 961, 73, doi: 10.3847/1538-4357/ad0966

Nayakshin, S., & Sunyaev, R. 2005, , 364, L23, doi: 10.1111/j.1745-3933.2005.00097.x

Noeske, K. G., Weiner, B. J., Faber, S. M., et al. 2007a, , 660, L43, doi: 10.1086/517926

Noeske, K. G., Faber, S. M., Weiner, B. J., et al. 2007b, , 660, L47, doi: 10.1086/517927

Nürnberger, D. E. A., & Petr-Gotzens, M. G. 2002, , 382, 537, doi: 10.1051/0004-6361:20011600

Nussbaumer, H., & Schmutz, W. 1984, , 138, 495

Oesch, P. A., Bouwens, R. J., Illingworth, G. D., Labbé, I., & Stefanon, M. 2018, , 855, 105, doi: 10.3847/1538-4357/aab03f

Oesch, P. A., Bouwens, R. J., Carollo, C. M., et al. 2010, , 709, L21, doi: 10.1088/2041-8205/709/1/L21

Osterbrock, D. E. 1989, Annals of the New York Academy of Sciences, 571, 99, doi: 10.1111/j.1749-6632.1989.tb50500.x

Ostriker, J. P. 1983, The Astrophysical Journal, 273, 99, doi: 10.1086/161351

Papadopoulos, P. P. 2010, , 720, 226, doi: 10.1088/0004-637X/720/1/226

Peebles, P. J. E. 1993, Principles of Physical Cosmology, doi: 10.1515/9780691206721

Peng, Y., Maiolino, R., & Cochrane, R. 2015, , 521, 192, doi: 10.1038/nature14439

Peng, Y.-j., Lilly, S. J., Kovač, K., et al. 2010, , 721, 193, doi: 10.1088/0004-637X/721/1/193

Pérez-González, P. G., Rieke, G. H., Villar, V., et al. 2008, , 675, 234, doi: 10.1086/523690

Pettini, M., Steidel, C. C., Adelberger, K. L., Dickinson, M., & Giavalisco, M. 2000, , 528, 96, doi: 10.1086/308176

Pettini, M., Zych, B. J., Steidel, C. C., & Chaffee, F. H. 2008, , 385, 2011, doi: 10.1111/j.1365-2966.2008.12951.x

Pillepich, A., Nelson, D., Hernquist, L., et al. 2018, , 475, 648, doi: 10.1093/mnras/stx3112

Planck Collaboration, Aghanim, N., Akrami, Y., et al. 2020, , 641, A6, doi: 10.1051/0004-6361/201833910

Pozzetti, L., Bolzonella, M., Zucca, E., et al. 2010, , 523, A13, doi: 10.1051/0004-6361/200913020

Prince, R., Zajaček, M., Czerny, B., et al. 2022, , 667, A42, doi: 10.1051/0004-6361/202243194

Rieke, M. J., Robertson, B., Tacchella, S., et al. 2023, , 269, 16, doi: 10.3847/1538-4365/acf44d

Risaliti, G., Elvis, M., Fabbiano, G., Baldi, A., & Zezas, A. 2005, , 623, L93, doi: 10.1086/430252

Risaliti, G., Elvis, M., & Nicastro, F. 2002, , 571, 234, doi: 10.1086/324146

Robertson, B. E. 2022, , 60, 121, doi: 10.1146/annurev-astro-120221-044656

Saintonge, A., & Catinella, B. 2022, , 60, 319, doi: 10.1146/annurev-astro-021022-043545

Salim, S., Lee, J. C., Davé, R., & Dickinson, M. 2015, , 808, 25, doi: 10.1088/0004-637X/808/1/25

Salim, S., Rich, R. M., Charlot, S., et al. 2007, , 173, 267, doi: 10.1086/519218

Salpeter, E. E. 1955, , 121, 161, doi: 10.1086/145971

Sanders, D. B., Scoville, N. Z., & Soifer, B. T. 1991, , 370, 158, doi: 10.1086/169800

Schechter, P. 1976, , 203, 297, doi: 10.1086/154079

Schmidt, M. 1963, , 197, 1040, doi: 10.1038/1971040a0

Schnee, S., Li, J., Goodman, A. A., & Sargent, A. I. 2008, The Astrophysical Journal, 684, 1228, doi: 10.1086/590375

Schnittman, J. D., & Buonanno, A. 2007, , 662, L63, doi: 10.1086/519309

Schreiber, C., Elbaz, D., Pannella, M., et al. 2018, , 609, A30, doi: 10.1051/0004-6361/201731506

Scoville, N., Aussel, H., Brusa, M., et al. 2007, The Astrophysical Journal Supplement Series, 172, 1, doi: 10.1086/516585

Scoville, N., Lee, N., Vanden Bout, P., et al. 2017, , 837, 150, doi: 10.3847/1538-4357/aa61a0

Shapley, H., & Curtis, H. D. 1921, Bulletin of the National Research Council, 2, 171

Shapovalova, A. I., Burenkov, A. N., Carrasco, L., et al. 2001, Astronomy and Astrophysics, 376, 775, doi: 10.1051/0004-6361:20011011

Shen, Y., Richards, G. T., Strauss, M. A., et al. 2011, The Astrophysical Journal Supplement Series, 194, 45, doi: 10.1088/0067-0049/194/2/45

Shen, Y., Brandt, W. N., Richards, G. T., et al. 2016, The Astrophysical Journal, 831, 7, doi: 10.3847/0004-637X/831/1/7

Silk, J. 1995, , 438, L41, doi: 10.1086/187710

Smith, S. 1936, , 83, 23, doi: 10.1086/143697

Sneppen, A., Steinhardt, C. L., Hensley, H., et al. 2022, The Astrophysical Journal, 931, 57, doi: 10.3847/1538-4357/ac695e

Sodroski, T. J., Odegard, N., Arendt, R. G., et al. 1997, , 480, 173, doi: 10.1086/303961

Sohn, T. S. 2019, in STIS Data Handbook v. 7, Vol. 7 (Baltimore: STScI), 7

Solomon, P. M., Downes, D., Radford, S. J. E., & Barrett, J. W. 1997, , 478, 144, doi: 10.1086/303765

Somerville, R. S., & Davé, R. 2015, , 53, 51, doi: 10.1146/annurev-astro-082812-140951

Song, J., Fang, G., Lin, Z., Gu, Y., & Kong, X. 2023, , 958, 82, doi: 10.3847/1538-4357/ad0365

Song, M., Finkelstein, S. L., Ashby, M. L. N., et al. 2016, , 825, 5, doi: 10.3847/0004-637X/825/1/5

Sorba, R., & Sawicki, M. 2015, , 452, 235, doi: 10.1093/mnras/stv1235

—. 2018, , 476, 1532, doi: 10.1093/mnras/sty186

Speagle, J. S., Steinhardt, C. L., Capak, P. L., & Silverman, J. D. 2014, , 214, 15, doi: 10.1088/0067-0049/214/2/15

Spitoni, E., Vincenzo, F., & Matteucci, F. 2017, , 599, A6, doi: `10.1051/0004-6361/201629745`

Stefanon, M., Bouwens, R. J., Labbé, I., et al. 2021, , 922, 29, doi: `10.3847/1538-4357/ac1bb6`

—. 2017, , 843, 36, doi: `10.3847/1538-4357/aa72d8`

Steidel, C. C., Giavalisco, M., Pettini, M., Dickinson, M., & Adelberger, K. L. 1996, , 462, L17, doi: `10.1086/310029`

Steinhardt, C. L., Capak, P., Masters, D., & Speagle, J. S. 2016, The Astrophysical Journal, 824, 21, doi: `10.3847/0004-637X/824/1/21`

Steinhardt, C. L., Jespersen, C. K., & Linzer, N. B. 2021, , 923, 8, doi: `10.3847/1538-4357/ac2a2f`

Steinhardt, C. L., Kokorev, V., Rusakov, V., Garcia, E., & Sneppen, A. 2023a, , 951, L40, doi: `10.3847/2041-8213/acdef6`

Steinhardt, C. L., Rusakov, V., Clark, T. H., et al. 2023b, , 949, L38, doi: `10.3847/2041-8213/acd447`

Steinhardt, C. L., Sneppen, A., Clausen, T., et al. 2023c, arXiv e-prints, arXiv:2305.15459, doi: `10.48550/arXiv.2305.15459`

Steinhardt, C. L., Schramm, M., Silverman, J. D., et al. 2012, The Astrophysical Journal, 759, 24, doi: `10.1088/0004-637X/759/1/24`

Steinhardt, C. L., Alexandroff, R., Capak, P. L., et al. 2019, Understanding an Extreme QSO: The Curious Case of SDSS 0956+5128, HST Proposal: 2019hst..prop15872S

Steinhardt, C. L., Sneppen, A., Hensley, H., et al. 2022a, The Astrophysical Journal, 934, 22, doi: `10.3847/1538-4357/ac7642`

Steinhardt, C. L., Sneppen, A., Mostafa, B., et al. 2022b, The Astrophysical Journal, 931, 58, doi: `10.3847/1538-4357/ac62d6`

Stolte, A., Brandner, W., Brandl, B., & Zinnecker, H. 2006, , 132, 253, doi: `10.1086/504589`

Stolte, A., Grebel, E. K., Brandner, W., & Figer, D. F. 2002, , 394, 459, doi: `10.1051/0004-6361:20021118`

Strait, V., Brammer, G., Muzzin, A., et al. 2023, , 949, L23, doi: 10.3847/2041-8213/acd457

Strateva, I. V., Strauss, M. A., Hao, L., et al. 2003, The Astronomical Journal, 126, 1720, doi: 10.1086/378367

Sullivan, M., Treyer, M. A., Ellis, R. S., et al. 2000, , 312, 442, doi: 10.1046/j.1365-8711.2000.03140.x

Sung, H., & Bessell, M. S. 2004, , 127, 1014, doi: 10.1086/381297

Syer, D., Clarke, C. J., & Rees, M. J. 1991, Monthly Notices of the Royal Astronomical Society, 250, 505, doi: 10.1093/mnras/250.3.505

Tacchella, S., Dekel, A., Carollo, C. M., et al. 2016a, , 458, 242, doi: 10.1093/mnras/stw303

—. 2016b, , 457, 2790, doi: 10.1093/mnras/stw131

Tacchella, S., Finkelstein, S. L., Bagley, M., et al. 2022, , 927, 170, doi: 10.3847/1538-4357/ac4cad

Tanaka, M., Coupon, J., Hsieh, B.-C., et al. 2018, , 70, S9, doi: 10.1093/pasj/psx077

Taylor, G. 1950, Proceedings of the Royal Society of London Series A, 201, 159, doi: 10.1098/rspa.1950.0049

Tilvi, V., Papovich, C., Tran, K. V. H., et al. 2013, , 768, 56, doi: 10.1088/0004-637X/768/1/56

Topping, M. W., Stark, D. P., Endsley, R., et al. 2022, , 941, 153, doi: 10.3847/1538-4357/aca522

Trakhtenbrot, B., & Netzer, H. 2012, , 427, 3081, doi: 10.1111/j.1365-2966.2012.22056.x

Treu, T., Auger, M. W., Koopmans, L. V. E., et al. 2010, , 709, 1195, doi: 10.1088/0004-637X/709/2/1195

Treu, T., Suyu, S. H., & Marshall, P. J. 2022, , 30, 8, doi: 10.1007/s00159-022-00145-y

Treyer, M. A., Ellis, R. S., Milliard, B., Donas, J., & Bridges, T. J. 1998, , 300, 303, doi: 10.1046/j.1365-8711.1998.01909.x

Trussler, J., Maiolino, R., Maraston, C., et al. 2021, , 500, 4469, doi: 10.1093/mnras/staa3545

Tsalmantza, P., Decarli, R., Dotti, M., & Hogg, D. W. 2011, , 738, 20, doi: 10.1088/0004-637X/738/1/20

U, V., Barth, A. J., Vogler, H. A., et al. 2022, , 925, 52, doi: 10.3847/1538-4357/ac3d26

Urry, C. M., & Padovani, P. 1995, , 107, 803, doi: 10.1086/133630

Valentino, F., Magdis, G. E., Daddi, E., et al. 2020, , 890, 24, doi: 10.3847/1538-4357/ab6603

van Dokkum, P., Brammer, G., Wang, B., Leja, J., & Conroy, C. 2024, Nature Astronomy, 8, 119, doi: 10.1038/s41550-023-02103-9

van Dokkum, P., Conroy, C., Villaume, A., Brodie, J., & Romanowsky, A. J. 2017a, , 841, 68, doi: 10.3847/1538-4357/aa7135

—. 2017b, , 841, 68, doi: 10.3847/1538-4357/aa7135

van Dokkum, P. G., & Conroy, C. 2012, , 760, 70, doi: 10.1088/0004-637X/760/1/70

Vanden Berk, D. E., Richards, G. T., Bauer, A., et al. 2001, The Astronomical Journal, 122, 549, doi: 10.1086/321167

Vestergaard, M., & Osmer, P. S. 2009, , 699, 800, doi: 10.1088/0004-637X/699/1/800

Vestergaard, M., & Wilkes, B. J. 2001, , 134, 1, doi: 10.1086/320357

Weaver, J. R., Kauffmann, O. B., Ilbert, O., et al. 2022, , 258, 11, doi: 10.3847/1538-4365/ac3078

Weaver, J. R., Davidzon, I., Toft, S., et al. 2023, , 677, A184, doi: 10.1051/0004-6361/202245581

Wechsler, R. H., & Tinker, J. L. 2018, , 56, 435, doi: 10.1146/annurev-astro-081817-051756

Weidner, C., & Kroupa, P. 2005, , 625, 754, doi: 10.1086/429867

Whitaker, K. E., van Dokkum, P. G., Brammer, G., & Franx, M. 2012, , 754, L29, doi: 10.1088/2041-8205/754/2/L29

Whitaker, K. E., Franx, M., Leja, J., et al. 2014, , 795, 104, doi: 10.1088/0004-637X/795/2/104

Whitler, L., Endsley, R., Stark, D. P., et al. 2023a, , 519, 157, doi: 10.1093/mnras/stac3535

Whitler, L., Stark, D. P., Endsley, R., et al. 2023b, , 519, 5859, doi: 10.1093/mnras/stad004

Wilkes, B. J. 1986, , 218, 331, doi: 10.1093/mnras/218.2.331

Williams, R. J., Quadri, R. F., Franx, M., van Dokkum, P., & Labbé, I. 2009, , 691, 1879, doi: 10.1088/0004-637X/691/2/1879

Wills, B. J., Brotherton, M. S., Fang, D., Steidel, C. C., & Sargent, W. L. W. 1993, The Astrophysical Journal, 415, 563, doi: 10.1086/173186

Wyder, T. K., Treyer, M. A., Milliard, B., et al. 2005, , 619, L15, doi: 10.1086/424735

Yan, H., Sun, B., Ma, Z., & Ling, C. 2023, arXiv e-prints, arXiv:2311.15121, doi: 10.48550/arXiv.2311.15121

York, D. G., Adelman, J., Anderson, John E., J., et al. 2000, , 120, 1579, doi: 10.1086/301513

Yu, X., Li, J.-T., Qu, Z., et al. 2021, Monthly Notices of the Royal Astronomical Society, 505, 4444, doi: 10.1093/mnras/stab1614

Yung, L. Y. A., Somerville, R. S., Finkelstein, S. L., Wilkins, S. M., & Gardner, J. P. 2023, arXiv e-prints, arXiv:2304.04348, doi: 10.48550/arXiv.2304.04348

Zahid, H. J., Dima, G. I., Kewley, L. J., Erb, D. K., & Davé, R. 2012, , 757, 54, doi: 10.1088/0004-637X/757/1/54

Zajaček, M., Czerny, B., Martinez-Aldama, M. L., et al. 2020, , 896, 146, doi: 10.3847/1538-4357/ab94ae

Zavala, J. A., Casey, C. M., Manning, S. M., et al. 2021, , 909, 165, doi: 10.3847/1538-4357/abdb27

Zhang, Z.-Y., Romano, D., Ivison, R. J., Papadopoulos, P. P., & Matteucci, F. 2018, , 558, 260, doi: 10.1038/s41586-018-0196-x

Zheng, W., Binette, L., & Sulentic, J. W. 1990, , 365, 115, doi: 10.1086/169462

Zhu, J.-P., Wang, K., & Zhang, B. 2021, , 917, L28, doi: 10.3847/2041-8213/ac1a17

Zolotov, A., Dekel, A., Mandelker, N., et al. 2015, , 450, 2327, doi: 10.1093/mnras/stv740

Zwicky, F. 1933, Helvetica Physica Acta, 6, 110